Modeling 2008 in Massachusetts Bay using an upgraded unstructured-grid Bays Eutrophication Model

Massachusetts Water Resources Authority
Environmental Quality Department
Report 2010-15

Citation:

Chen C, Tian R, Beardsley RC, Qi J, Xu Q. 2010. **Modeling 2008 in Massachusetts Bay using an upgraded unstructured-grid Bays Eutrophication Model**. Boston: Massachusetts Water Resources Authority. Report 2010-15. 128p.

Key word acronyms and definitions

ECOM-si	Estuarine and Coastal Ocean Model-semi-implicit. A structured-grid hydrodynamic model.
FVCOM	Finite-Volume Coastal Ocean Model: An unstructured-grid hydrodynamic model.
GoM/GB FVCOM	FVCOM applied to the Gulf of Maine/Georges Bank.
RCA	Row Column Advanced (RCA) ecological systems operating program: a water quality model.
UG-RCA	Unstructured-grid version of RCA.
BEM	Massachusetts Bay Eutrophication Model: a coupled water quality and hydrodynamics model system.
WRF	Weather Research and Forecast Model
Cyclone	Wind circulation associated with a low-pressure system - counterclockwise in the northern hemisphere.
NRMSE	Normalized root mean square error

Modeling 2008 in Massachusetts Bay using an upgraded unstructured-grid Bays Eutrophication Model

Submitted to

Massachusetts Water Resources Authority
Environmental Quality Department
100 First Avenue
Charlestown Navy Yard
Boston, MA 02129
(617) 242-6000

Prepared by
Changsheng Chen[1], Rucheng Tian[1], R.C. Beardsley[2], Jianhua Qi[1] and Qichun Xu[1]

[1]School for Marine Science and Technology
University of Massachusetts-Dartmouth
New Bedford, MA 02744

[2]Department of Physical Oceanography
Woods Hole Oceanographic Institution
Woods Hole, MA 02543

August 2010

EXECUTIVE SUMMARY

The Massachusetts Water Resources Authority (MWRA) contracted the Marine Ecosystem Dynamics Modeling (MEDM) laboratory of University of Massachusetts at Dartmouth (UMASSD) to 1) update the Massachusetts Bay Eutrophication Model (BEM) by replacing the structured-grid ECOM-si/RCA* with the unstructured-grid FVCOM/UG-RCA* and 2) simulate currents, temperature, salinity, dissolved oxygen, and other water quality parameters in Massachusetts Bay for calendar year 2008. This report summarizes the results of these two major tasks. This report also includes the results of two projection runs: removing the MWRA outfall to identify its potential impacts on water quality and ecosystem function in Massachusetts Bay, and reducing monitoring sites to examine the potential influences of the amended monitoring program on the modeling performance in simulating the Bay water quality conditions.

The updated BEM with FVCOM/UG-RCA has improved the reality and accuracy of the Bay-scale simulation by *a*) refining horizontal and vertical model resolutions; *b*) accurate geometric fitting to resolve islands and other irregular coastal geometry in the Massachusetts Bay and Boston Harbor system; *c*) automatic grid nesting that allow us to drive the Massachusetts Bay FVCOM with the US Northeast Coastal Ocean Forecast System (NECOFS) through a mass conservative nesting boundary; *d*) data assimilation methods to integrate various types of hydrographic data into the model to provide the best known hydrodynamics fields to drive the water quality model and *e*) full MPI parallelization that can efficiently run FVCOM on multi-processor clusters to save labor commitment while improving resolution. The most important improvement is that by using FVCOM no open boundary conditions from other models are required, so that the model results in the Massachusetts Bay are not influenced by unrealistic specification of the open boundary condition.

The model reproduced the observed seasonal cycles of monitored physical and water quality variables. The seasonal variation of the water quality field was dominated by a spring and a fall phytoplankton bloom characterized by high chlorophyll concentration and decreased nutrients in surface waters in spring. Dissolved oxygen (DO) showed high values during the spring phytoplankton bloom as a result of photosynthetic production, but remained at a low level in fall without response to the fall bloom. This suggests that the DO dynamics during the fall bloom is controlled by multiple factors such as high consumption by increased remineralization and low solubility under high temperature. As expected, no bay-wide influences of the MWRA outfall were found, except for a minor change in dissolved inorganic nutrient concentration in the bottom layer close to the outfall. The reduction of monitoring sites does not seem to cause dramatic changes for short-term simulations.

* ECOM-si/RCA - model configuration with Estuarine and Coastal Ocean Model-semi-implicit hydrodynamic model driving Row Column Advanced (RCA) water quality model

FVCOM/UG-RCA - model configuration with Finite-Volume Coastal Ocean Model hydrodynamic model driving unstructured-grid version of RCA water quality model

Table of Contents

List of figures

List of Tables

1. Introduction

The Massachusetts Bay Eutrophication Model (BEM) has served as a key tool to understanding the effects of the Massachusetts Water Resources Authority (MWRA) outfall on water quality in Massachusetts Bay over the last two decades. This model has helped with decisions about the level of treatment required for a discharge at the MWRA outfall in the Massachusetts Bay, and has provided an annual assessment of the outfall discharge's influence on the local ecosystem.

Previously, BEM was an application of the structured-grid models ECOM-si and RCA. In this report we introduce an unstructured grid version of BEM. ECOM-si is the modified semi-implicit version of the three-dimensional (3D), free-surface, primitive equation structured-grid, finite-difference Princeton Ocean Model (POM) (Blumberg, 1994). This model was first configured for Massachusetts Bay by Signell et al. (1996) and calibrated to simulate the realistic currents and water stratification in the Bay by HydroQual and Signell (2001). Subsequently that model was used as the MWRA-authorized hydrodynamics model for Massachusetts Bay modeling through 2007 (Jiang and Zhou, 2003; 2004a,b; 2006a,b; 2008a,b; Chen et al., 2009a; Tian et al., 2009). ECOM-si was the best available model when it was applied to the Massachusetts Bay 15 years ago. The technology for numerical computation for coastal ocean models has developed rapidly in the last decade. Compared with other current popular models, ECOM-si is now rarely used by the ocean community due to its outdated technology. For the MWRA modeling project, the ECOM-si has shown its limitation in resolution and realistic geometric fitting, open boundary conditions, surface forcing and data assimilation. Massachusetts Bay has irregular features that are not easily fitted with a uniform grid: harbors, islands, sounds, estuaries, tidal creeks, wetlands, a narrow canal to the south, steep bottom topography offshore near Stellwagen Bank, and a complex active boundary with the western Gulf of Maine. Resolving the complex coastal geometry plays a critical role in capturing the realistic circulation in the Bay, particularly in the Boston Harbor area.

This report describes how we updated BEM by replacing the structured-grid ECOM-si/RCA with the unstructured-grid FVCOM/UG-RCA. FVCOM is an unstructured-grid, finite volume, 3D, free surface primitive equation coastal ocean model developed originally by Chen et al. (2003) and updated by a team of scientists at the University of Massachusetts-Dartmouth (UMASSD) and Woods Hole Oceanographic Institution (WHOI) (Chen et al., 2006a,b, Chen et al. 2007, Huang et al., 2008). The governing equations used in FVCOM are the same as in ECOM-si. The major difference between the two models is that ECOM-si is solved using a finite difference scheme and integrated with the semi-implicit method while FVCOM is solved numerically by a flux calculation in an integral form of the governing equations over non-overlapping, unstructured triangular grids. Flux calculation ensures the conservation of mass and momentum over individual control volumes and thus the whole computational domain. The finite-volume numerical approach combines the advantage of finite-element methods for geometric flexibility and finite-difference methods for simple discrete code structure and computational efficiency. UG-RCA is the unstructured grid version of RCA. Both FVCOM and UG-RCA are coded with Message Passing Interface (MPI) parallelization, which can run efficiently on a multi-processor cluster computer.

Replacing ECOM-si/RCA with FVCOM/UG-RCA is aimed at *a)* refining horizontal and vertical model resolution, which has demonstrated to be important to accurate simulation of hydrodynamics of Massachusetts Bay; *b*) providing an accurate geometric fitting that is capable of

resolving all islands and other irregular coastal geometry in the Massachusetts Bay and Boston Harbor; *c*) introducing automatic grid nesting that allows us to drive the Massachusetts Bay FVCOM using NECOFS through a mass-conservative nesting boundary with assimilated temperature, salinity and currents; *d*) upgrading the data assimilation methods to integrate various types of hydrographic and current data into the model to provide the best knowledge of hydrodynamics fields to drive the water quality model (UG-RCA); *e*) implementing the fully MPI parallelization that can efficiently run FVCOM and UG-RCA on multi-processor clusters to save labor commitment while improving resolution.

This report summarizes our activities in both updating BEM and simulating the 2008 hydrodynamics and water quality conditions in the Bay. The section on updating BEM includes the description and validation of FVCOM/UG-RCA, and the section on the 2008 simulation focuses on the model-data comparison at MWRA monitoring sites.

2. Updating BEM and Model Configuration for the 2008 Simulation

2.1 Description of FVCOM/UG-RCA

The updated BEM is the model system including FVCOM and UG-RCA. FVCOM is an unstructured-grid, finite volume, 3D, free surface primitive equation Coastal Ocean Model developed originally by Chen et al. (2003). FVCOM is a MPI parallelized model updated by the team of scientists at the University of Massachusetts-Dartmouth (UMASSD) and Woods Hole Oceanographic Institution (WHOI) (Chen et al., 2006a,b). In the horizontal, FVCOM uses a non-overlapping unstructured triangular grid, which is particularly suitable to resolve the complex coastal geometry of Massachusetts Bay. In the vertical, FVCOM is discretized by layers following the generalized terrain-following hybrid coordinate (Pietrzak et al., 2002). This vertical coordinate system allows for uniform thickness vertical layers near the surface and bottom over the slope with a smooth transition to the topography-following layers in the inner shelf and estuaries, which is critical to resolve the wind-driven surface mixed layer and sloping bottom boundary layer. FVCOM is solved numerically by the flux calculation in an integral form of the governing equations with options of either mode-split (like POM and ROMS) or semi-implicit (like ECOM-si) schemes. Flux calculation ensures the conservation of mass and momentum over individual control volumes and thus the whole computational domain. The finite-volume numerical approach combines the advantage of finite-element methods for geometric flexibility and finite-difference methods for simple discrete code structure and computational efficiency.

FVCOM uses the modified MY-2.5 and Smagorinsky turbulent closure schemes for vertical and horizontal mixing, respectively (Mellor and Yamada, 1992; Smagorinsky, 1963). FVCOM provides optional vertical turbulence closure schemes using the General Ocean Turbulence Model (GOTM) developed by Burchard et al., 2002. The present version of FVCOM contains several new modules, non-hydrostatic dynamics (Lai et al., submitted); advanced data Kalman Filter data assimilation packages (Chen et al., 2009b); an unstructured-grid surface wave model (FVCOM-SWAVE) (Qi et al., 2008), and an unstructured-grid sea ice model (UG-CICE, Gao et al, submitted), a sediment model (FVCOM-SED) and generalized biological model (FVCOM-GEM). An automatic nesting grid system is also implemented in FVCOM, which allows two different FVCOM models to run through the nested boundary without need of interpolation from one to another.

Built with FVCOM as a core model, we have developed an integrated atmospheric-ocean model system called the “Northeast Coastal Ocean Forecast System (NECOFS)” for the northeast US coastal region with a computational domain stretching from the south of Long Island Sound to the northeastern part of the Scotian Shelf. This system includes 1) two regional meso-scale meteorological models (MM5 and WRF); 2) Gulf of Maine/Georges Bank (GoM/GB) FVCOM, and 3) FVCOM-SWAVE. This system is in operation to provide 3-day forecast fields of water temperature, salinity, currents, surface elevation and other variables. Using NECOFS, we also re-built the hindcast hourly fields of assimilated currents, temperature, salinity, mixing rate, etc from 1995 to present for the Gulf of Maine including Massachusetts Bay. These fields can be directly used to drive the high-resolution subgrid Massachusetts Bay FVCOM and water quality model.

UG-RCA is the unstructured-grid finite-volume version of RCA modified by the UMASS FVCOM development team under contract to MWRA. RCA is the structured-grid version of the Row-Column Advanced water quality model developed by HydroQual (HydroQual, 2000, 2004). It consists of 26 water quality state variables and 23 sediment variables, including various forms of organic carbon, nitrogen and phosphorus, inorganic nutrients, phytoplankton and dissolved oxygen. Nutrient and carbon loadings from point sources (e.g., the MWRA sewage outfall), non-point sources (e.g., ground water), rivers and atmosphere are the major anthropogenic perturbations to the system. A comprehensive suite of biological, chemical and sedimentological variables is routinely observed within the framework of the MWRA-sponsored monitoring program. The data from this monitoring program were used to determine the initial conditions, boundary conditions, anthropogenic forcing and model validation for the RCA simulation. The model has successfully reproduced observed magnitudes and seasonal cycles of DO, phytoplankton, primary production, nutrients and nutrient flux at the sediment-water interface for 1992-94 and 1998-2007 (HydroQual, 2000, 2003; Jiang and Zhou 2004b, 2006b, 2008b; Tian et al. 2009). We converted RCA to the unstructured grid finite volume version (UG-RCA) using the same algorithms as FVCOM. We chose to base UG-RCA on RCA-v3, the newest version of RCA, because it is better supported, publicly accessible, and has more options for light attenuation, phytoplankton growth function, and reaeration than in earlier versions. UG-RCA is written in the MPI parallelized framework, so it can run in both online and offline modes. Under agreement with HydroQual, UG-RCA will serve as a publicly accessible community water quality module under the FVCOM framework.

In addition to updating the model framework, we made two changes to RCA-v3. (1) The structured-grid RCA-v3 requires re-calculating the salinity together with water quality variables. This approach is used to re-check that transport in the water quality model is accurate and is consistent with the physical model. There is no need to do this in an unstructured grid model. In UG-RCA, the salinity is obtained directly from the physical model output. The volume and mass conservations are checked directly by the fluxes in individual control volumes. This saves computation cost, particularly when data assimilation is done on salinity in the physical model. (2) In RCA-v3, the light function in phytoplankton growth is specified using the total solar radiation. Theoretically speaking, it should be the photosynthetically active radiance (PAR), even though PAR is usually proportional to the total short-wave solar radiation. UG-RCA uses PAR in the light function, with modification in parameters to ensure consistency with RCA-v3.

2.2 Differences between RCA-v2 and RCA-v3

BEM model runs prior to the 2008 calendar year run used RCA-v2. We based UG-RCA on RCA-v3, so here we list differences between RCA-v2 and RCA-v3.

Model functionality. RCA-v3 has more choices for functionalities and options than RCA-v2 (Table 2.1), although in this report we kept the same choices as RCA-v2. RCA-v3 is a modular simulation system that includes eutrophication, pathogens, tracer and residence time modules, whereas RCA-v2 is basically a eutrophication model. In the eutrophication module, RCA-v3 is coded in a more generalized way than RCA-v2. For example, the number of phytoplankton groups is defined as an array counting from 1 to *n* (*n* can be defined by users) in RCA-v3, whereas there are only three defined phytoplankton groups in RCA-v2. RCA-v3 provides the option of either of two phytoplankton growth functions: standard and Laws-Chalup, while RCA-v2 has only the

Laws-Chalup function. Multiple choices of air-sea oxygen reaeration parameterizations (including constant, spatially variable, velocity-shear-dependent, and wind shear-dependent formulations) are available in RCA-v3, whereas only the spatially variable reaeration parameterization is specified in RCA-v2. Similarly, multiple light attenuation functions (including constant, spatially variable, temporally variable, and 4D resolved functions) are available in RCA-v3, but only the spatially variable light attenuation function is coded in RCA-v2.

Parameters. State variables are listed in Table 2.2 and parameter definitions in Table 2.3. The number of parameters included in RCA-v3 and RCA-v2 is 180 and 134, respectively (Table 2.3). In RCA-v3, 31 of 180 parameters are not used in the present model setup, so that there are effectively 149 parameters. The parameter indices 1-4 are defined in RCA-v3.

- Index #1 "AGMOPT" stands for "Algal Growth Model Option", by which users can select different phytoplankton growth functions: "0" to select standard phytoplankton growth function, "1" to select the Laws-Chalup function.
- Index #2 "ACTALG" defines the number of "Active Algal Groups" effectively simulated in the model. It is assigned a value of 3 for winter-spring, summer and fall phytoplankton groups in Massachusetts Bay.
- Index #3 "KAOPT" defines the choice of reaeration parameterization: 0 for constant, 1 for spatially variable, 2 for velocity shear dependent, and 3 for wind shear dependent.
- Index #4 "KEOPT" defines the choice of light attenuation function: 0 for constant, 1 for spatially variable, 2 for temporally variable, 3 for 2D spatially and temporally variable, and 4 for 3D spatially and temporally variable.
- In UG-RCA, we added an additional parameter index #5 to allow the user to select a conversion factor from shortwave irradiance to PAR.

Because RCA-v3 has more options, there several new parameter indices compared to RCA-v2.

- For example, index #19 "K1RT", #52 "K2RT" and #83 "K3RT" are used to specify the respiration temperature-dependent coefficient for three phytoplankton groups, respectively in RCA-v3, whereas only a single constant value is used for the three phytoplankton groups in RCA-v2.
- A new state variable named "REPOC (REactive Particulate Organic Matter) is added in RCA-v3 (Table 2.2). (We did not model REPOC this in this report. Rather, we treated it as a dummy variable.)
- Two parameter indices #157 and #158 are added to define the hydrolysis of REPOC and its temperature-coefficient.
- RCA-v3 allows parameterization of the solid materials discharged from a Combined Sewer Overflow (CSO). This new module brought in three new parameter indices #161 and #162 to specify elemental ratios in solid CSO substances and #173-176 to specify the sedimentation of solid CSO materials.
- Adding multiple choices of oxygen reaeration brought in two parameters index #166 and #176 to define the reaeration rate in RCA-v3.
- In addition, the parameter index #180 "KECONST" is specified only when the constant attenuation option is chosen. This parameter index is not included in RCA-v2.

On the other hand, RCA-v2 has four parameter indexes used to define total active metals. These parameter indexes are removed in RCA-v3 (see Table 2.3).

2.3. Computational Domains and Grids

The implementation of FVCOM used for Massachusetts Bay is a sub-grid domain model (hereafter referred to as MB-FVCOM) nested within the Gulf of Maine regional domain model (hereafter referred to as GoM-FVCOM). The computational domain of MB-FVCOM is configured with 9738 cells and 5472 nodes. The horizontal resolution of this sub-grid domain varies from 290 m near the coast to 5-10 km near the nested boundary (Figure 2.1, upper panel). GoM-FVCOM consists of 27421 cells and 14777 nodes, with the horizontal resolution varying from 10-25 km in the open ocean to 1.0 km near the coast (Figure 2.1, lower panel). GoM-FVCOM uses hybrid terrain-following coordinates with a total number of 30 layers in the vertical. In shallow regions with depth < 60 m, the vertical layers are defined using the σ-coordinate, while in the region with depth ≥. 60 m, the s-coordinate is used. These two coordinates merge on the 60-m isobath at which the water column is divided by uniform layers with a thickness of 2 m. In the σ-coordinate, the layer thickness varies with water depth, with a maximum of ≤ 2 m. In the s-coordinate, five uniform layers with a thickness of 2 m is specified in the upper and lower layers connected to the surface and bottom, respectively.The remaining mid-depth is divided into 20 layers with thickness varying with water depth. The same vertical coordinate system was used for MB-FVCOM. The GoM regional and Massachusetts Bay sub-domain grids share common triangular cells along the nesting boundary. The model output from GoM-FVCOM at the nested boundary can directly drive MB-FVCOM with no need for any spatial interpolation. This one-way nesting approach ensures volume and mass conservation between the two computational domains.

Both GoM-FVCOM and MB-FVCOM are solved using the mode-split integration scheme. The time step is 12 seconds for the external mode and 120 seconds for the internal mode for GoM-FVCOM, and 5 seconds for the external mode and 50 seconds for the iinternal mode for MB-FVCOM.

UG-RCA is configured on the same grid as MB-FVCOM, but with a smaller offshore extent (Figure 2.1). It is driven by the hourly MB-FVCOM fields of water temperature, salinity, velocity and turbulence mixing diffusivities. UG-RCA is coded with the flexibility to allow users to select a different time step from the hydrodynamics model. For the Massachusetts Bay modeling project, the time step used to drive UG-RCA is 60 seconds, with 60 time steps per hour.

It should be pointed out here that horizontal resolution of MB-FVCOM is much higher than the ECOM-si and RCA used in the previous BEM system. The ECOM-si grid consisted of 68 rows and 68 columns and the RCA only used the first 54 columns. From the total of 3672 grid points in the ECOM-si domain, only 2091 were in the water and the rest on the land (and thus were not used in the computation). MB-FVCOM has a total of 9738 grid points and all of them are in the water. The horizontal resolution of this new Bay model system is thus about triple that of the previous BEM system. In addition, the ECOM-si used in the previous BEM system consists of ten σ-layers, which is also only one-third the vertical resolution used in MB-FVCOM.

2.4. Forcing

2.4.1 Physical models

Both GoM-FVCOM and MB-FVCOM are driven by 1) surface forcing (wind stress, precipitation, evaporation, surface net heat flux, and short-wave irradiance), 2) river discharges and 3) tidal forcing.

The surface forcing data were provided by the data-assimilated fields of the Weather Research and Forecast (WRF) model. WRF is the new-generation mesoscale numerical weather prediction system developed principally by National Center for Atmospheric Research (NCAR) through collaboration with other government agencies (http://wrf-model.org/index.php). This model is designed for both operational forecasting and atmospheric research and has multiple dynamical cores and 3-dimensional variational data assimilation. WRF uses the hydrostatic North American Mesoscale weather model fields as initial and boundary conditions with two-way nesting capability, and can provide continuous hindcasts and 3-day forecasts. WRF replacesthe older MM5 in our GoM weather forecast model system (Chen et al., 2005). GoM-WRF is configured with a "regional" domain (covering the Scotian Shelf, Gulf of Maine, Georges Bank, and the New England Shelf) and a "local" domain (covering Massachusetts coastal waters west to Long Island Sound) with horizontal grid spacing of 9 and 3 km respectively, and 31 sigma levels in the vertical with finer resolution in the Planetary Boundary Layer. All available data from the National Data Buoy Center's Coastal-Marine Automated Network (C-MAN)and meteorological buoys are assimilated. The surface wind stress, air-sea heat flux components, and evaporative flux are computed using GoM-WRF output, with a horizontal resolution of 9 km, the COARE 2.6 bulk algorithm (Fairall et al., 1996, 2003), and satellite sea surface temperature. The surface radiative fluxes are computed using International Satellite Cloud Climatology Project (ISCCP) data. The resulting hindcast data-assimilated surface forcing fields are used to drive both the regional GoM-FVCOM and MB-FVCOM.

GoM-FVCOM includes 33 rivers emptying into the GoM region. Of those, 13 are inside the Massachusetts Bay sub-domain. Those, plus the MWRA outfall discharge, are included in MB-FVCOM. The freshwater discharge data from the rivers were directly downloaded from the US Geological Survey (USGS) at http://waterdata.usgs.gov/ma/nwis. No accurate discharge data are available for the Mystic River, and its discharge was assumed to be proportional to the Charles River discharge by a factor of 0.195. The daily freshwater flow from the MWRA outfall was provided by MWRA.

Tidal forcing used to drive GoM-FVCOM was specified at the open boundary with the real o'clock time. The tidal elevation at the open boundary is calculated based on amplitudes and phases of five major tidal constituents: three semi-diurnal tides (M_2, S_2 and N_2,) and two diurnal tides (K_1 and O_1). In addition to the surface forcing and river discharge, MB-FVCOM is driven by the lateral boundary conditions specified through one-way nesting with the GoM-FVCOM model output. The surface elevation at the nesting node at the boundary is directly given by the GoM-FVCOM, so no tidal condition is required for the sub-domain Massachusetts Bay model.

2.4.2. Biological model

Surface forcing. UG-RCA is directly driven by the hourly model output field of MB-FVCOM. In addition to the initial and open boundary conditions, UG-RCA requires the surface wind speed and solar radiation as the surface forcing. The wind speed (w) is used to determine the reaeration rate for oxygen exchange at the air-sea interface, which is formulated as:

$$F_{O2} = k\left(DO_{sat} - DO\right) \tag{2.1}$$

$$k = 0.728\sqrt{w} - 0.317w + 0.0372w^2 \tag{2.2}$$

$$DO_{sat} = 14.6244 - 0.36713T + 0.0044972T^2 + 0.0966S + 0.00205S\cdot T + 0.0002739S^2 \tag{2.3}$$

where F_{O2} is the oxygen reaeration flux, DO_{sat} is the dissolved oxygen saturation concentration determined with an empirical function of temperature (T) and salinity (S) (Hyer et al., 1971; HydroQual, 1993), and k is the piston coefficient of the oxygen air-sea exchange, determined by an empirical function depending on the wind speed (Banks and Herrera, 1977).

The solar radiation is used to compute the phytoplankton growth rate based on the Laws-Chalup function:

$$\mu_{\max} = \frac{G_{pre}(1-k_{RG})(1-f_{SC})I}{G_{pre}/G_{pr0} + I\left[1+G_{pre}/(I_S G_{pr0})\right]}, \qquad (2.4)$$

where I is the photosynthetically active radiation PAR (einsteins m^{-2} d^{-1}) and I_s is the half-saturation radiation (Laws and Chalup, 1990). Other parameters are defined in Table 2.3.

Calibrated with satellite-derived shortwave irradiance and available measurement data at the coast, GoM-WRF provides the light intensity at the surface of the water column required for the BEM. In the structured-grid RCA, the light function used to calculate phytoplankton growth is directly specified using the short-wave irradiance. For this project, we used PAR instead of the shortwave irradiance. Since there are not sufficient PAR data available for the time integration scale in UG-RCA, a key issue here is how to convert the WRF-predicted total shortwave irradiance to PAR.

To address this, we downloaded the SeaWIFs-derived PAR data in the Massachusetts Bay area from a NASA website www.oceancolor.gsfc.nasa.gov/. This dataset covers a period from 1997 to present, with a spatial resolution of 8 km and a time interval of one day. The algorithm to calculate the PAR values was validated over a vast region of the world ocean (Frouin et al., www.oceancolor.gsfc.nasa.gov/*DOCS/seawifs_par_wfigs.pdf*). We compared the SeaWIFS-derived PAR to the shortwave irradiance predicted by GoM-MM5 (1997-2005) and GoM-WRF (2006-present). The results showed a robust correlation between PAR and shortwave irradiance in the Massachusetts Bay region, with a slope of 0.437 for the linear regression (Figure 2.2). The analysis indicates that 92% of the variance is explained by the regression. Using this coefficient we converted GoM-WRF-predicted short-wave irradiance data to PAR and used this to drive the UG-RCA simulation for 2008. To assess the impact of the change from the shortwave irradiance to PAR on the water quality simulation, we have made a comparison between the simulation results using these two data sets. Examples of the comparison are presented in the following section.

As noted in Figure 2.2, multiplying WRF shortwave irradiance (W m^{-2}) by the factor of 0.437 converts it to WRF PAR irradiance (in energy flux units of W m^{-2}). Dividing that by 0.2174 gives WRF PAR irradiance in quantum flux units of μE m^{-2} s^{-1}. That conversion is needed for several parameters in UG-RCA. The 0.2174 factor is based on the approximation that quanta of wavelengths of 400-700 nm are equally active for photosynthesis, and the average PAR wavelength is typically 550 nm. A single photon of that wavelength has energy 3.61×10^{-19} joules. A mole (einstein) of 550 nm photons has energy 2.174×10^{5} joules. An irradiance of 1 μE m^{-2} s^{-1} thus corresponds to 0.2174 W m^{-2}.

Nutrient loadings. Nutrient and carbon loadings include the MWRA effluent outfall from the Deer Island Treatment Plant (DITP), non-MWRA point sources, non-point sources, river discharge and atmospheric sources. Each source was specified based on recent observed data where available, combined with historical observations and estimates.

MWRA conducts daily measurements of treated sewage flow in millions of gallons per day and daily or weekly concentration of various pollutants in mg l^{-1}. The data for NO_3^-, NO_2^-, NH_4^+ and PO_4^{3-} were directly used to drive UG-RCA, while the bulk-parameter data of Biochemical Oxygen Demand (CBOD), Total Kjeldahl Nitrogen (TKN) and Total Phosphorus (TP) were first converted and partitioned into model variables (Tables 2.4 and 2.5). For example, CBOD was converted into total organic carbon using the function TOC = 0.7CBOD+18 (HydroQual and Normandeau, 1993) and then partitioned to each organic matter pool using the functions listed in Table 2.3. TKN and TP were converted into total organic nitrogen and phosphorus and then partitioned into their respective organic pools. Silicon was not analyzed on a regular basis at the MWRA outfall. To help determine the silicon loading, MWRA collected four samples over the period of May 19-22, 2009. MWRA's Department of Laboratory Services reported an average value for these samples of 90 µM Si l^{-1}. This value was about five times lower than the value of 446.4 µ M Si l^{-1} suggested by HydroQual (1993; p.3-6) for all RCA simulations. We followed MWRA's suggestion (Mike Mickelson, personal communication on June 12, 2009) and replaced the previous value used in RCA with the value estimated from the measurement.

Non-point source loadings comprise the storm drain system-derived runoff and groundwater discharge which are fully based on historical estimates (Menzie-Cura, 1991; Alber and Chan, 1994). For runoff from combined sewer systems, updates were conducted using the total estimated combined sewer overflow (CSO) volume at the Mystic/Chelsea confluences, the upper inner Harbor, the lower inner Harbor, Fort Point Channel, North Dorchester Bay, South Dorchester Bay and the Neponset River estuary. Estimated annual outflow at these sites were provided by Wendy Leo and Kelly Coughlin at MWRA. These data were divided into monthly values following the same monthly variation in freshwater discharge as the Charles River. The Charles River discharge is correlated with the precipitation in the region (Appendix A, Libby et al. 2009). Unfortunately, 2008 sewer system model results for CSO flows were not available at the time the 2008 simulation runs were performed. Following a suggestion by Wendy Leo (personal communication, March 30, 2009), the estimated CSO flows from 2007 were used for 2008, scaled to the river discharge in each year. The pollutant concentrations in combined sewage reported by Alber and Chan (1994, their Table 2.4) were used to estimate the contaminant loadings for previous BEM simulations and also for the 2008 simulation with UG-RCA. The groundwater discharges and those from other non-MWRA treatment plants were specified using the same value estimated by Menzie-Cura (1991).

The river discharges included in the UG-RCA simulation were the Charles River, Neponset River and Mystic River. The Merrimack River was included in MB-FVCOM, but not in UG-RCA since it was located outside the UG-RCA sub-domain. Flows were obtained as described in section 2.4.1. The nutrient concentrations near the mouth of these three rivers were measured by MWRA as part of its CSO receiving water monitoring program; the nutrient loading at these rivers were estimated using the monthly averaged values. Measurements were made of inorganic nutrients, organic phosphorus, particulate organic nitrogen (PON) and dissolved organic nitrogen (DON).

The river loadings were estimated by multiplying the river discharge rate with the nutrient concentration. The measured inorganic nutrients can be directly used, whereas the total organic phosphorus must be converted into model variables using the functions listed in Table 2.4. PON and DON were equally split into refractory and labile pools for RPON, LPON, RDON and LDON, respectively (Table 2.5). Because standard oceanographic measurements of nutrients and carbon do not determine how much is refractory, labile, or very labile (reactive), the coefficients in Table 2.5 are used to partition the measured amounts into the state variables (HydroQual and Normandeau, 1993.)

The atmospheric loadings were provided using the values estimated by Menzie-Cura (1991). These values were used in the previous BEM simulation (HydroQual and Normandeau, 1995; HydroQual, 2000; HydroQual, 2003; Jiang and Zhou, 2004b; Tian et al., 2009). The loadings included both dry-fall and wet-fall inorganic and organic nitrogen, phosphorus, and carbon.

For organic carbon loading, non-MWRA sewage treatment plants contributed the largest value in 2008, followed by the MWRA outfall, atmospheric, river and non-point sources (Figure 2.3). The MWRA outfall only counted for 24% of the total organic carbon loading. For nitrogen loading, however, the MWRA outfall represented the largest value (50%), followed by the atmospheric flux (29%), non-MWRA point sources (13%), non-point sources (4%) and river discharge (4%). For phosphorus loading, the MWRA outfall again contributed the largest portion (58%), followed by the non-MWRA point sources (29%), non-point sources (6%), river discharge (4%) and atmospheric flux (3%).

2.5. Open boundary conditions for UG-RCA

The UG-RCA simulation requires the open boundary conditions of water quality state variables. Following the previous BEM simulation approach, bi-weekly open boundary conditions were specified by using the objective analysis (OA) procedure to interpolate the MWRA field data (Libby et al. 2009) onto the boundary nodes. The field measurements were made monthly at 7 stations near the MWRA outfall (called "nearfield" stations indicated by "N") and bimonthly at 24 farfield stations indicated by "F" (Figure 2.4). Because of the outbreak of a harmful algal bloom in late spring and early summer 2008, three cruises were added on May 28, June 3 and June 24 for the "*Alexandrium* Rapid Response Study (ARRS)". During these ARRS cruises, 8 additional stations were added (indicated by "AF" in Figure 2.4). Meanwhile, 4 nearfield stations (N04, N10, N16 and N18) and 7 farfield stations (F05, F06, F07, F13, F17, F22 and F31) were occupied.

The data included 14 variables: Chlorophyll, DO, NH_4^+, NO_3^-, PO_4^{3-}, SiO_3^{2-}, DON, DOC, DOP, PON, POC, POP, Biogenic silica and salinity. DON was estimated by the difference between the total dissolved nitrogen (TDN) and total dissolved inorganic nitrogen (NO_3^-, NO_2^-, NH_4^+). DOP was estimated by the difference between total dissolved phosphorus (TDP) and dissolved phosphate (PO_4^{3+}). Particulate phosphorus (PARTP) was used as POP. The OA mapped chlorophyll field was partitioned to the three-phytoplankton groups using the partition coefficients listed in Table 2.6. The fraction of the phytoplankton represented by each group changes over time and space in the model. The coefficients in Table 2.6 are the partitions imposed at the open boundary during each season of the year. From January to April, the chlorophyll along the boundary was considered as entirely composed of the winter-spring phytoplankton group with a zero partition coefficient to the other two phytoplankton groups. May was considered as a transition period with chlorophyll being

equally split into winter-spring and summer phytoplankton groups. In June and July, the chlorophyll belonged to the summer phytoplankton group. August was another transitional period with chlorophyll being split into the summer and fall phytoplankton groups. Chlorophyll consisted of only fall phytoplankton in September and October and was split into winter-spring and fall phytoplankton groups in December. The carbon to chlorophyll ratios of phytoplankton were 40, 65 and 15 for winter-spring, summer and fall phytoplankton, respectively (HydroQual, 2000; HydroQual, 2003; Jiang and Zhou, 2004b; Tian et al., 2009). DON and PON were split equally into labile and refractory pools. The partition coefficients for organic carbon and phosphorus are listed in Table 2.5.

The OA procedure was done using the OA software called OAX. This software was developed by Bedford Institute of Oceanography (Hendry and He, 1996). We used this method in the 2006-2007 BEM simulation (Tian et al., 2009). In the OAX, the covariance function (R) between data and estimation site is based on their pseudo-distance (r) determined as:

$$R(r) = (1 + r + \frac{r^3}{3})e^{-r} \tag{2.5}$$

$$r = \sqrt{\left(\frac{x_d - x_m}{a}\right)^2 + \left(\frac{y_d - y_m}{b}\right)^2 + \left(\frac{z_d - z_m}{c}\right)^2 + \left(\frac{t_d - t_m}{T}\right)^2} \tag{2.6}$$

where x ,y, z, and t are the four spatial and temporal coordinates; the subscripts d and m indicate data and model positions, respectively; and parameters a, b, c, and T are the de-correlation scales for their corresponding coordinate. Given the fact that the measurement sites were away from the open boundary and measurements were made on a monthly or bi-monthly basis, the OA procedure was done with relatively large de-correlation scales: 30 km in the horizontal, 15 m in the vertical and 45 days in time.

Examples of the OA-mapping results on the open boundary for April 15 and August 15 are presented in Figures 2.5-2.8. Chlorophyll concentration was higher in April than in August and both displayed a subsurface chlorophyll maximum (Figures 2.5 and 2.6). Nutrients showed high concentrations in the deeper channel and depletion in the surface layer. On the April section, dissolved nutrients were somewhat depleted near the surface with high concentrations in the deep basin. On the August transect, nutrients were further depleted near the surface, while remaining high in the deep water. The subsurface chlorophyll maximum indicates that phytoplankton growth is limited closer to the surface by these low nutrient levels, both in April and August. Similar to chlorophyll, DO concentration had higher surface values in April and slightly higher values in the subsurface layer in August. On the April transect, particulate organic substances showed high values in the middle of the transect (Figure 2.7), while dissolved organic matter had a relatively higher value near the surface than in the deeper region.

3. Model Validation Results

3.1. RCA-v3 vs RCA-v2

The objective of conducting a comparison experiment is to demonstrate that RCA-v3 can reproduce the results of RCA-v2, so that the shift from RCA-v2 to RCA-v3 would not produce contrast results as compared to those reported in previous BEM simulations. We did the 2006 BEM simulation for MWRA (Tian et al. 2009). Setting parameters as the same as those in RCA-v2, we repeated the 2006 simulation using RCA-v3. The comparison results are shown in Figures 3.1-3.11.

The time series of most variables for the two models were practically identical. Both predicted similar spring and fall phytoplankton blooms reflected by chlorophyll abundance (Figure 3.1). Dissolved oxygen in both surface and bottom waters showed similar magnitude and seasonal cycles, with high values during the spring phytoplankton bloom and low values during summer and early fall (Figures 3. 2 and 3.3). The nutrient predictions are practically superposed in both surface and bottom waters with the same magnitudes and seasonal variations (Figures 3.4-3.7). Similarly, the dissolved and particulate organic nitrogen predicted by these two models were practically identical (Figures 3.8 and 3.9). Even at the sediment-water interface, only small differences in nutrient fluxes (exemplified by the ammonium flux) and sediment oxygen demand were discernable (Figures 3.10 and 3.11). The RCA-v2 and RCA-v3 codes are different, particularly for the sediment modules so that differences are inevitable. However, these differences are very limited and apparently RCA-v3 provides slightly better comparison with data. In conclusion, the similarity between the two simulations shows that RCA-v3 successfully reproduced the simulation by RCA-v2. The shift to RCA-v3 did not generate substantial changes in the simulated results.

3.2 RCA-v2 (ECOM-si) vs UG-RCA (FVCOM)

UG-RCA is the unstructured grid version of RCA-v3, which is derived from RCA-v2. We checked our overall code conversion by comparing model results driven by identical meteorological forcing. Here we compare the results of UG-RCA with RCA-v2 for 2006 forcing. RCA-v2 was driven as usual by the model output of ECOM-si, and UG-RCA was driven by the model output of MB-FVCOM.

We used the Normalized Root Mean Square Error (NRMSE) to measure the similarity between a simulation and data. The root mean square error (RMSE) is influenced by the unit so that it does not provide a uniform value across various variables, whereas NRMSE is independent of units. The normalized root mean square error is defined as the root mean square error divided by the difference between the observed maximum and minimum of the variable:

$$RMSE = \sqrt{\frac{\sum_{i=1}^{n}\left(x_m(i) - x_o(i)\right)^2}{n}}, \quad NRMSE = \frac{RMSE}{MAX(x_o) - MIN(x_o)} \qquad (3.1)$$

where x_m is modeled result, x_o is observation, n is the total number of data, $MAX(x_o)$ and $MIN(x_o)$ are maximum and minimum of observation. All the data from the MWRA monitoring program were included in the calculation of NRMSE. In addition to estimating the model-data fit for the entire year, the data were grouped into 3-month seasons to examine the seasonal variation in fit.

Table 3.1 presents the NRMSE of the 2006 RCA-v2 and UG-RCA simulations. Both models show the same seasonal variability in model-data fit for all state variables. No substantial difference was found in comparison with the measurement data. The slight difference between these two models is believed to be due to the different hydrodynamic models. A brief discussion of the comparison results is given below with reference to the NRMSE values in Table 3.1 and the model-data comparison plots in Figures 3.12-3.21.

For the chlorophyll concentration, the annual NRSME of UG-RCA is slightly lower than that of RCA-v2: 0.17 versus 0.20 near the surface and 0.17 versus 0.18 near the bottom. Near the surface, the UG-RCA provided a slightly better simulation of chlorophyll in spring, summer and fall, while RCA-v2 produced a better comparison with the observation in winter (Figure 3.12). Near the bottom (Figure 3.13), the results of the two models are quite similar, although UG-RCA showed lower NRMSEs in spring and summer and RCA-v2 showed lower NRMSEs in winter and fall.

For the DO concentration, RCA-v2 showed relatively lower annual values of NRMSE than UG-RCA: 0.15 and 0.10 versus 0.17 and 0.16 near the surface and bottom, respectively (Figures 3.14-3.15). RCA-v2 produced a slightly better model-data comparison in terms of NRMSE in winter, spring and fall seasons, but not in summer.

For nitrate concentration, the two models produced quite similar NRMSE near the surface: 0.14 for RCA and 0.15 for UG-RCA on an annual basis. The difference mainly appeared near the bottom. RCA-v2 produced a relatively lower annual NRMSE: 0.17 versus 0.22. For ammonium, UG-RCA produced a lower annual NRMSE than RCA-v2 near the surface, but a higher value near the bottom. When split into seasons, the dissolved inorganic nitrogen (DIN) predicted by UG-RCA had lower NRMSE values in summer and fall, an equal value in winter, but a higher value in spring near the surface (Figure 3.16). UG-RCA showed slightly higher NRMSE values near the bottom for all the seasons (Figure 3.17). As an overall assessment, the two models were much more similar than they were different.

For dissolved and particulate organic nitrogen (DON and PON), UG-RCA and RCA-v2 produced mostly comparable results (Figures. 3.18 and 3.19). UG-RCA produced slightly lower annual NRMSE values of PON in surface waters (0.21 vs. 0.26), but slightly higher in the bottom layer (0.29 versus 0.20) than RCA-v2. In the case of DON, UG-RCA produced slightly higher NRMSE in both surface and bottom waters on an annual basis (Table 3.1). When split into seasons, however, UG-RCA had a lower NRMSE in spring and fall than RCA-v2.

UG-RCA produced a slightly better simulation for nutrient fluxes and dissolved oxygen demand at the sediment-water interface (Figures 3.20 and 3.21). Lower fluxes predicted by UG-RCA at two stations in the harbor (Station BH02 and BH03) made this model a better match with observations.

Although the biological parameters remained identical for RCA-v2 and UG-RCA, the physical fields used to drive these two models are different. In addition to different hydrodynamic models, bathymetric data in MB-FVCOM and ECOM-si are different. In spite of these differences, the water quality model simulation results from the new model compare about equally well with the data.

3.3 Comparison of results with PAR and solar irradiance

We have compared the results of UG-RCA using a phytoplankton growth rate function which depends on light as solar irradiance, with the results using a growth rate that depends on light as PAR. A simple modification was made to the light intensity function in Eq. 2.4 by replacing shortwave radiation (SWR) by PAR. In detail, the saturation light intensities (IS1, IS2 and IS3) for the three phytoplankton groups were modified by multiplying by the estimated ratio of PAR to SWR (0.437). Correspondingly, the base gross photosynthetic rate (G_{pr0}) had to be changed. In RCA-v3, G_{pr0} = 0.28, while in UG-RCA with PAR, G_{pr0} = 0.64 (see Table 2.3). After these changes, the PAR- and SWR-driven simulation results were identical (Figure 3.22).

4. The 2008 Simulation Results

4.1 Physical Fields

4.1.1 Model-data comparisons

The BEM is designed to assess the water quality of Massachusetts Bay. Since this is highly controlled by the physical environment, available data were assimilated into the physical model MB-FVCOM to provide the best known physical fields for the water quality model. These data included the satellite-derived sea-surface temperature (SST) and all available hydrographic data. The model-data comparisons described here demonstrate how MB-FVCOM with these assimilated data provides realistic physical fields.

Figures 4.1 and 4.2 show the comparison between model-predicted and observed temperature and salinity at MWRA selected monitoring stations F26, F27, F29, F31, N01 and N10. Stations F26 and 27 are located in the northern part of the study area close to the UG-RCA open boundary. Station F29 is located in the southern part of the study area close to the open boundary. Stations N01 and N10 are located in central Massachusetts Bay and F31 is within Boston Harbor. Assimilation of SST and hydrographic data made the model-predicted temperature and salinity match the observations well.

Near the open boundary area (Stations F26, F27 and F29) and in the central Massachusetts Bay (N01 and N10), the water column was stratified from spring to early fall, with large temperature and salinity differences between the surface and bottom. At harbor station F31, however, the water column was fully mixed through the entire year. At Stations N01 and N10, the bottom temperature exhibited substantial high-frequency (weekly) fluctuations.

Salinity displayed larger fluctuations near the surface than near the bottom. The variation was particularly high at Stations F26 and F27, signaling the impact of the freshwater discharge from the Merrimack River just north of Massachusetts Bay.

Figures 4.3-4.7 compare the near-surface distributions of temperature and salinity. Note that the plots of observed data gather all the observations for the month. The plot for February includes the early February and the later February survey. Observations in the other months span at least three days, the shortest time it takes to complete a survey. The model plots gather model results for the same time as each observed data point. After the observed data and modeled results were gathered for the month, they were contoured. The assimilation worked well to reproduce realistic fields of temperature and salinity. In February, the temperature displayed a mostly homogeneous distribution in both temperature and salinity, with a slight inshore-offshore gradient in salinity (Figure 4.3). In April, both temperature and salinity exhibited a southeast-northwest gradient: warmer in the harbor and the northwestern Massachusetts Bay and colder in the southern Massachusetts Bay and offshore (Figure 4.4). Higher salinity corresponded to lower temperatures; salinity was low in the harbor and high in southern Massachusetts Bay and in the offshore region. The model reproduced both magnitude and distribution of the observations of both temperature and salinity. In June, the temperature and salinity distribution was similar to that in April, but with a

higher temperature (Figure 4.5). The temperature was < 8 °C in April and about 16 °C in June. In August, the surface temperature reached 20 °C, but with higher values in the offshore region, opposite to the distribution in June and April (Figure 4.6). In October, the surface temperature decreased considerably, to below 13 °C, but with slightly higher values in the harbor and coastal regions than in the offshore region (Figure 4.7). On the other hand, salinity showed a similar pattern year round, with lower values in the harbor and coastal regions and relatively higher values in the offshore region and in southern Massachusetts Bay.

4.1.2 Distributions of monthly averaged temperature and salinity

To examine the seasonal variability of water properties, we present in Figures 4.8-4.13 the monthly averaged fields of temperature and salinity near the surface. In section 4.1.1, we have shown that the water is seasonally well-stratified in Massachusetts Bay except in the shallow area of Boston Harbor. The monthly averaged fields showed that water temperature was not spatially uniform in the Bay. The temperature distributions in January-March were similar, with a relatively northeast-southwest oriented temperature front. The coldest water appeared in March, particularly in the northern coastal region which might be linked to the influence of the Western Gulf of Maine Coastal Current (WMCC). In April and May, however, the surface water temperature was higher in the bay than in the offshore region, forming a north-south oriented front. The northeast-southwest oriented temperature front appeared again in June with low temperature in the northeastern region of the simulation domain. This temperature front moved gradually southward from June through August when the temperature was notably lower in the northern bay than in Cape Cod Bay (Figure 4.9). The temperature front remained until the end of the year with a decreasing trend from August through December. On the other hand, salinity showed fewer spatial features in winter as compared with temperature. In January through March, salinity showed two low patches near the Merrimack River mouth and in Boston Harbor, respectively (Figure 4.11). In April, the low salinity region spread with the northwestern region of the computation domain filled with low salinity water. Low salinity water spread further in May and June with salinity values lower in Massachusetts Bay than in the offshore region (Figure 4.12). Salinity remained relatively low from May till September and increased again in October and November (Figure 4.13). The lower salinity in the coastal region and Massachusetts Bay from May through September is most likely due to the coastal current advection rather than freshwater discharge from local rivers, but monthly averaged distribution may not adequately characterize the current pattern. Subsequently, we present the simulated subtidal current in the following section.

4.1.3 Distributions of seasonally averaged sub-tidal currents

The signal of water intrusion from the northeastern open boundary was clearly evident in winter, spring and fall seasons (Figure 4.14). The model-predicted near-surface subtidal currents showed the Western Maine Coastal Current (WMCC) in winter, spring and fall. In the winter season, the southward WMCC entered Massachusetts Bay and was bifurcated at the northern end of Stellwagen Bank, with one branch turning clockwise and flowing into Massachusetts Bay and the other branch flowing southward along the eastern side of Stellwagen Bank. The spatial distribution of near-surface currents in spring was similar to that in winter. The model-predicted currents varied considerably on short (daily to weekly) time scales. However, these temporal variation signals were filtered out of the seasonal averaged fields. This suggests that in winter and spring of 2008, the total wind-energy input into the Massachusetts Bay was almost the same in each month of winter and spring, and the current was dominated by the wind-induced short-term variability. The current

in summer was characterized by cyclonic and anticyclonic subtidal eddies in the northern and southern areas of Stellwagen Bank. These eddies played a key role in reducing summertime exchange between the Gulf of Maine and Massachusetts Bay. Meanwhile, the currents in Boston Harbor featured multi-eddy fields, which could have intensified the harmful algal bloom observed in June in Massachusetts Bay. The distribution of seasonally averaged currents in the fall season was back to the pattern of winter and spring, even though the intensity of currents differed.

In order to have a quantitative idea about the coastal current and potential water intrusion into Massachusetts Bay, we estimated the daily volume transport across a transect of the Northern Passage off Cape Ann with a length of 13 km and depth ranging from 26 to 93 m (Figure 4.14). The transport was characterized by high-frequency variations (Figure 4.15). During most of the year, the water moved southwestward toward the bay, but occasionally the transport reversed and was northeastward out of the bay with a velocity ranging from -41 to 67 cm s^{-1} (positive velocity toward the bay) When split into seasons, the transport was the strongest in spring -- from April through June -- with an average of 88×10^3 m^3 s^{-1}, and weakest in fall -- from October through December -- with an average of 33×10^3 m^3 s^{-1}.

4.2 Water quality fields

4.2.1 Data-model comparison

In this section, we evaluate the 2008 simulation by using the NRMSE, correlation between simulation and observation, and plots for visual comparison of key variables at selected stations.

The annual NRMSE of the chlorophyll simulation in 2008 was 0.16 near the surface and 0.15 near the bottom (Table 3.1). These values were lower than those of the 2006 and 2007 simulations, modeled with either RCA or UG-RCA. Split into each season, the model-predicted 2008 chlorophyll concentration has its lowest NRMSE in spring and summer. As a general observation, the model has successfully captured the spring phytoplankton bloom in both 2006 and 2008. This is the most prominent feature of the annual phytoplankton cycle in Massachusetts Bay.

The annual NRMSE of model-predicted near-surface DO concentration in 2008 was lower than that in 2006 and 2007. In comparison to 2006, however, the model-predicted near-bottom DO concentration in 2008 was relatively high. The seasonal NRMSE values of DO concentration in 2008 were also lower than that those in 2006 and 2007. Compared with the 2006 UG-RCA simulation results, the model-predicted seasonal means of NRMSE in 2008 were lower in winter, spring and summer seasons, but higher in fall.

The error in model-predicted NO_3 concentration in 2008 was slightly lower than the 2006 UG-RCA simulation results in terms of annual NRMSE. There were not substantial differences for NO_3 in the seasonal means of NRMSE among the different years.

The NRMSEs of the modeled NH_4 concentration in 2008 were similar to the 2006 UG-RCA simulation results. The model-data fit was not as good near the bottom. The NMRSEs of PON and DON concentrations for the 2008 simulation were mostly lower than the 2006 simulation results.

Data-model correlation analyses of key variables are presented in Figure 4.16, including surface chlorophyll, NO_3, $Si(OH)_4$, NH_4, and bottom DO and DO saturation. Good correlations were found

between the modeled and observed results for NO_3^- near the surface and DO near the bottom. For the near-surface chlorophyll, the modeled and observed values have a similar range, but the data were relatively scattered with a global correlation coefficient of 0.4. The model-data correlation for the surface silicate was reasonably good (r=0.76), but the model tended to underestimate the peak of the silicate concentration. On the other hand, the model overestimated the lowest ammonium concentration near the surface. Unlike the dissolved oxygen concentration, for which a good correlation was found between the model prediction and observation, the model tended to underestimate the saturation of dissolved oxygen. The saturation of dissolved oxygen was not directly modeled, rather it is calculated based on temperature, salinity and DO data. Biases in the simulation of these different parameters could accumulate.

Annual cycles of key variables were plotted with the observation data for visual comparison (Figures 4.17-4.25). Chlorophyll concentration was broadly similar between the simulation and observation, but higher values observed at certain stations, particularly near the bottom, were not reproduced by the model, for example see N10, N07 and F06 in Figure 4.17. The model-data comparison results appeared to be better near the surface than near the bottom. At most monitoring stations, model-estimated and observed DIN matched well both near the bottom and near the surface (Figure 4.18). At F23, however, the simulation result was higher than the observed data in late winter. A week or two shift in the timing of the phytoplankton bloom and the drawdown of nutrient concentration could lead to the model-data deviation. Most of the DON and PON data were reproduced by the model (Figures 4.19 and 4.20). The model-estimated and observed DO concentrations compared relatively well in most cases (Figure 4.21). A noticeable deviation appeared in early April, when high values of DO, which may be linked to the spring phytoplankton bloom, were observed; however, the model underestimated its peak.

The model-data comparison of chlorophyll and DO concentrations in Boston Harbor (BH) is presented in Figures 4.22 and 4.23, with F23 representing a transition from BH to Massachusetts Bay. The chlorophyll concentration showed different seasonal variation in BH than in Massachusetts Bay. In BH, the spring and fall blooms showed similar peaks, and the chlorophyll concentration remained relatively high from spring to fall (Figure 4.22). As mentioned in Tian et al. (2009), the shallow depth and multiple anthropogenic and natural nutrient sources seem to contribute to sustained high primary production in the harbor during the summer. A reasonable model-data comparison result was reported for the DO concentration in BH, although the model tended to slightly overestimate the DO level in summer at a few stations (Figure 4.23). Unlike chlorophyll, the seasonal variation of the DO concentration in BH was similar to that in Massachusetts Bay. The higher chlorophyll concentration in summer, most likely from elevated phytoplankton production, did not result in increased DO concentration in summer as it did during the spring bloom. From this we infer that *in-situ* remineralization of organic substances, which also consumed DO, contributed much of the nutrients supporting the high phytoplankton production in summer in BH.

Sediment nutrient fluxes and oxygen demand (SOD) were observed (Tucker et al., 2009) at three stations in BH (BH02, BH03 and BH08A) and three stations in Massachusetts Bay (MB01, MB03 and MB05) (Figure 2.4). At the bay stations shown at the right side of the figure, the model-data comparison results were reasonably good with little seasonal variation (Figures 4.24 and 4.25). On the other hand, sediment nutrient fluxes and SOD were substantially higher during

summer and early fall at the harbor stations compared with the bay stations, in agreement with our assessment that remineralization contributed a substantial share in the increased nutrient supplies in summer in BH. The model simulation results compared relatively well with the observations for most sediment fluxes in BH, except at BH02 where the model underestimated the SOD flux in summer.

In summary, the UG-RCA 2008 simulation reproduced most of the observed magnitudes and seasonal variations of an array of parameters. For some specific cases, however, model-data deviation was evident, such as an underestimation of the chlorophyll and DO concentrations near the surface during the spring phytoplankton bloom and a general underestimation of bay sediment oxygen demand.

4.2.2 Model-predicted seasonal and interannual variability

Simulated seasonal variations of key variables (e.g. chlorophyll, DIN and DO) at 12 MWRA monitoring stations are displayed in Figures 4.26 through 4.35. These stations and include stations near the outfall site. In order to isolate interannual from inter-model variations, only the UG-RCA simulations of 2006 and 2008 are presented. These two years are very similar in the model results.

Seasonal variation. In 2008, the seasonal cycle of chlorophyll concentration was characterized by the spring and fall blooms and relatively low values in winter and summer (Figures 4.26 and 4.27). The spring bloom occurred mostly in late March and early April and lasted until late April. The onset of the fall bloom was not evident at most of the monitoring stations due to the gradual increase in the chlorophyll concentration from late August to late October, but the termination of the fall bloom in 2008 appeared to be abrupt with a sharp drop in the chlorophyll concentration in late October.

DIN (including NH_4^+, NO_2^- and NO_3^-) was replenished near the surface in winter, depleted in spring due to phytoplankton consumption, and increased in late fall as a result of multiple mechanisms such as strengthened vertical mixing, remineralization and decreased phytoplankton consumption (Figures 4.28 and 4.29). DIN near the bottom also showed high values in winter and late fall and low values in summer (Figures 4.30 and 4.31). Unlike the DIN near the surface which remained at a low level from late spring through early fall, the DIN concentration near the bottom gradually increased from summer to late fall. At the outfall site and nearby station N18, the DIN concentration near the bottom displayed high-frequency variations, which may be linked to the outfall effluent discharge.

The seasonal variation of the DO concentration differed from that of chlorophyll; DO exhibited high values during the spring phytoplankton bloom and low values in fall without response to the fall bloom at either surface or bottom (Figures 4.32-4.35). The high DO values in spring reflected production by phytoplankton photosynthesis. On the other hand, the low values of DO in fall were linked to multiple factors such as high surface and bottom temperature in early fall leading to low DO solubility, mixing that could prevent DO accumulation in the surface layer even when phytoplankton production was high, and increased remineralization of organic substances that consume DO.

4.2.3 Comparison with previous year simulations

In this section we compare the UG-RCA simulations of 2006 and 2008. We selected these two years because the simulations were carried out using the same model configuration: MB-FVCOM/UG-RCA. In most cases, the seasonal cycles of chlorophyll concentration were similar between 2006 and 2008 (Figures 4.26 and 4.27). Two notable differences were observed. First, the spring bloom started later by about 2 weeks in 2008 than in 2006 at certain stations (e.g., at F06 and F01), and the peak of the spring chlorophyll concentration appeared to be later by a week at all other stations. Secondly, the fall bloom declined gradually until the end of November in 2006 whereas it terminated abruptly at the end of October in 2008.

The seasonal cycles of DIN at both near-surface and near-bottom were similar between the two years (Figures 4.28-4.31). However, the DIN concentration in winter appeared to be higher in 2008 than in 2006 at most of the monitoring sites. The spring depletion of DIN was also later in 2008 than in 2006 at certain stations (e.g,, F01, F06 and F29), which was in agreement with the later spring phytoplankton bloom in 2008. In late fall, the DIN concentration was replenished near the surface earlier in 2008 than in 2006 at most of the monitoring stations, and the replenishment occurred within a short period of time, in agreement with the quick termination of the fall bloom in 2008.

The seasonal cycles of DO were quite similar between 2006 and 2008 (Figures 4.32-4.35). At the end of the year, however, DO was higher in 2008 than in 2006 at both near-surface and near-bottom. The period of high DO corresponded to that of the low chlorophyll and high nutrient concentrations. As a result, the increase in the DO concentration at the end of the year was not controlled by phytoplankton photosynthesis because the fall bloom terminated during that period of time. The mechanism leading to this increase in DO seemed to be linked to physical dynamics such as strong vertical mixing that increased the air-sea exchange, brought nutrients from the deep region to the surface and inhibited phytoplankton growth by reducing light exposure and low temperature.

5. Projection Experiments and Process Studies

5.1 Influences of the MWRA outfall on Massachusetts Bay

We have conducted a model run without MWRA effluent to assess the potential influence of the MWRA outfall on the water quality and ecosystem function in Massachusetts Bay. In this section, we refer the initial run with the MWRA outfall as the "control run" and the sensitivity-analysis run as the "non-sewage" run. We compared the chlorophyll concentration, dissolved inorganic nitrogen and DO between the two simulations. The intensities and seasonal variations of the chlorophyll concentration for these two runs were almost identical (Figure 5.1). Even though the two simulation lines were not fully superposed on each other as were those in the PAR- and SWR-driven simulation comparison (section 3.3), the difference between them remained negligible throughout the year.

The DIN concentration near the surface also compared fairly well between the two simulations (Figure 5.2). The results were the same in summer and fall. A noticeable difference was found in winter, during which the 'non-sewage" run predicted a slightly lower DIN concentration than the control run with the MWRA outfall. Near the bottom, the non-sewage run predicted a noticeably lower DIN concentration than the control run at N10, whereas the two predictions were quite similar at other stations (Figure 5.3). The DO results were practically identical between the two simulations (Figure 5.4). Although the time series of the DO concentration were not fully superposed, the difference between the non-sewage and control runs remained almost indistinguishable. Also, the simulation showed only small differences at mid-depth around the MWRA outfall (Figures 5.5 and 5.6). A slightly higher ammonium concentration in February and November and slightly higher chlorophyll concentration in May and August were barely perceptible around the MWRA outfall, but given the small range of the scale (-0.1 to +0.1 uM DIN or ug/l chlorophyll), these differences were negligible. As a general observation, the MWRA outfall does not seem to influence bay-wide water quality and ecosystem function. This is consistent with the before/after outfall statistical analyses conducted by Taylor (2004) and Libby et al. (2009).

5.2 Effect of reducing sampling sites on UG-RCA simulation

MWRA has proposed to EPA and the Massachusetts Department of Environmental Protection that a scaled back monitoring program is appropriate after many years of observing no adverse impact. One part of the proposal is to reduce the monitoring stations, parameters and cruise frequency. Basically, the total number of stations will be reduced from 33 to 14 with the following stations being removed: F03, F05, F07, F12, F14, F16, F17, F18, F19, F24, F25, F26, F27, F28, F30, F31, N10, N16, N20 (MWRA, 2009). Secondly, dissolved organic carbon, biogenic silica, primary production, and benthic nutrient and SOD fluxes will be removed from the observation parameters. Finally, all the remaining stations will be occupied 9 times per year instead of the present12 times at nearfield stations near the outfall and 6 times at the more distant farfield stations. The monitoring data are used to specify the boundary conditions to drive the model. This projection simulation was aimed at analyzing the potential impact of this amendment on the modeling results. By re-constructing the boundary conditions for water quality variables using the data after removal of those stations in the 2008 case, and comparing the model results for the cases with and without

removal of these data, we quantitatively estimated the change of the model simulation results over seasons.

It should be pointed out here that the analysis was done without considering changes in the monitored parameters. Dissolved organic carbon constitutes 4 state variables in the water quality model (Refractory, Labile, Reactive and Exudate) and biogenic silica is also a state variable. Without measurements of dissolved organic carbon and biogenic silica, we would need to develop an alternate method to construct boundary conditions for these variables, which was outside the scope of this experiment. Consequently, this projection analysis is based on all the parameters measured in 2008, but only with the stations and 3 nearfield cruises removed from the full data set according to the proposed amendment to the monitoring plan.

The comparison results show that the temporal and spatial distributions of the chlorophyll concentration were mostly comparable with the control run in terms of intensities and seasonal variations (Figure 5.7). The only difference is that the reduced-data run predicted slightly higher chlorophyll concentration in winter and slightly lower concentration during the spring phytoplankton bloom as well as at the end of the year. Similarly, the nutrient simulation results showed slightly lower values in winter and at the end of the year (Figures 5.8 and 5.9). As the physical conditions and biological processes were identical, the differences between the two runs were caused by changes in the boundary conditions. On the other hand, the DO simulation results were quite similar near the surface and bottom (Figures 5.10 and 5.11). Note that this projection run was based on the initial condition simulated from the full data set of 2007 and was run only for one year cycle. The projected results are valid only as a study of short-term influences. In addition, we did not examine the effect of deleting dissolved organic carbon and biogenic silica measurements from the monitoring program. Without these data, it would be necessary to construct boundary conditions for these parameters by some other method. For example, the past years' data and model runs could be used to develop a climatology. Or, the twenty years of monitoring data could be used to develop an empirical relationship between biogenic Si and SiO4 and between DOC and particulate organic carbon (POC).

5.3 Upwelling events

In Massachusetts Bay, southerly wind can cause upwelling and potentially bring nutrients from the deep region to the surface. This upwelling is one mechanism to stimulate phytoplankton growth near the surface in this area. The impact of upwelling is particularly noticeable during stratified seasons in summer and early fall. When the water column was fully mixed in winter, the effect of upwelling on nutrient and phytoplankton dynamics was limited due to homogenization of the water column and light limitation of phytoplankton growth. We plotted the hourly wind speed and direction during the entire year of 2008 (Figure 5.12). The wind speed rarely passed the critical value of 10 m/s for storm events; in contrast to previous years when a number of storm events occurred based on the same criterion (Butman et al., 2002, Chen et al., 2009a). From May to September, when upwelling events can potentially influence nutrient dynamics and phytoplankton development, four southerly wind events were identified: May 26-28, July 1-4, August 22-28 and September 11-15, respectively. We plotted the sea temperature near the surface during the same period of time and the results did not show any noticeable anomaly along the coastline (Figure 5.13). Based on the model prediction, upwelling events had limited effect on nutrient dynamics and phytoplankton production during the summer of 2008. On the other hand, Libby et al. (2009)

reported 2008 as a normal year in terms of upwelling index based on wind stress and water temperature measured at the NOAA buoy 44013.

6. Summary

To model calendar year 2008, we developed an unstructured grid version of RCA-v3 (called UG-RCA). RCA-v3 (HydroQual, 2004) has many superior functionalities to the previous version of RCA, but to ensure that results are comparable with past model runs, we re-ran 2006 using RCA-v3 and compared it with RCA-v2. Then, UG-RCA was validated by comparing its results with RCA-v3 and RCA-v2 by re-running the 2006 case using MB-FVCOM/UG-RCA and comparing it with ECOM-si/RCA-v2. The results for both models were comparable, except that, MB-FVCOM/UG-RCA provides higher-resolution model results in Massachusetts Bay.

RCA was initially coded to use total short-wave radiation (SWR) to drive photosynthesis and phytoplankton growth. Theoretically, only visible Photosynthetically Active Radiation (PAR) is active for photosynthesis and PAR should be used in modeling. In order to improve the coherence and theoretical soundness of RCA, we corrected the light function by using PAR to replace SWR in UG-RCA. The conversion factor from SWR to PAR was determined based on a long-term data set of remote sensing and MM5-WRF meteorological model predictions. Certain parameter values were also modified based on the same conversion factors in such a way that the results were identical between SWR- and PAR-driven simulations. Consequently, the shift from SWR to PAR did not create abrupt changes or discontinuities in the simulation.

The 2008 simulation was conducted using MB-FVCOM/UG-RCA. The surface forcing was essentially based on observational data collected at the NOAA buoy 44013 and WRF prediction, nutrient loadings based on the MWRA data set, and river discharges and the open boundary conditions established from the data collected during the MWRA monitoring program. The simulation was validated with (1) normalized root mean square error (NRMSE), (2) data-model regression analysis, and (3) visual comparison between data and model results over annual cycles. In general, the 2008 simulation was comparable with that of previous years in terms of NRMSE. In some cases, the NRMSE was slightly lower (better comparison) than that of previous years (e.g, chlorophyll and DO), and in some other cases somewhat higher than other simulations (e.g., NH_4). Good correlations were found between the modeled and observed results for NO_3^- (r=0.91) near the surface and DO (r=0.89) near the bottom. For chlorophyll near the surface, the range of modeled and observed values was similar, but the data were relatively scattered with a global correlation coefficient of 0.4. Visual comparisons show that the UG-RCA 2008 simulation reproduced most of the magnitudes and seasonal variations of the observations. For some specific cases, a deviation between simulation and data was observed, such as the underestimation of chlorophyll concentration and DO in surface waters during the spring phytoplankton bloom and underestimation of sediment oxygen demand in summer.

The seasonal variation of model predicted water quality variables was dominated by spring and fall phytoplankton blooms that were reflected by high chlorophyll concentration, which depleted nutrients near the surface in spring and kept nutrients at low levels in the fall. In general, the seasonal cycles of the chlorophyll concentration were similar between 2006 and 2008, but it seemed that the spring blooms started later and the fall bloom terminated earlier in 2008. Corresponding to the aforementioned shift in phytoplankton blooms, the DIN concentration in

winter appeared to be higher and the fall DIN replenishment occurred earlier in 2008 than in 2006. DO showed high values during the spring phytoplankton bloom due to photosynthetic production, but remained at a low level in fall without response to the fall bloom, which may be linked to multiple factors such as high DO consumption by increased remineralization and low DO solubility under high temperature. Similar seasonal variations were reported in 2006 and 2008, but at the end of the year, DO is higher in 2008 than in 2006 near the surface and bottom. This seemed to be linked to physical dynamics such as strong vertical mixing.

We conducted two projection simulations by (1) removing the MWRA outfall to examine its potential influences on water quality and ecosystem function in Massachusetts Bay and (2) reducing the number observational sites to evaluate the potential effect of an amended monitoring program on modeling performance. As a general observation, the MWRA outfall didn't seem to have a bay-wide substantial influence on the water quality and ecosystem function. Only limited changes in DIN concentration near the bottom close to the outfall were observed. The reduction in the data set did not result in dramatic changes in the simulation for short-term (1 year).

7. References

Alber M. and Chan A. 1994. Sources of contaminants to Boston Harbor: revised loading estimates. Boston: Massachusetts Water Resources Authority. Report 1994-01, 113pp.

Banks R. B. and Herrera F. F. 1977. Effect of wind and rain on surface reaeration. J. Envir. Engr. Div., ASCE. **103:** 489-504.

Blumberg A. F. 1994. A primer for ECOM-si. Technical Report, HydroQual, Inc. Mahwah, New Jersey, 101 pp.

Burchard H., Bolding K., Rippeth T.P., Stips A., Simpson J.H. and Sündermann J. 2002. Microstructure of turbulence in the Northern North Sea: a comparative study of observations and model simulations. J. Sea Res. 47, pp. 223–238.

Butman B., Bothner M.H. Lightsom F.L. Gutierrez B.T., Alexander P.S., Martini M.A. and Strahle, W.S. 2002. Long-term Oceanographic Observations in Western Massachusetts Bay offshore of Boston, Massachusetts: Data Repor for 1989-2000, U.S. Geological Survey Digital Data Series 74.

Chen C., Liu H. and Beardsley R. 2003. An unstructured grid, finite-volume, three dimensional, primitive equations ocean model: Application to coastal ocean and estuaries. Journal of Atmospheric and Ocean Technology, 20 (1), 159–186.

Chen C.**,** Beardsley R.C., Hu S., Xu Q. and Lin H. 2005. Using MM5 to hindcast the ocean surface forcing fields over the Gulf of Maine and Georges Bank region. *J. Atmos. Oceanic Technol.* 22: 131-145.

Chen C., Beardsley R.C. and Cowles G. 2006a. An unstructured grid, finite-volume coastal ocean model (FVCOM) system. Special Issue entitled “Advance in Computational Oceanography”, Oceanography, 19(1), 78-89.

Chen C., Beardsley R.C. and Cowles G. 2006b. An unstructured grid, finite-volume coastal ocean model-FVCOM user manual, School for Marine Science and Technology, University of Massachusetts Dartmouth, New Bedford, Second Edition. SMAST/UMASSD Technical Report-06-0602, 318 pp.

Chen C**,** Huang H., Beardsley R. C., Liu H., Xu Q. and Cowles G., 2007. A finite-volume numerical approach for coastal ocean ciirculation studies: comparisons with finite difference models. J. Geophys. Res. 112, C03018, doi:10.1029/2006JC003485.

Chen C., Beardsley R.C., Xu Q., Mickelson M.J., Tian R., Xue P., Cowles G.W. and Rothschild B.J. 2009a. The Massachusetts Bay hydrodynamic model: 2006-2007 simulation. Boston: Massachusetts Water Resources Authority. Report 2009-10. 77 p.

Chen C**.**, Malanotte-Rizzoli P., Wei J., Beardsley R.C., Lai Z., Xue P., Lyu S., Xu Q., Qi J. and Cowles G.W. 2009b. Application and comparison of Kalman filters for coastal ocean problems: An experiment with FVCOM, J. Geophys. Res., 114, C05011, doi:10.1029/2007JC004548.

Fairall C.W., Bradley E. F., Rogers D. P., Edson J. B. and Young G. S. 1996. Bulk parameterization of air–sea fluxes in TOGA COARE. J. Geophys. Res., 101, 3747–3767.

Fairall C.W., Bradley E. F., Hare J. E.,Grachev A. A. and Edson J. B. 2003. Bulk Parameterization

of Air–Sea Fluxes: Updates and Verification for the COARE Algorithm. Journal of Climate 2003; 16: 571-591.

Frouin R., Franz B., and Wang M. no date. www.oceancolor.gsfc.nasa.gov/DOCS/seawifs_par_wfigs.pdf.

Gao G., Chen C., Qi J. and Beardsley R. C. 2010. Development of Unstructured-grid Version CICE: Validation and Applications, Submitted to *J. Geophys. Res.*

Hendry R. and He I. 1996. Technical report on objective analysis (OA) project, Bedford Institute of Oceanography, Dartmouth, Nova Scotia, 105pp.

Huang H., Chen C., Colwes G. W., Winant C. D., Beardsley R. C., Hedstrom K. S. and Haidvogel D. B. 2008. FVCOM validation experiments: comparisons with ROMS for three idealized barotropic test problems. J. Geophys. Res., 113, C07042, doi: 10.1029/2007JC004557.

Hyer P.V., Fang C. S., Ruzeck E. P. and Hargis W. J. 1971. Hydrography and hydrodynamics of Virginia estuaries, studies of the distribution of salinity and dissolved oxygen in the upper York system. Gloucester Point, VA:Virginia Institute of Marine Science.

HydroQual, Inc. and Normandeau Associates, Inc. 1993, A water quality model for Massachusetts and Cape Cod Bays. Boston, Massachusetts Water Resources Authority. Report 1993-05, 222pp.

HydroQual, Inc. and Normandeau Associates, Inc. 1995. A water quality model for Massachusetts and Cape Cod Bays: Calibration of the Bay Eutrophication Model (BEM). Boston: Massachusetts Water Resources Authority. Report 1995-08. 402 p.

HydroQual, Inc. 2000. Bays Eutrophication Model (BEM): modeling analysis for the period 1992-1994. Boston, Massachusetts Water Resources Authority. Report 2000-02, 158pp.

HydroQual, Inc. 2003. Bays Eutrophication Model (BEM): modeling analysis for the period 1998-1999. Boston, Massachusetts Water Resources Authority. Report 2003-03, 318pp.

HydroQual Inc. 2004. Users' guide for RCA release 3.0. Mahwah, NJ, 217p.

Jiang M. S. and Zhou M. 2003. Massachusetts Bay Hydrodynamic Model and Water Quality Model results in 1998-99: Comparison Report between HydroQual and University of Massachusetts Boston Runs. Boston: Massachusetts Water Resources Authority. Report 2003-10, 42pp.

Jiang M.S. and Zhou M. 2004a. Calibration of the Massachusetts and Cape Cod Bays Hydrodynamic Model: 2000-2001. Boston: Massachusetts Water Resources Authority. Report 2004-08. 71pp.

Jiang M.S. and Zhou M. 2004b. Calibration of the Massachusetts and Cape Cod Bays water quality model: 2000-2001. Boston: Massachusetts Water Resources Authority. Report 2004-09. 90pp.

Jiang M.S. and Zhou M. 2006a. The Massachusetts and Cape Cod Bays hydrodynamic model: 2002-2004 simulation. Boston: Massachusetts Water Resources Authority. Report 2006-12. 128 p.

Jiang M.S. and Zhou M. 2006b. Bays Eutrophication Model: 2002-2004 simulation. Boston: Massachusetts Water Resources Authority. Report 2006-13. 126 p.

Jiang M. and Zhou M. 2008a. The Massachusetts and Cape Cod Bays hydrodynamic model: 2005 simulation. Boston: Massachusetts Water Resources Authority. Report 2008-12. 58 p.

Jiang M. and Zhou M. 2008b. Massachusetts Bay Eutrophication Model: 2005 simulation. Boston: Massachusetts Water Resources Authority. Report 2008-13. 82 p. Report 2008-12., 118pp.

Lai Z., Chen C., Cowles G. and Beardsley R. C. Submitted. A Non-Hydrostatic Version of FVCOM, Part I: Validation Experiments (submitted to Journal of Geophysical Research-Oceans, in revision).

Laws E.A. and Chalup M.S. 1990. A microalgal growth model. Limnol. Oceanogr. 35, 597-608.

Libby P.S., Anderson D.M., Borkman D.G., Geyer W.R., Keller A.A., Oviatt C.A. and Turner J.T. 2009. 2008 Water Column Monitoring Results. Boston: Massachusetts Water Resources Authority. Report 2009-12. 31p. plus appendices.

Mellor G. L. and Yamada T. 1982. Development of a turbulence closure model for geophysical fluid problems. Rev. Geophys. Space Phys., 20, 851-875.

Menzie-Cura. 1991. Sources and loadings of pollutants to Massachusetts Bays. Boston: Massachusetts Bays Program. Report MBP-91-01, 266pp.

MWRA 2009. 2009 Annual list of proposed changes to MWRA's Effluent Outfall Ambient Monitoring Plan, October 23, 2009. http://www.mwra.com/harbor/pdf/omsap/amp_prop_mod_list_20091023.pdf

Pietrzak J., Jakobson J.B., Burchard H., Vested H.J. and Peterson O. 2002. A three-dimensional hydrostatic model for coastal and ocean modeling using a generalized topography following coordinate system. Ocean Modelling 4**,** pp. 173–205.

Qi J., Chen C., , Beardsley R. C., Perrie W. and Cowles G. 2009. An unstructured-grid finite-volume surface wave model (FVCOM-SWAVE): implementation, valida.tions and applications. Ocean Modelling, 28, 153-166. doi:10.1016/j.ocemod.2009.01.007.

Sea-Bird Electronic Inc, 2007. PAR Light Sensors. Application note No. 11 General. Bellevue, WA.

Smagorinsky J. 1963. General circulation experiments with the primitive equations, I. The basic experiment. Monthly Weather Review, 91, 99–164.

Signell R.P., Jenter H. L. and Blumberg A. F. 1996. Circulation and effluent dilution modeling in Massachusetts Bay: model implementation, verification and results. USGS Open File Report 96-015, U.S. Geological Survey, Woods Hole.

Taylor D.I. 2004. Harbor-Bay eutrophication-related water chemistry changes after 'offshore transfer'. Boston: Massachusetts Water Resources Authority. Report 2004-06, 83 p.

Tian R.C., Chen C.S., Xu Q.C., Xue P.F., Cowles G.W., Beardsley R. and Rothschild B. 2009. Massachusetts Bay Eutrophication Model: 2006-2007 Simulation. Boston: Massachusetts Water Resources Authority. Report 2009-11. 147p.

Tucker J., Kelsey S. and Giblin A.E. 2009. 2008 Annual benthic nutrient flux monitoring: summary report. Boston: Massachusetts Water Resources Authority. Report 2009-08. 31 p.

Table 2.1 Comparison of functionality between UG-RCA and RCA-v2.

UG-RCA & RCA-v3	RCA-v2
Multiple modules: • Eutrophication • Pathogens • Tracer • Residence Time	Only one program: • Eutrophication
Number of phytoplankton groups: • Flexible	Number of phytoplankton groups: • Three
Two phytoplankton growth functions: • Standard • Laws-Chalup function.	One phytoplankton growth function: • Laws-Chalup function.
Multiple reaeration formulations: • Constant in time and space • Constant in time but varies spatially • Driven by current shear • Driven by wind stress (The latter two vary with time and space)	One reaeration formulation: • Driven by wind-stress
Multiple light attenuation functions: • Constant • Spatially variable • Temporally variable • 4D resolved.	One light attenuation function: • Spatially variable.

Table 2.2 State variable numbers in the different water quality models

RCA-2 number	UG-RCA & RCA-3 number.	UG-RCA & RCA-3 variable
1	1	Salinity
2	2	Winter/spring phytoplankton
3	3	Summer phytoplankton
26	4	Fall phytoplankton
4	5	Refractory POP
5	6	Labile POP
6	7	Refractory DOP
7	8	Labile DOP
8	9	PO4
9	10	Refractory PON
10	11	Labile PON
11	12	Refractory DON
12	13	Labile DON
13	14	Total ammonia
14	15	Nitrite + nitrate
15	16	Biogenic silica
16	17	Total silica
17	18	Refractory POC
18	19	Labile POC
19	20	Refractory DOC
20	21	Labile DOC
22	22	Exudate DOC
21	23	Reactive DOC
	24	Reactive POC
23	25	O_2* - aqueous oxygen
24	26	Dissolved oxygen
25		Total active metal (TAM)

Table 2.3 Parameter definition, symbols, values and units in RCA-v3 and UG-RCA, and in RCA-v2. Where values used in RCA differ from those used in UG-RCA, they are shown in parentheses.

UG-RCA order	Parameter definition	UG-RCA RCA-v3 symbol	Value	Unit	RCA-v2 symbol
1	MODEL OPTION	AGMOPT	1		-
2	Phytoplankton categories	ACTALG	3		-
3	REAERATION FORMULATION	KAOPT	3		-
4	EXTINCTION COEFFICIENT	KEOPT	1		-
5	PAR FRACTION	PAR	0.437		-
9	GROWTH TEMPERATURE FOR DIATOMS	TOPT1	8.000	^oC	TOPT1
10	TEMPERATURE CORRECTION EFFECT ON GROWTH RATE BELOW TOPT1	K1BETA1	0.004	$^oC^{-2}$	K1TX1
11	TEMPERATURE CORRECTION EFFECT ON GROWTH RATE ABOVE TOPT1	K1BETA2	0.006	$^oC^{-2}$	K1TX2
12	GROSS PHOTOSYNTHETIC RATE PER UNIT CELL (ASSOCIATED WITH PHOTOSYNTHETIC DARK REACTIONS)	GPRE1	2.5	d^{-1}	GPRE1
13	GROSS PHOTOSYNTHETIC RATE PER UNIT CELL PER UNIT LIGHT INTENSITY UNDER NUTRIENT-SATURATED CONDITIONS AND ZERO IRRADIANCE	GPR01	0.64 (0.28)	m^2 Ein^{-1}	GPR01
14	SATURATING ALGAL LIGHT INTENSITY	IS1	0.000	Ein m^{-2} d^{-1}	IS1
15	HALF SATURATION CONSTANT FOR NITROGEN	KMN1	0.010	mg N l^{-1}	KMN1
16	HALF SATURATION CONSTANT FOR PHOSPHOROUS	KMP1	0.001	mg P l^{-1}	KMP1
17	HALF SATURATION CONSTANT FOR SILICA	KMS1	0.020	mg Si l^{-1}	KMS1
18	BASAL OR RESTING RESPIRATION RATE	K1RB	0.030	d^{-1}	K1RB
19	TEMPERATURE COEFFICIENT FOR BASAL/ENDOGENOUS RESPIRATION	K1RT	1.0	dimensionless	-
20	GROWTH-RATE-DEPENDENT RESPIRATION COEFFICIENT	K1RG	0.280	dimensionless	K1RG
21	DEATH RATE DUE TO GRAZING	K1GRZC	0.100	d^{-1}	K1GRZC
22	TEMPERATURE COEFFICIENT	K1GRZT	1.100	dimensionless	K1GRZT
23	FRACTION OF C ALLOCATED TO STRUCTURAL PURPOSES	FSC1	0.10	dimensionless	FSC1
24	CARBON TO CHLOROPHYLL RATIO	WCCHL1	40.0	mg C (mg chl)$^{-1}$	WCCHL1
25	CARBON TO PHOSPHORUS RATIO - NON-P LIMITED	WCP1	40.0	mg C (mg P)$^{-1}$	WCP1
26	CARBON TO NITROGEN RATIO - NON-N LIMITED	WCN1	5.0	mg C (mg N)$^{-1}$	WCN1
27	CARBON TO SILICA RATIO - NON-SI LIMITED	WCS1	2.500	mg C (mg Si)$^{-1}$	WCS1
28	QUOTIENT OF NUTRIENT-LIMITED NUTRIENT:C RATIOS AT RELATIVE GROWTH RATES OF 0 AND 1	QF1	0.85		QF1
29	CHLOROPHYLL SELF-SHADING EXTINCTION COEFFICIENT FOR ALGAL GROUP 1	XKC1	0.017	m^2 (mg chl) $^{-1}$	XKC
30	BASE ALGAL SETTLING RATE - GROUP 1	VSBAS1	0.500	m d^{-1}	VSBAS1

UG-RCA order	Parameter definition	UG-RCA RCA-v3 symbol	Value	Unit	RCA-v2 symbol
31	NUTRIENT STRESSED ALGAL SETTLING RATE - GROUP 1	VSNTR1	1.000	$m\ d^{-1}$	VSNTR1
	Algal Group 2				
41	OPTIMAL GROWTH TEMPERATURE FOR SUMMER GROUP 2	TOPT2	18.000	^oC	TOPT2
42	TEMPERATURE CORRECTION EFFECT ON GROWTH RATE BELOW TOPT2	K2BETA1	0.004	$^oC^{-2}$	K2TX1
43	TEMPERATURE CORRECTION EFFECT ON GROWTH RATE ABOVE TOPT2	K2BETA2	0.006	$^oC^{-2}$	K2TX2
44	GROSS PHOTOSYNTHETIC RATE PER UNIT CELL (ASSOCIATED WITH PHOTOSYNTHETIC DARK REACTIONS)	GPRE2	3.0	d^{-1}	GPRE2
45	PHOTOSYNTHETIC RATE PER UNIT CELL PER UNIT LIGHT INTENSITY UNDER NUTRIENT-SATURATED CONDITIONS AND ZERO IRRADIANCE	GPR02	0.64 (0.28)	$m^2\ Ein^{-1}$	GPR02
46	SATURATING ALGAL LIGHT INTENSITY	IS2	000.0	$Ein\ m^{-2}\ d^{-1}$	IS2
47	HALF SATURATION CONSTANT FOR NITROGEN	KMN2	0.010	$mg\ N\ l^{-1}$	KMN2
48	HALF SATURATION CONSTANT FOR PHOSPHOROUS	KMP2	0.001	$mg\ P\ l^{-1}$	KMP2
49	HALF SATURATION CONSTANT FOR SILICA	KMS2	0.005	$mg\ Si\ l^{-1}$	KMS2
50	BASAL OR RESTING RESPIRATION RATE	K2RB	0.036	d^{-1}	K2RB
51	TEMPERATURE COEFFICIENT FOR BASAL/ENDOGENOUS RESPIRATION	K2RT	1.0		-
52	GROWTH-RATE-DEPENDENT RESPIRATION COEFFICIENT	K2RG	0.280		K2RG
53	DEATH RATE DUE TO GRAZING	K2GRZC	0.100	d^{-1}	K2GRZC
54	TEMPERATURE COEFFICIENT	K2GRZT	1.100		K2GRZT
55	FRACTION OF C ALLOCATED TO STRUCTURAL PURPOSES	FSC2	0.10		FSC2
56	CARBON TO CHLOROPHYLL RATIO	WCCHL2	65.0	$mg\ C\ (mg\ chl)^{-1}$	WCCHL2
57	CARBON TO PHOSPHORUS RATIO - NON-P LIMITED	WCP2	40.000	$mg\ C\ (mg\ P)^{-1}$	WCP2
58	CARBON TO NITROGEN RATIO - NON-N LIMITED	WCN2	5.670	$mg\ C\ (mg\ N)^{-1}$	WCN2
59	CARBON TO SILICA RATIO - NON-SI LIMITED	WCS2	7.000	$mg\ C\ (mg\ Si)^{-1}$	WCS2
60	QUOTIENT OF NUTRIENT-LIMITED NUTRIENT:C RATIOS AT RELATIVE GROWTH RATES OF 0 AND 1	QF2	0.85		QF2
61	CHLOROPHYLL SELF-SHADING EXTINCTION COEFFICIENT FOR ALGAL GROUP 2	XKC2	0.017	$m^2\ (mg\ chl)^{-1}$	XKC
62	BASE ALGAL SETTLING RATE - GROUP 2	VSBAS2	0.300	$m\ d^{-1}$	VSBAS2
63	NUTRIENT STRESSED ALGAL SETTLING RATE - GROUP 2	VSNTR2	0.700	$m\ d^{-1}$	VSNTR2
	Algal Group 3				
73	OPTIMAL GROWTH TEMPERATURE FOR DIATOMS	TOPT3	14.0	^oC	TOPT3
74	TEMPERATURE CORRECTION EFFECT ON GROWTH RATE BELOW TOPT3	K3BETA1	0.004	$^oC^{-2}$	K3TX1
75	TEMPERATURE CORRECTION EFFECT ON GROWTH RATE ABOVE TOPT3	K3BETA2	0.006	$^oC^{-2}$	K3TX2

UG-RCA order	Parameter definition	UG-RCA RCA-v3 symbol	Value	Unit	RCA-v2 symbol
76	GROSS PHOTOSYNTHETIC RATE PER UNIT CELL (ASSOCIATED WITH PHOTOSYNTHETIC DARK REACTIONS)	GPRE3	2.5	d^{-1}	GPRE3
77	GROSS PHOTOSYNTHETIC RATE PER UNIT CELL PER UNIT LIGHT INTENSITY UNDER NUTRIENT-SATURATED CONDITIONS AND ZERO IRRADIANCE	GPR03	0.64 (0.28)	m^2 Ein^{-1}	GPR03
78	SATURATING ALGAL LIGHT INTENSITY	IS3	000.0	Ein m^{-2} d^{-1}	IS3
79	HALF SATURATION CONSTANT FOR NITROGEN	KMN3	0.005	mg N l^{-1}	KMN3
80	HALF SATURATION CONSTANT FOR PHOSPHOROUS	KMP3	0.001	mg P l^{-1}	KMP3
81	HALF SATURATION CONSTANT FOR SILICA	KMS3	0.040	mg Si l^{-1}	KMS3
82	BASAL OR RESTING RESPIRATION RATE	K3RB	0.030	d^{-1}	K3RB
83	TEMPERATURE COEFFICIENT FOR BASAL/ENDOGENOUS RESPIRATION	K3RT	1.0	dimensionless	-
84	GROWTH-RATE-DEPENDENT RESPIRATION COEFFICIENT	K3RG	0.280	dimensionless	K3RG
85	DEATH RATE DUE TO GRAZING	K3GRZC	0.100	d^{-1}	K3GRZC
86	TEMPERATURE COEFFICIENT	K3GRZT	1.100	dimensionless	K3GRZT
87	FRACTION OF C ALLOCATED TO STRUCTURAL PURPOSES	FSC3	0.10	dimensionless	FSC3
88	CARBON TO CHLOROPHYLL RATIO	WCCHL3	15.0	mg C (mg chl)$^{-1}$	WCCHL3
89	CARBON TO PHOSPHORUS RATIO - NON-P LIMITED	WCP3	40.000	mg C (mg P)$^{-1}$	WCP3
90	CARBON TO NITROGEN RATIO - NON-N LIMITED	WCN3	5.670	mg C (mg N)$^{-1}$	WCN3
91	CARBON TO SILICA RATIO - NON-SI LIMITED	WCS3	2.500	mg C (mg Si)$^{-1}$	WCS3
92	QUOTIENT OF NUTRIENT-LIMITED NUTRIENT:C RATIOS AT RELATIVE GROWTH RATES OF 0 AND 1	QF3	0.85		QF3
93	CHLOROPHYLL SELF-SHADING EXTINCTION COEFFICIENT FOR ALGAL GROUP 3	XKC3	0.017	m^2 (mg chl) $^{-1}$	XKC
94	BASE ALGAL SETTLING RATE - GROUP 3	VSBAS3	0.300	m d^{-1}	VSBAS3
95	NUTRIENT STRESSED ALGAL SETTLING RATE - GROUP 3	VSNTR3	1.000	m d^{-1}	VSNTR3
	Biogeochemical parameters				
105	HALF SATURATION CONSTANT FOR PHYTOPLANKTON RECYCLE FRACTIONS MG C/L	KMPHYT	0.050	mg C l^{-1}	KMPHYT
106	REFRACTORY PARTICULATE ORGANIC PHOSPHOROUS	FRPOP	0.150		FRPOP
107	LABILE PARTICULATE ORGANIC PHOSPHOROUS	FLPOP	0.300		FLPOP
108	REFRACTORY DISSOLVED ORGANIC PHOSPHOROUS	FRDOP	0.100		FRDOP
109	LABILE DISSOLVED ORGANIC PHOSPHOROUS	FLDOP	0.150		FLDOP
110	DISSOLVED INORGANIC PHOSPHOROUS	FPO4	0.300		FPO4
111	REFRACTORY PARTICULATE ORGANIC NITROGEN	FRPON	0.150		FRPON
112	LABILE PARTICULATE ORGANIC NITROGEN	FLPON	0.325		FLPON

UG-RCA order	Parameter definition	UG-RCA RCA-v3 symbol	Value	Unit	RCA-v2 symbol
113	REFRACTORY DISSOLVED ORGANIC NITROGEN	FRDON	0.150		FRDON
114	LABILE DISSOLVED ORGANIC NITROGEN	FLDON	0.175		FLDON
115	AMMONIA	FNH4	0.200		FNH3
116	REFRACTORY PARTICULATE ORGANIC CARBON	FRPOC	0.150		FRPOC
117	LABILE PARTICULATE ORGANIC CARBON	FLPOC	0.350		FLPOC
118	REFRACTORY DISSOLVED ORGANIC CARBON	FRDOC	0.100		FRDOC
119	LABILE DISSOLVED ORGANIC CARBON PHOSPHORUS	FLDOC	0.400		FLDOC
120	HYDROLYSIS RATE OF RPOP TO RDOP	K57C	0.010	d^{-1}	K46C
121	TEMPERATURE COEFFICIENT	K57T	1.080		K46T
122	HYDROLYSIS RATE OF LPOP TO LDOP	K68C	0.050	d^{-1}	K57C
123	TEMPERATURE COEFFICIENT	K68T	1.080		K57T
124	MINERALIZATION RATE OF RDOP TO PO4	K79C	0.010	d^{-1}	K68C
125	TEMPERATURE COEFFICIENT	K79T	1.080		K68T
126	MINERALIZATION RATE OF LDOP TO PO4	K89C	0.100	d^{-1}	K78C
127	TEMPERATURE COEFFICIENT NITROGEN	K89T	1.080		K78T
128	HYDROLYSIS RATE OF RPON TO RDON	K1012C	0.008	d^{-1}	K911C
129	TEMPERATURE COEFFICIENT	K1012T	1.080		K911T
130	HYDROLYSIS RATE OF LPON TO LDON	K1113C	0.050	d^{-1}	K1012C
131	TEMPERATURE COEFFICIENT	K1113T	1.080		K1012T
132	MINERALIZATION RATE of RDON TO NH4	K1214C	0.008	d^{-1}	K1113C
133	TEMPERATURE COEFFICIENT	K1214T	1.080		K1113T
134	MINERALIZATION RATE OF LDON TO NH4	K1314C	0.050	d^{-1}	K1213C
135	TEMPERATURE COEFFICIENT NITRIFICATION/DENITRIFICATION RATES	K1314T	1.080		K1213T
136	NITRIFICATION RATE AT 20 DEG C	K1415C	0.100	d^{-1}	K1314C
137	TEMPERATURE COEFFICIENT	K1415T	1.080		K1314T
138	HALF SATURATION CONSTANT FOR NITRIF- ICATION OXYGEN LIMITATION	KNIT	1.000	mg O_2 l^{-1}	KNIT
139	DENITRIFICATION RATE AT 20 DEG C	K150C	0.050	d^{-1}	K140C
140	TEMPERATURE COEFFICIENT	K150T	1.045		K140T
141	MICHAELIS CONSTANT FOR DENITRIFICATION OXYGEN LIMITATION SILICA MINERALIZATION RATES AT 20 DEG C	KNO3	0.100	mg O_2 l^{-1}	KNO3
142	MINERALIZATION RATE OF BIOGENIC SI TO AVAIL SI	K1617C	0.080	d^{-1}	K1516C
143	TEMPERATURE COEFFICIENT CARBON HYDROLYSIS/OXIDATION RATES AT 20 DEG C	K1617T	1.080		K1516T
144	HYDROLYSIS RATE OF RPOC TO RDOC	K1820C	0.010	d^{-1}	K1719C
145	TEMPERATURE COEFFICIENT	K1820T	1.080		K1719T
146	HYDROLYSIS RATE OF LPOC TO LDOC	K1921C	0.070	d^{-1}	K1820C
147	TEMPERATURE COEFFICIENT	K1921T	1.080		K1820T
148	OXIDATION RATE OF RDOC	K200C	0.008	d^{-1}	K190C
149	TEMPERATURE COEFFICIENT	K200T	1.080		K190T
150	OXIDATION RATE OF LDOC	K210C	0.100	d^{-1}	K200C
151	TEMPERATURE COEFFICIENT	K210T	1.080		K200T
152	MICHAELIS CONSTANT FOR LDOC	KMLDOC	0.100	mg C l^{-1}	KMLDOC
153	HALF SATURATION CONSTANT FOR ORG CARBON	KDOC	0.200	mg O_2 l^{-1}	KDOC
154	ALGAL EXUDATE DOC OXIDATION RATE	K220C	0.300	d^{-1}	K220C
155	TEMPERATURE COEFFICIENT	K220T	1.047		K220T

UG-RCA order	Parameter definition	UG-RCA RCA-v3 symbol	Value	Unit	RCA-v2 symbol
156	FRACTION OF PRIMARY PRODUCTIVITY GOING TO LABILE ORGANIC CARBON VIA EXUDATION REPOC/REDOC ARE ASSOCIATED WITH SANITARY/CSO SOLIDS	FLOCEX	0.100		FLOCEX
157	HYDROLYSIS RATE OF REPOC TO REDOC	K2324C	0.01	d^{-1}	-
158	TEMPERATURE COEFFICIENT	K2324T	1.0		-
159	REACTIVE DOC OXIDATION RATE	K240C	0.150	d^{-1}	K210C
160	TEMPERATURE COEFFICIENT	K240T	1.047		K210T
161	CARBON TO PHOSPHORUS RATIO OF CSO SOLIDS	CTOPCSO	0.0		-
162	CARBON TO NITROGEN RATIO OF CSO SOLIDS	CTONCSO	0.0		-
163	OXIDATION RATE FOR AQUEOUS SOD	K250C	0.150	d^{-1}	K230C
164	TEMPERATURE COEFFICIENT	K250T	1.080		K230T
165	HALF SATURATION CONSTANT FOR O2*	KO2EQ	0.100	mg O_2 l^{-1}	KO2EQ
166	MINIMUM VALUE FOR KL	KLMIN	0.0	m d^{-1}	-
167	DIFFUSIVITY OF OXYGEN ACROSS THE AIR-WATER INTERFACE	DIFUS	0.0	m^2 d^{-1}	-
168	TEMPERATURE CORRECTION COEFFICIENT FOR ATMOSPHERIC REAERATION	KAT	1.024		KAT
169	TEMPERATURE CORRECTION	VSBAST	1.027		VSBAST
170	PARTICULATE ORGANIC MATTER SETTLING RATE	VSPOM	1.000	m d^{-1}	VSPOM
171	TEMPERATURE CORRECTION	VSPMT	1.027		VSPMT
172	TEMPERATURE CORRECTION FOR DEPOSITION TO SEDIMENT	VSSEDT	1.027		VSSEDT
173	POWER COEFF. FOR CSO SOLID SETTLING RATE (>=1	BVCSO	1.0	dimensionless	-
174	CRITICAL REPOC CONC. FOR CSO SETTLING FUNCTION	CRCSO	1.0	mg C l^{-1}	-
175	MINIMUM SETTLING RATE FOR CSO SOLIDS Vcso = VMINCSO+(VMAXCSO-VMINCSO)*(REPOC/CRCSO)**BVCSO)	VMINCSO	0.0	m d^{-1}	-
176	MAXIMUM SETTLING RATE FOR CSO SOLIDS	VMAXCSO	0.0	m d^{-1}	
177	PARTITION COEFFICIENT FOR SORBED PHOSPHORUS	KADPO4	6.0	l mg SS^{-1}	KADPO4
178	PARTITION COEFFICIENT FOR SORBED SILICA	KADSI	6.0	l mg SS^{-1}	KADSI
179	SETTLING RATE FOR PHOSPHORUS/SILICA SORBED TO SUSPENDED SOLIDS	VSPIM	0.0	m d^{-1}	VSPIM
180	BASE (CHL-A CORRECTED) EXTINCTION COEFFICIENT (USED WHEN KEOPT=0,2)	KECONST	0.001	m^{-1}	-
	RCA v2 unique parameters				
	SOLUBILITY OF TAM UNDER ANOXIC CONDITIONS	-	1.5	mol l^{-1}	DTAMMX
	CONSTANT THAT RELATES TAM SOLUBILITY TO DO	-	1.5	l (mg DO) $^{-1}$	KDOTAM
	ANOXIC TAM RELEASE RATE AT REFERENCE TEMP	-	0.004	Mol (m^2 d)$^{-1}$	JTAMC

UG-RCA order	Parameter definition	UG-RCA RCA-v3 symbol	Value	Unit	RCA-v2 symbol
	TEMPERATURE COEFFICIENT	-	1.027		JTAMT
	HALF SATURATION CONSTANT FOR TAM RELEASE	-	1.027	mg DO l^{-1}	KTAM

Table 2.4 Data-model conversion for the MWRA effluent, rivers, and other sources.

Model			Conversion	Data	
Variable	Definition	Units	Function	Variable	Units
Flow	Sewage flow	L day^{-1}	3.785mflow	mflow	gallon d^{-1}
TOC	Total organic C	mg C d^{-1}	0.7CBOD+18	CBOD	mg O d^{-1}
RPOC	Refractory POC	mg C d^{-1}	9	CBOD	mg O d^{-1}
LPOC	Labile POC	mg C d^{-1}	0.198CBOD	CBOD	mg O d^{-1}
RDOC	Refractory DOC	mg C d^{-1}	9	CBOD	mg O d^{-1}
LDOC	Labile DOC	mg C d^{-1}	0.132CBOD	CBOD	mg O d^{-1}
REDOC	Reactive DOC	mg C d^{-1}	0.37CBOD	CBOD	mg O d^{-1}
TON	Total organic N	mg N d^{-1}	(TKN-NH4)/1000	TKN	μg N d^{-1}
RPON	Refractory PON	mg N d^{-1}	0.4(TKN-NH4)/1000	TKN	μg N d^{-1}
LPON	Labile PON	mg N d^{-1}	0.4(TKN-NH4)/1000	TKN	μg N d^{-1}
RDON	Refractory DON	mg N d^{-1}	0.1(TKN-NH4)/1000	TKN	μg N d^{-1}
LDON	Labile DON	mg N d^{-1}	0.1(TKN-NH4)/1000	TKN	μg N d^{-1}
TOP	Total organic P	mg P d^{-1}	(TP-PO4)/1000	TP	μg P d^{-1}
RPOP	Refractory DOP	mg P d^{-1}	0.3(TP-PO4)/1000	TP	μg P d^{-1}
LPOP	Labile DOP	mg P d^{-1}	0.55(TP-PO4)/1000	TP	μg P d^{-1}
RDOP	Refractory DOP	mg P d^{-1}	0.05(TP-PO4)/1000	TP	μg P d^{-1}
LDOP	Labile DOP	mg P d^{-1}	0.1(TP-PO4)/1000	TP	μg P d^{-1}

Table 2.5 Partition coefficients for organic substances.

		Labile	Refractory	Reactive	Exudate
Nitrogen	PON	0.5	0.5		
	DON	0.5	0.5		
Phosphorus	POP	0.647	0.353		
	DOP	0.66	0.33		
Carbon	POC	0.4	0.6	-	-
	DOC	0.2	0.7	0.05	0.05

Table 2.6 Partition coefficients of chlorophyll to phytoplankton groups at the open boundary.

	Winter-spring group	Summer group	Fall group
January-April	1.0	0	0
May	0.5	0.5	0
June-July	0	1.0	0
August	0	0.5	0.5
September-November	0	0	1.0
December	0.5	0	0.5

Table 3.1 Normalized root mean square error between simulation and observation. Values > 1 indicate model error higher than the data range. Shading highlights the higher value for 2006.

Parameter	Season	RCA		UG-RCA			
		2006		2006		2008	
		Surface	Bottom	Surface	Bottom	Surface	Bottom
Chl	Winter	0.45	0.43	0.60	0.73	0.57	0.66
	Spring	0.36	0.33	0.25	0.32	0.24	0.29
	Summer	0.65	0.60	0.45	0.58	0.43	0.52
	Fall	0.88	0.79	0.78	0.99	0.74	0.90
	Annual	0.20	0.18	0.17	0.17	0.16	0.15
DO	Winter	0.70	0.53	1.14	1.1 3	0.97	0.93
	Spring	0.31	0.25	0.37	0.37	0.32	0.30
	Summer	1.04	0.79	0.90	0.90	0.77	0.74
	Fall	0.51	0.38	0.87	0.87	0.74	0.71
	Annual	0.15	0.10	0.17	0.16	0.15	0.14
NO3	Winter	0.25	0.33	0.24	0.38	0.23	0.30
	Spring	0.39	0.49	0.36	0.46	0.35	0.37
	Summer	0.48	0.51	0.49	0.54	0.47	0.44
	Fall	0.39	0.45	0.38	0.55	0.38	0.45
	Annual	0.14	0.17	0.15	0.22	0.14	0.18
NH4	Winter	0.33	0.27	0.33	0.98	0.46	0.89
	Spring	0.40	0.30	0.76	1.74	1.06	1.67
	Summer	0.44	0.36	0.29	0.85	0.41	0.78
	Fall	0.38	0.33	0.33	1.11	0.45	1.01
	Annual	0.18	0.14	0.15	0.43	0.21	0.39
PON	Winter	0.50	0.53	0.61	0.63	0.57	0.59
	Spring	0.64	0.38	0.78	0.40	0.27	0.37
	Summer	0.60	0.60	0.64	0.71	0.61	0.47
	Fall	0.88	1.28	1.18	1.05	1.11	0.99
	Annual	0.26	0.20	0.21	0.29	0.13	0.20
DON	Winter	0.72	0.80	0.36	0.60	0.27	0.47
	Spring	0.97	0.71	1.45	0.75	1.07	0.57
	Summer	0.45	0.36	1.64	0.56	1.21	0.47
	Fall	1.25	0.68	0.65	0.40	0.48	0.32
	Annual	0.18	0.15	0.21	0.22	0.17	0.13

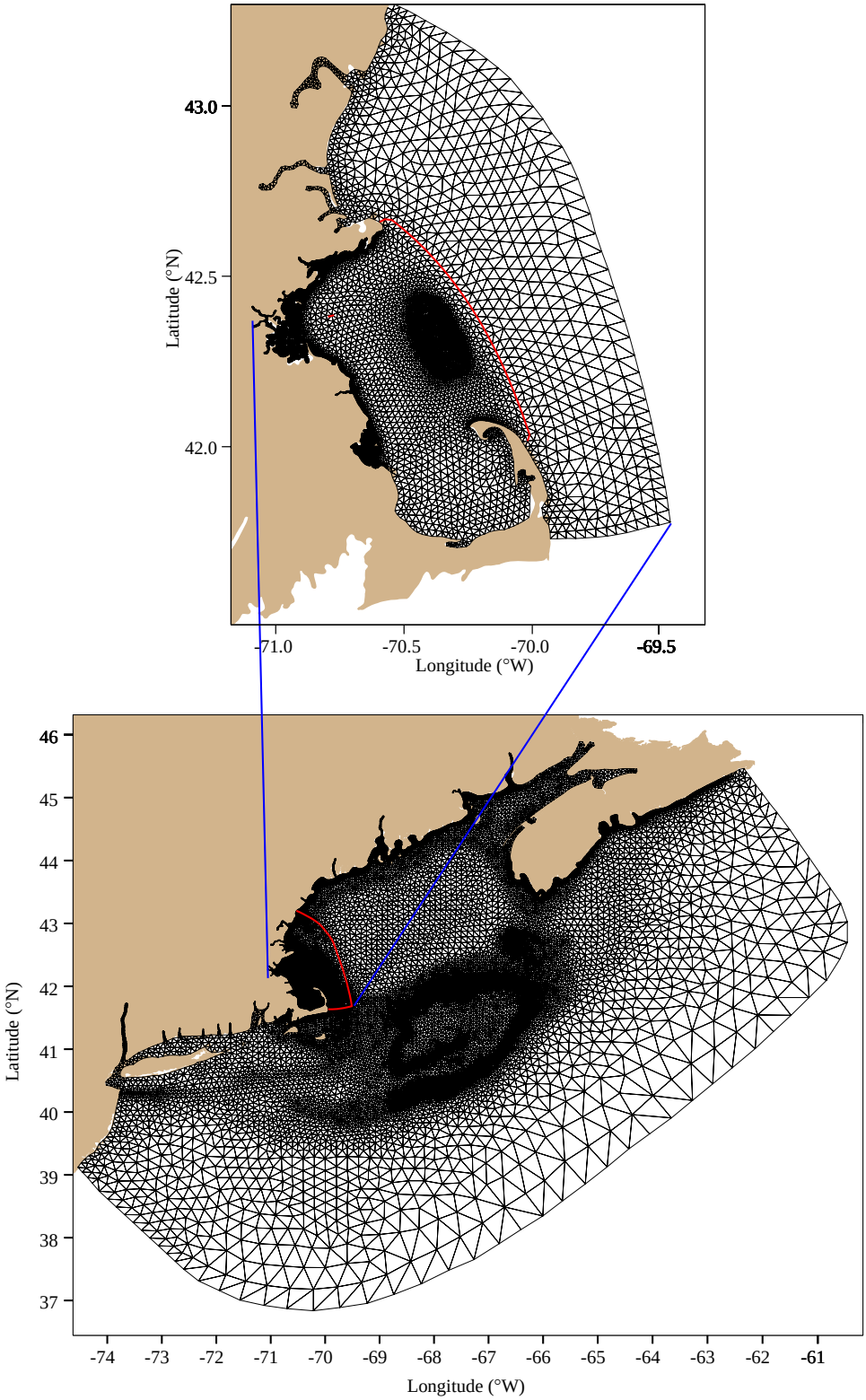

Figure 2.1 Grid for Gulf-of-Maine FVCOM (lower panel); the red line shows the nested domain of Massachusetts Bay FVCOM. The upper panel shows the higher-resolution grid for MB-FVCOM; the red line shows the domain of the water quality model UG-RCA.

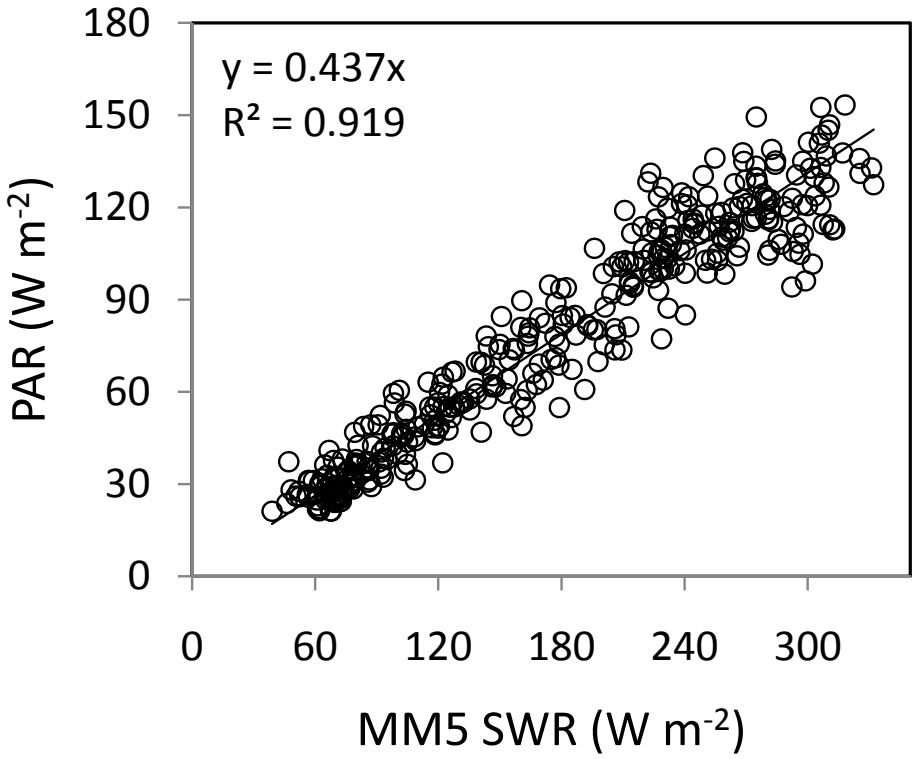

Figure 2.2 Correlation and linear regression between MM5 predicted short wave radiation and SeaWifs-derived PAR at the MWRA outfall.

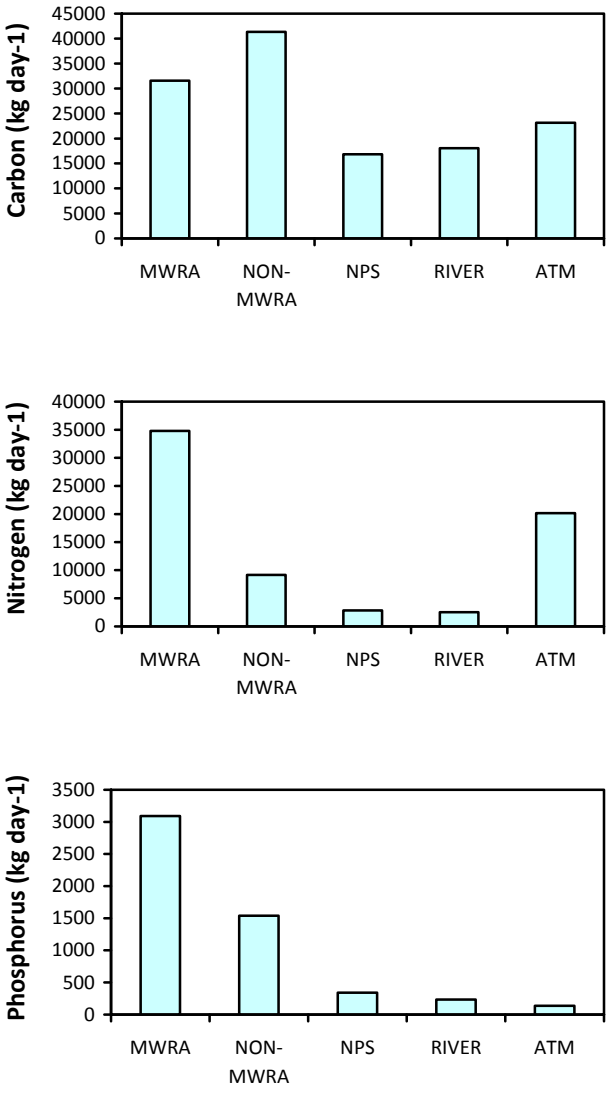

Figure 2.3 Mean daily loads of carbon, nitrogen and phosphorus from different anthropogenic sources. MWRA: MWRA outfall; Non-MWRA: Non MWRA point sources; NPS: Non-point sources; River: River loadings; ATM: Atmospheric input.

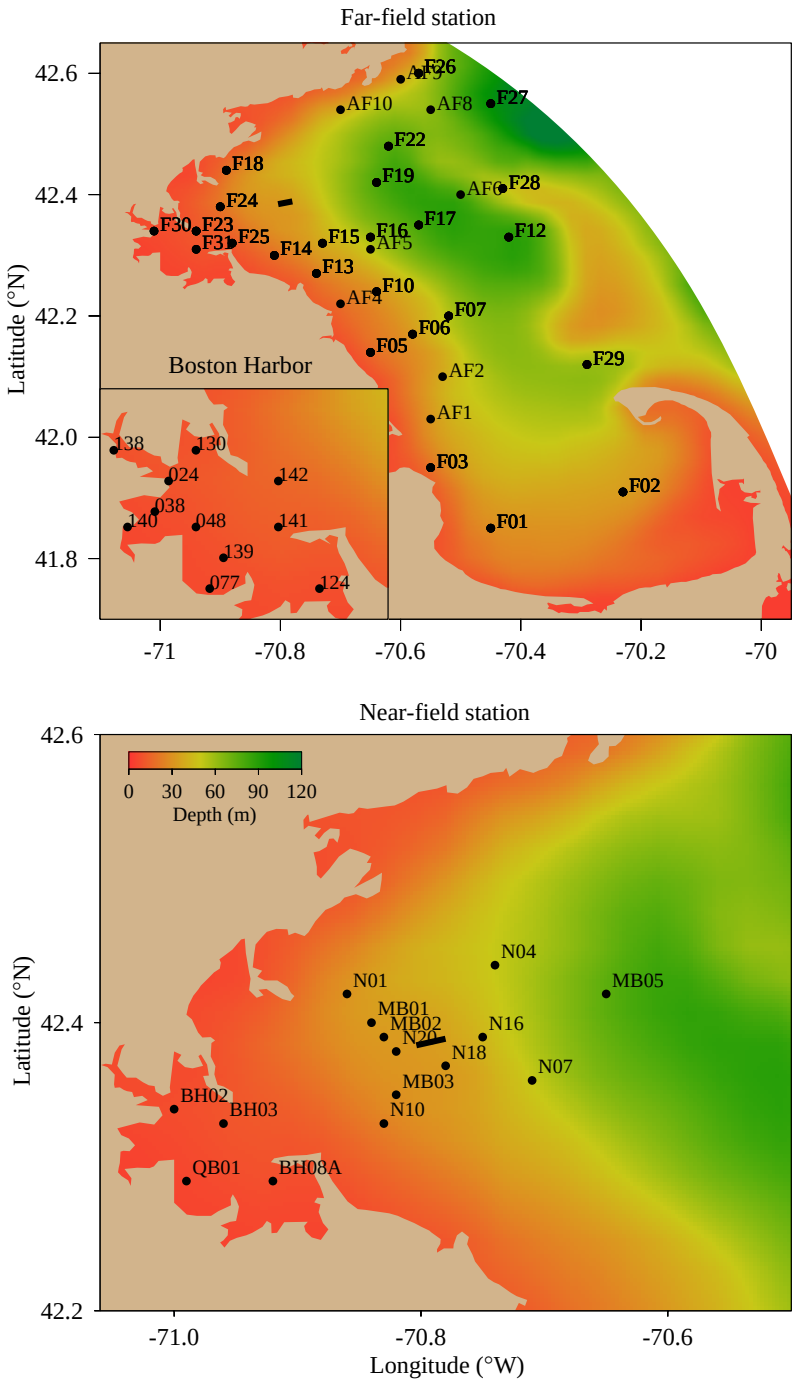

Figure 2.4 Location of farfield (denoted with “F”), *Alexandrium* Rapid Response Study (denoted with “AF”) and harbor stations in the upper panel and nearfield (denoted with “N”), harbor sediment (denoted with “BH” and “QH”) and Massachusetts Bay sediment (denoted with “MB”) stations in the lower panel. The bold line represents the location of the MWRA outfall.

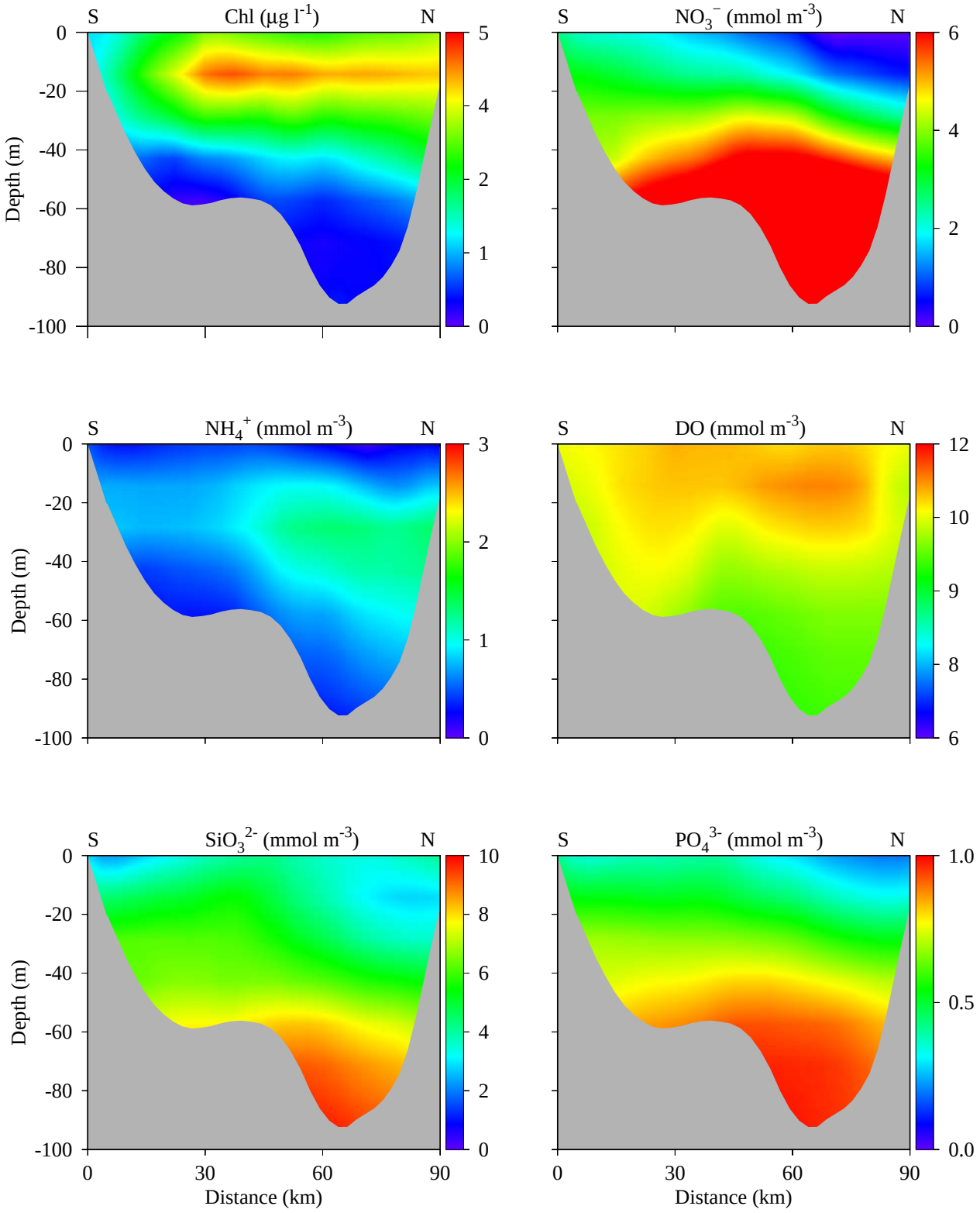

Figure 2.5 Transect of open boundary conditions from Cape Cod (south S) to Cape Ann (north N) of chlorophyll, nutrients and DO on April 15, 2008.

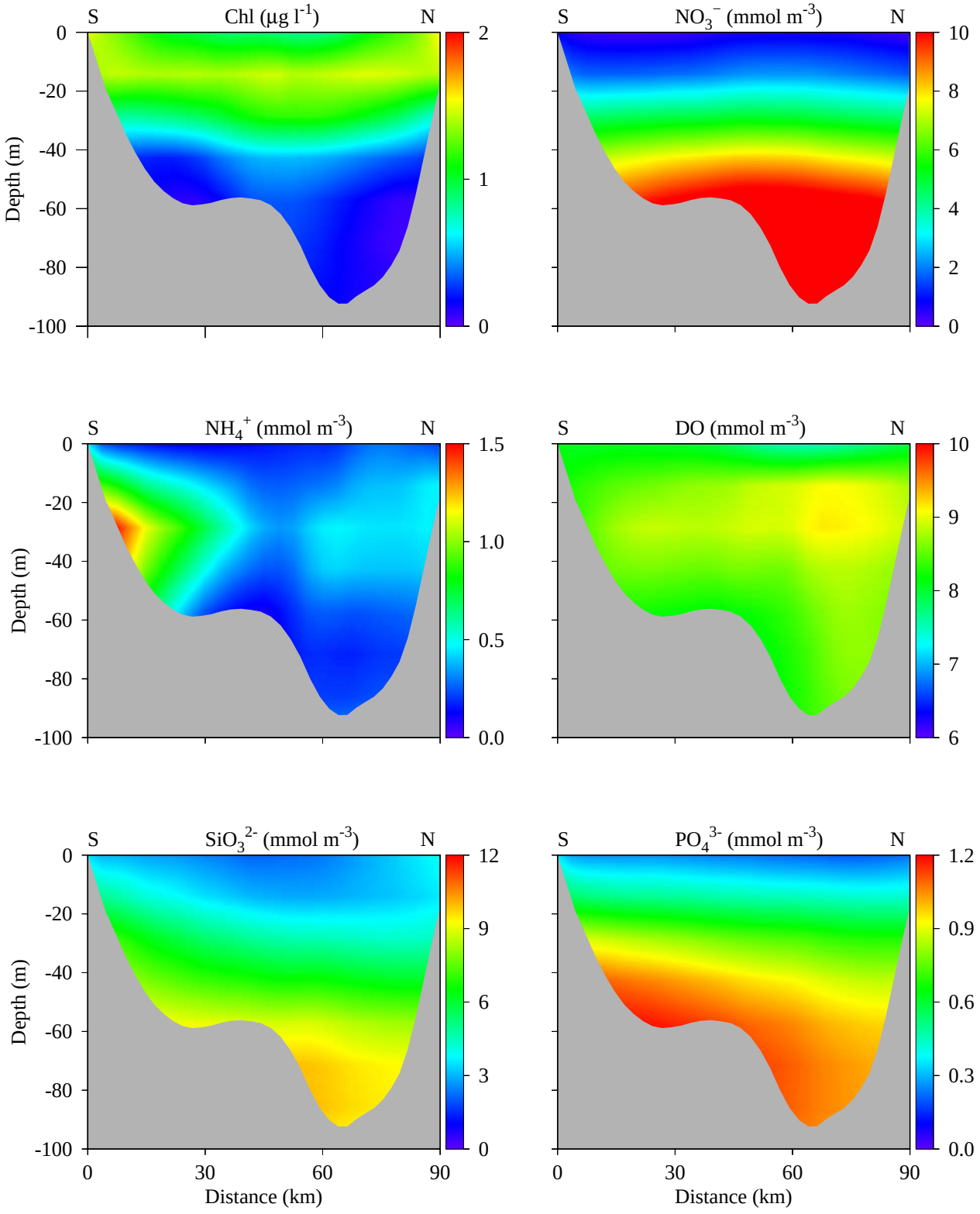

Figure 2.6 Transect of open boundary conditions from Cape Cod (south S) to Cape Ann (north N) of chlorophyll, nutrients and DO on August 15, 2008.

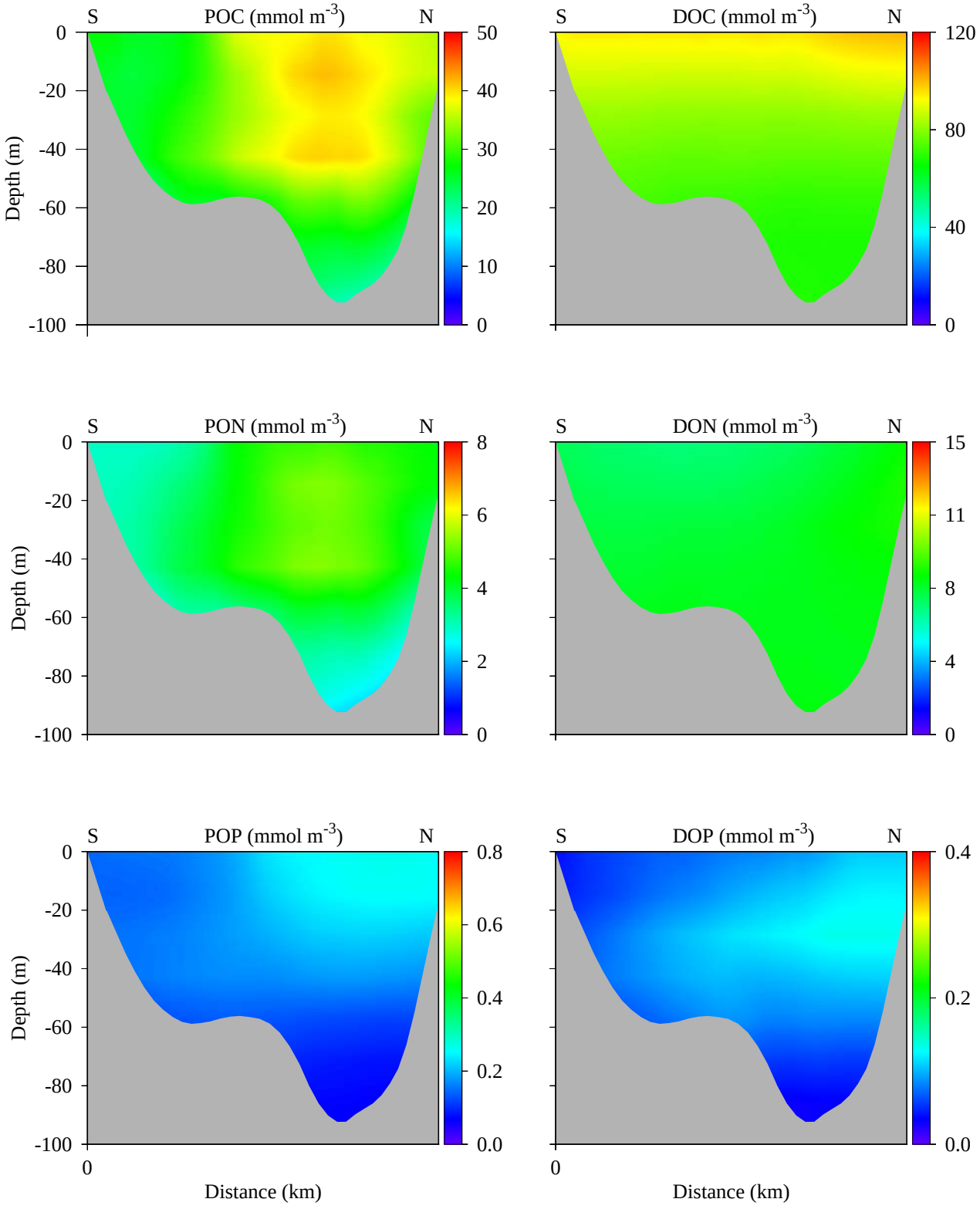

Figure 2.7 Transect of open boundary conditions from Cape Cod (south S) to Cape Ann (north N) of organic nutrient elements on April 15, 2008.

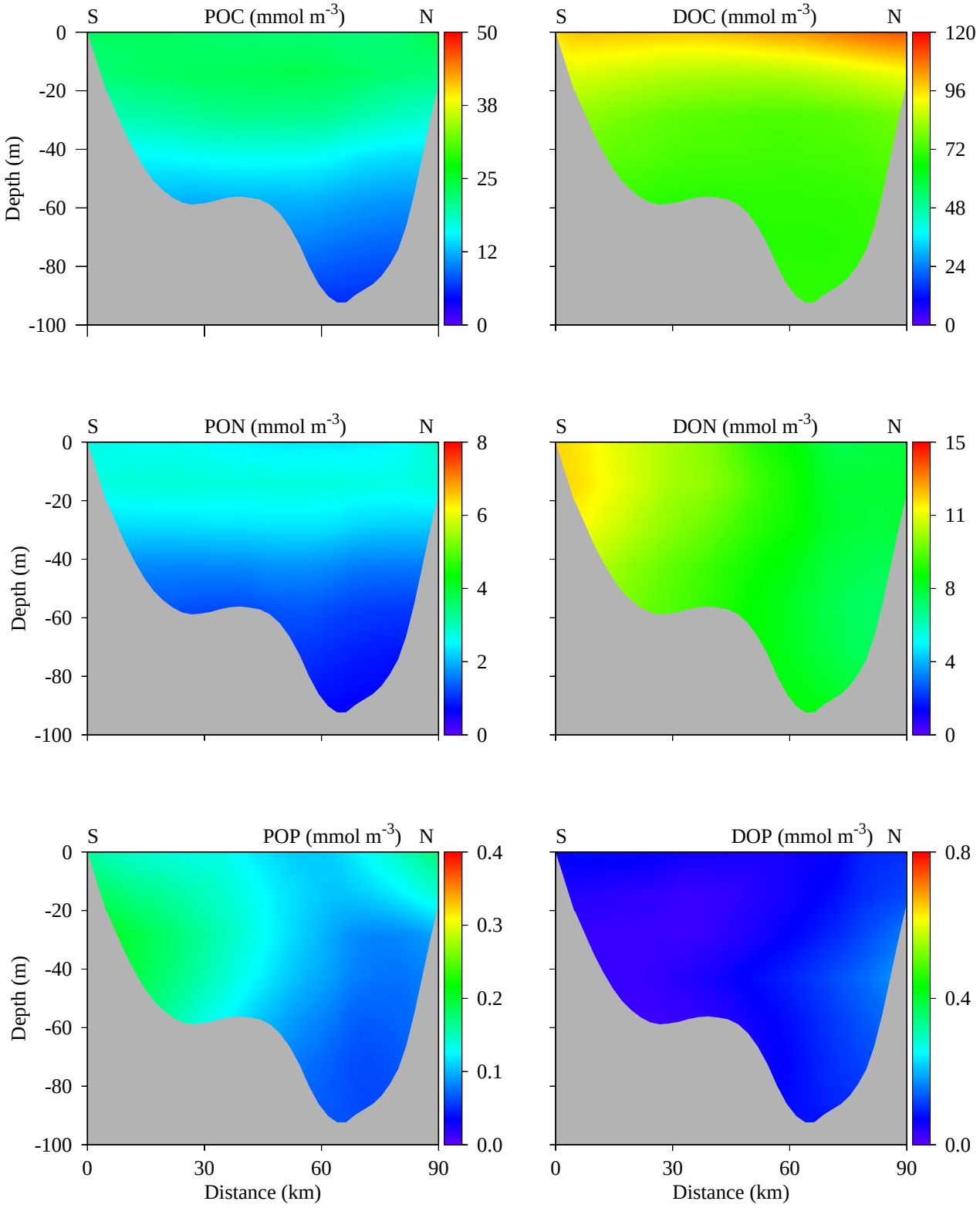

Figure 2.8 Transect of open boundary conditions from Cape Cod (south S) to Cape Ann (north N) of organic nutrient elements on August 15, 2008.

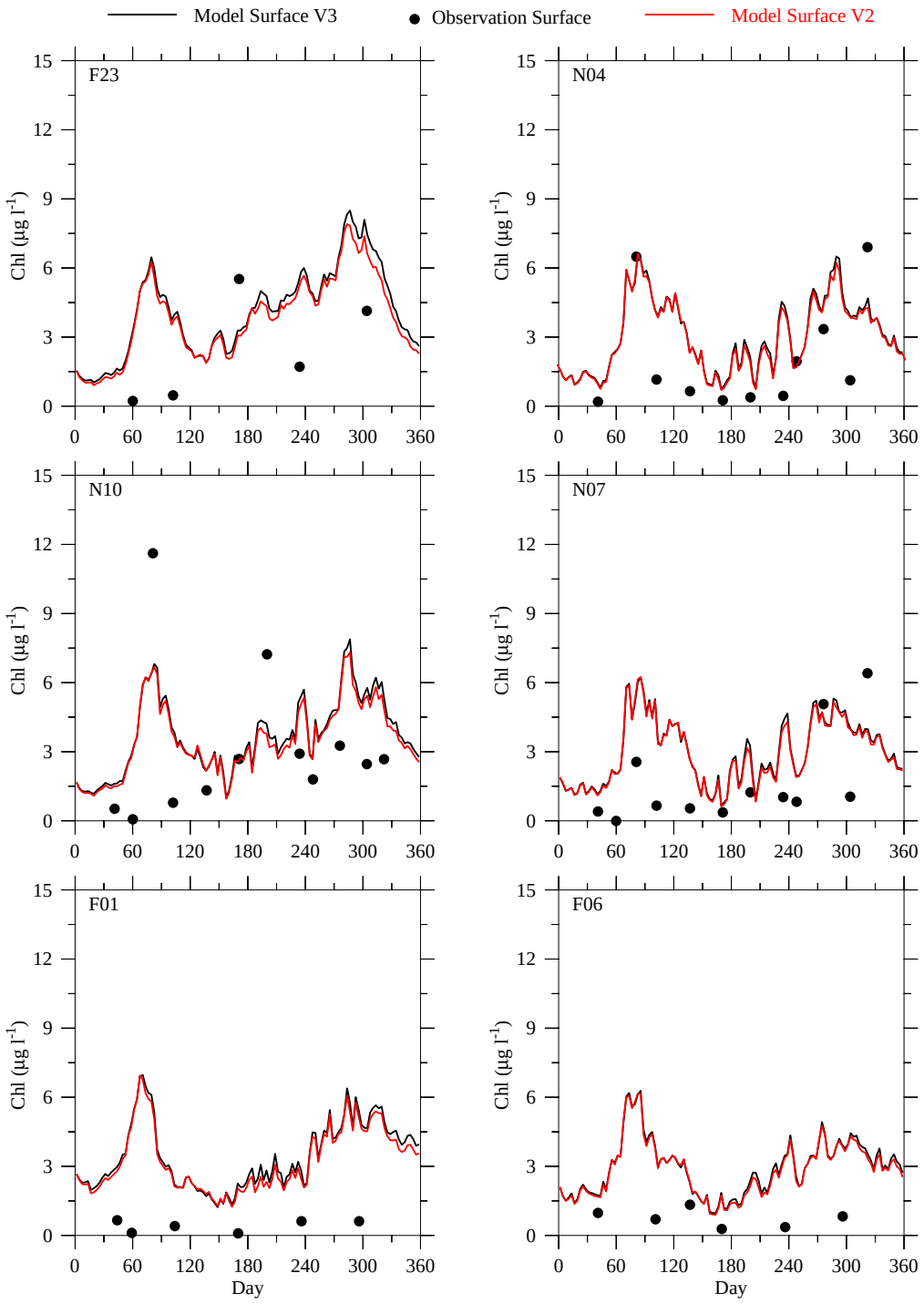

Figure 3.1 Comparison of chlorophyll in surface waters between RCA version 3 (black lines) and version 2 (red lines) at selected Massachusetts Bay monitoring stations in 2006. Dots are field measurements.

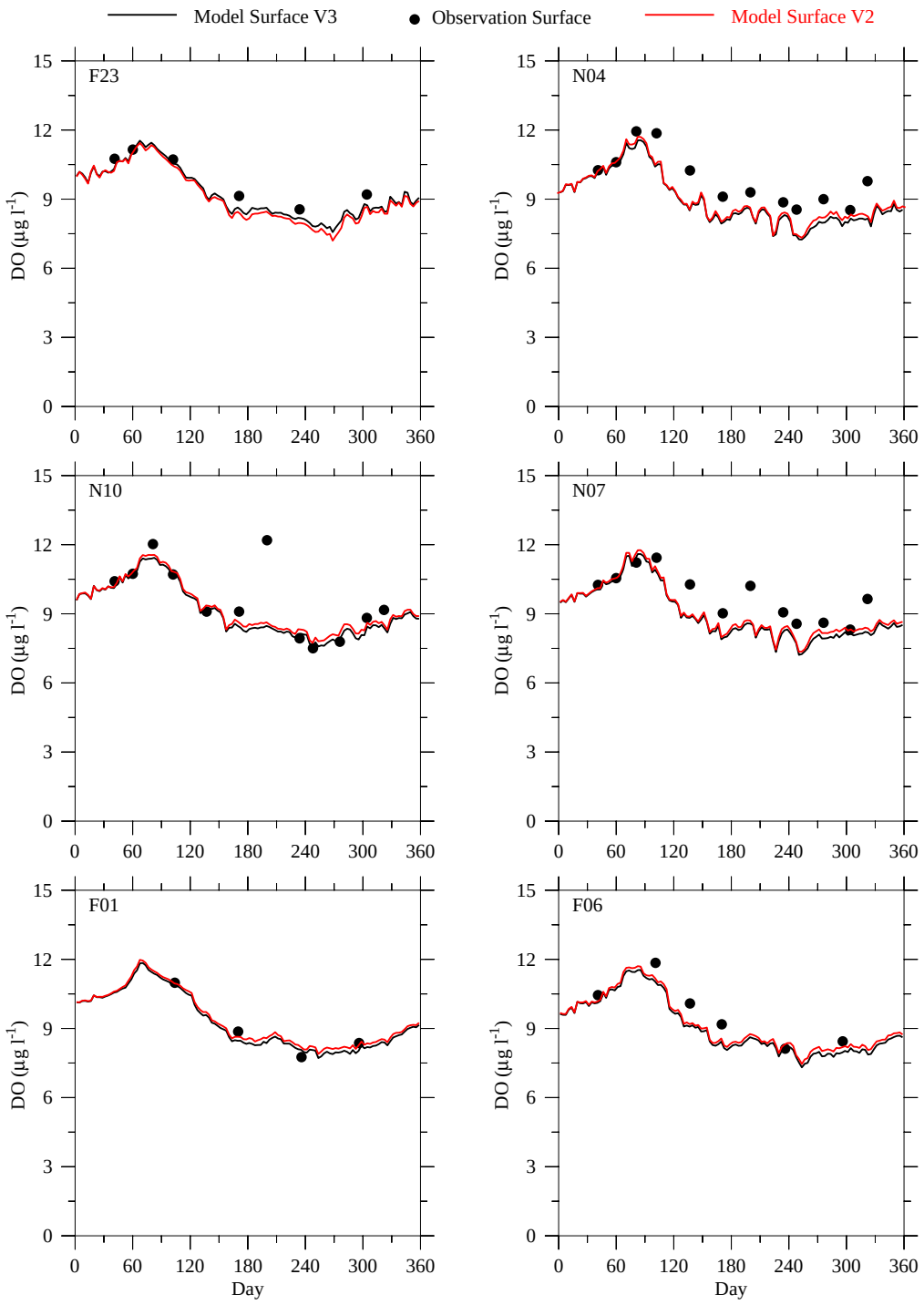

Figure 3.2 Comparison of surface dissolved oxygen between RCA version 3 (black lines) and version 2 (red lines) at selected Massachusetts Bay monitoring stations in 2006. Dots are field measurements.

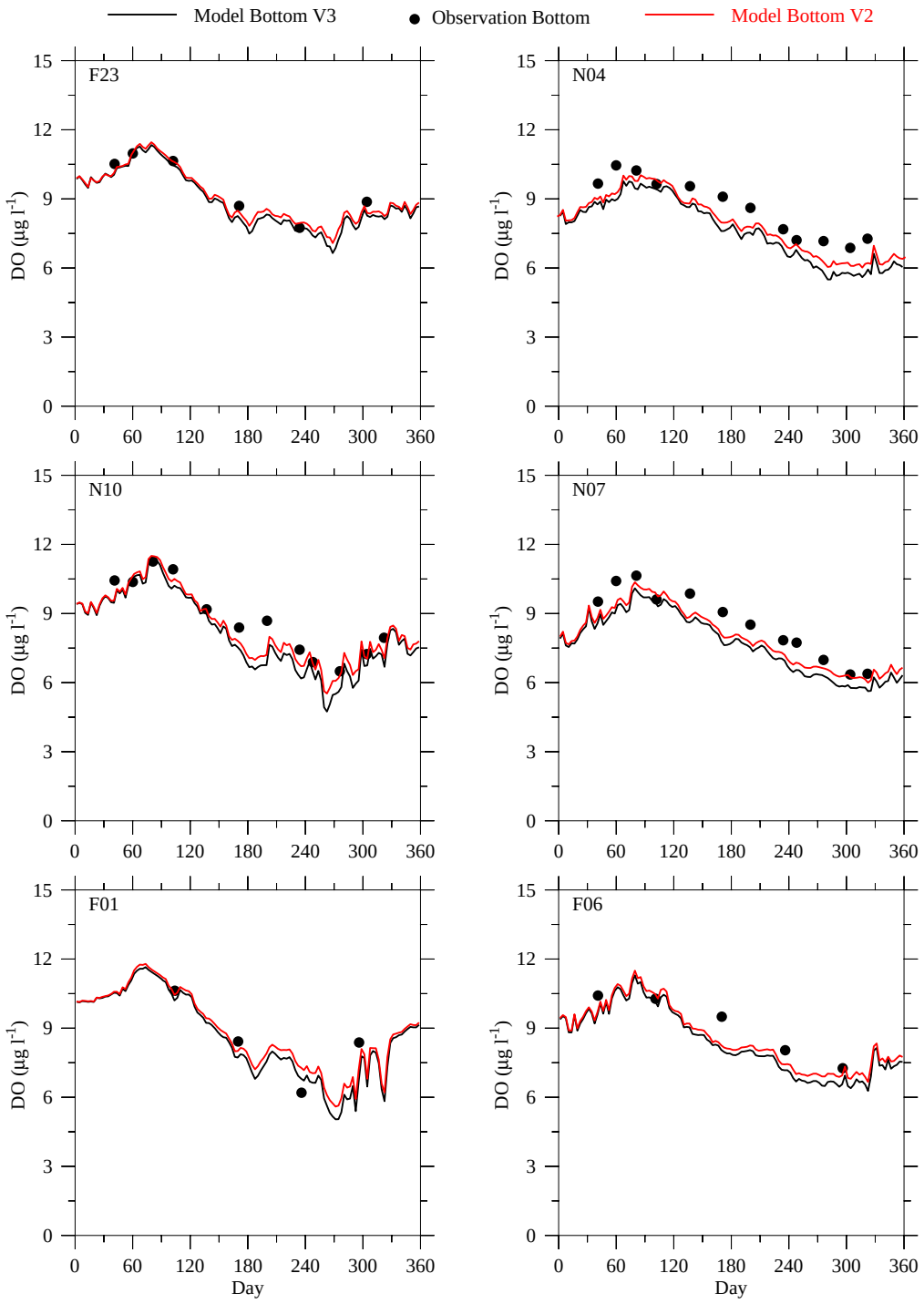

Figure 3.3 Comparison of bottom dissolved oxygen between RCA version 3 (black lines) and version 2 (red lines) at selected Massachusetts Bay monitoring stations in 2006. Dots are field measurements.

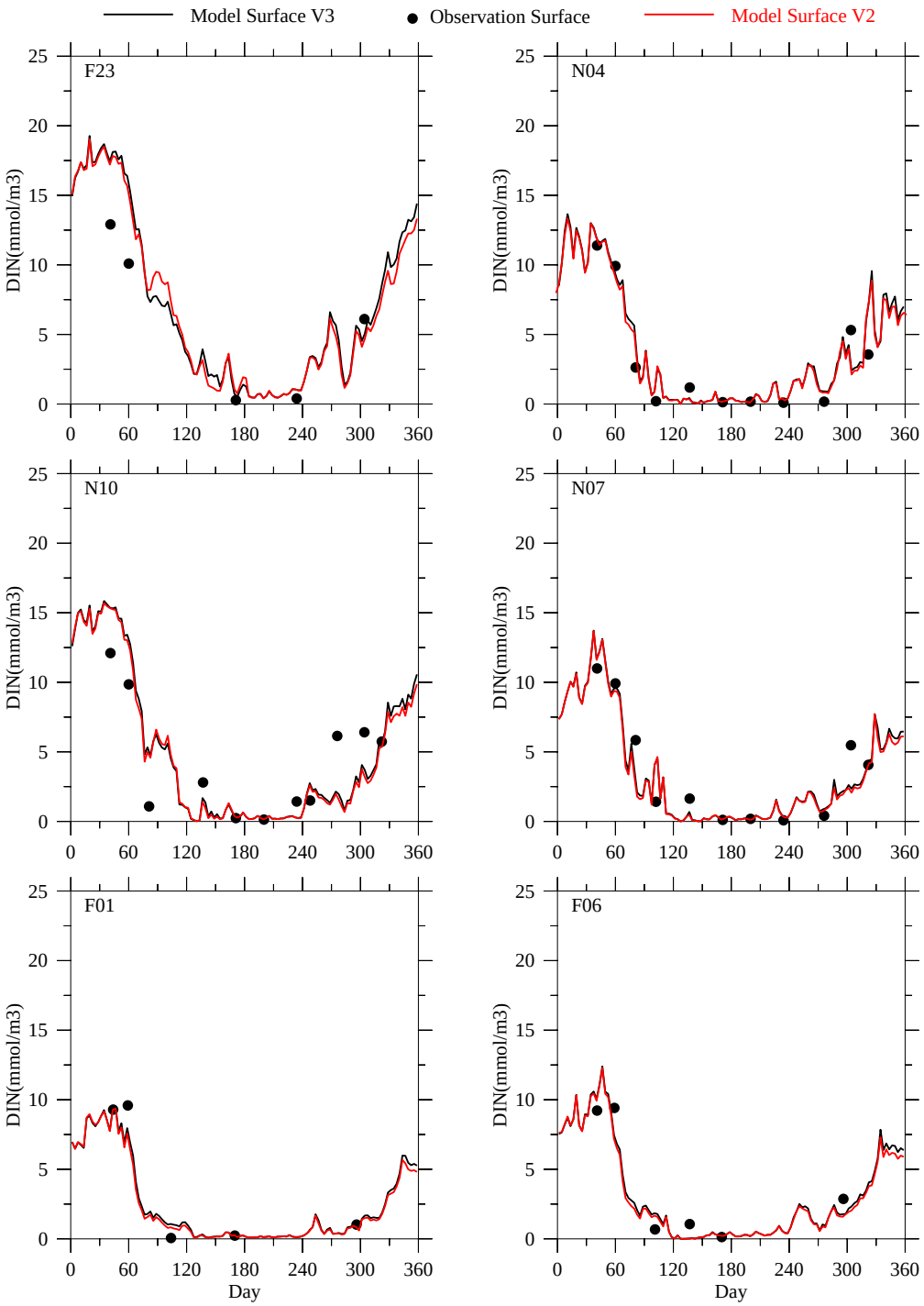

Figure 3.4 Comparison of surface dissolved inorganic nitrogen between RCA version 3 (black lines) and version 2 (red lines) at selected Massachusetts Bay monitoring stations in 2006. Dots are field measurements.

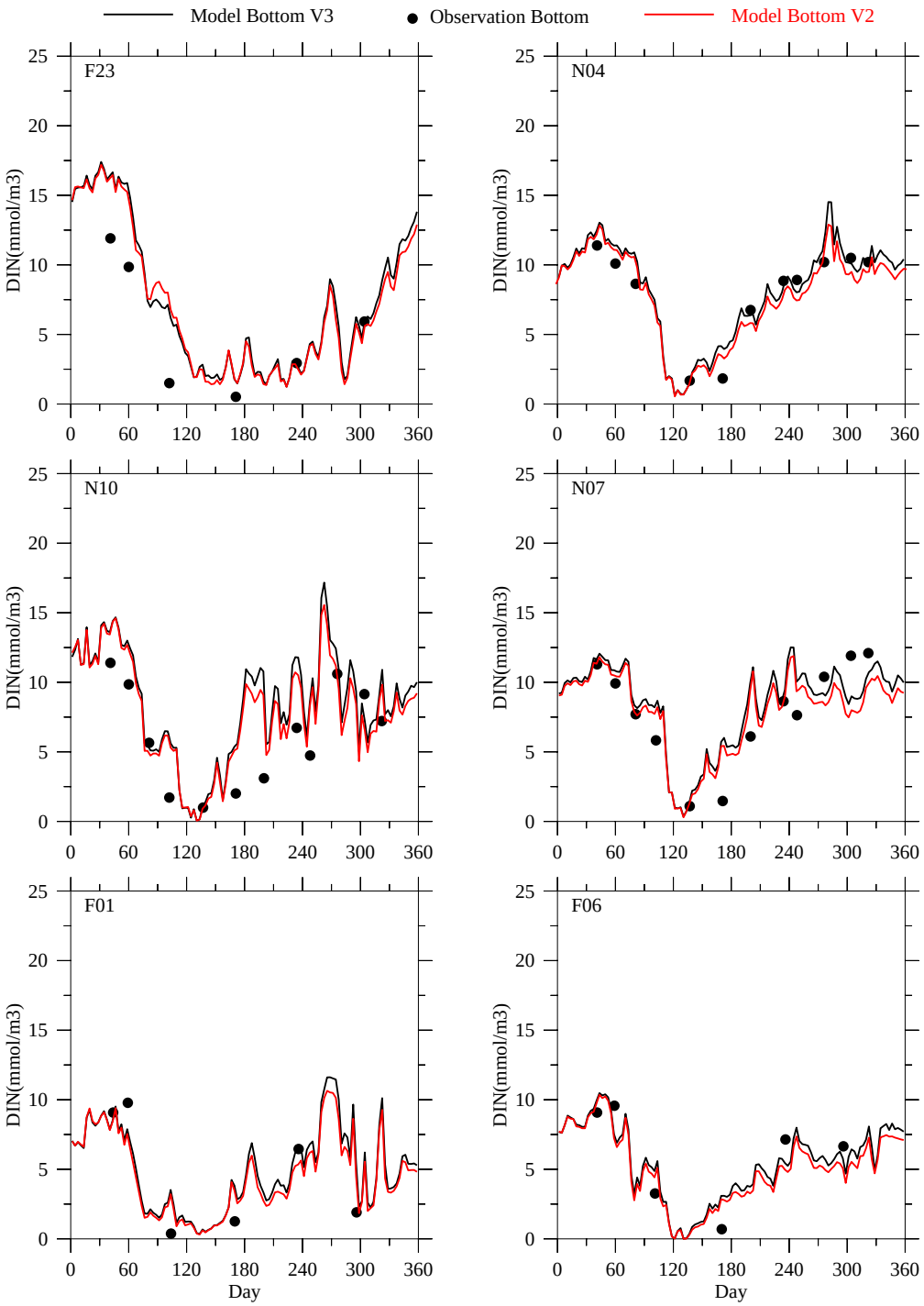

Figure 3.5 Comparison of bottom dissolved inorganic nitrogen between RCA version 3 (black lines) and version 2 (red lines) at selected Massachusetts Bay monitoring stations in 2006. Dots are field measurements.

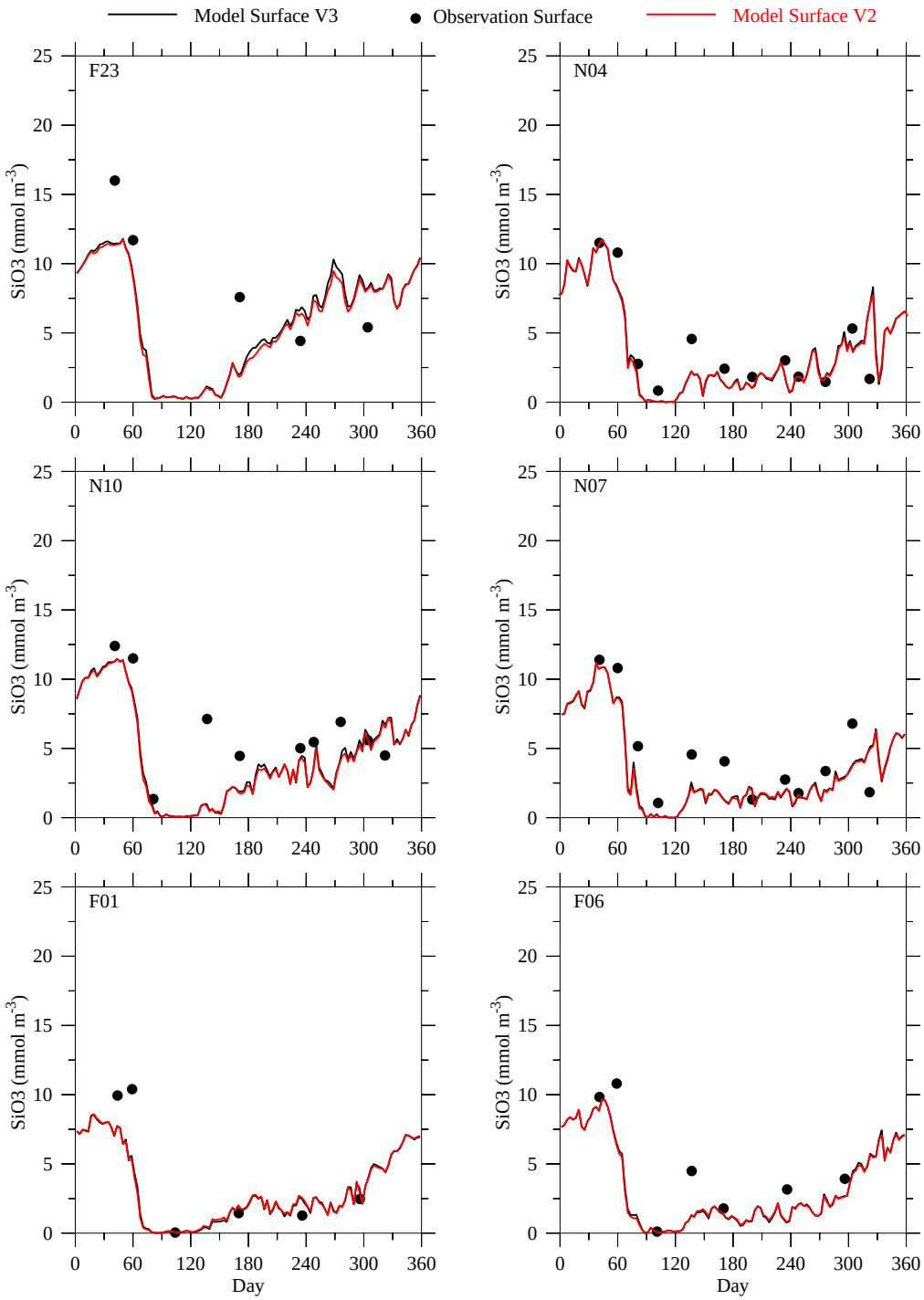

Figure 3.6 Comparison of surface silicate between RCA version 3 (black lines) and version 2 (red lines) at selected Massachusetts Bay monitoring stations in 2006. Dots are field measurements.

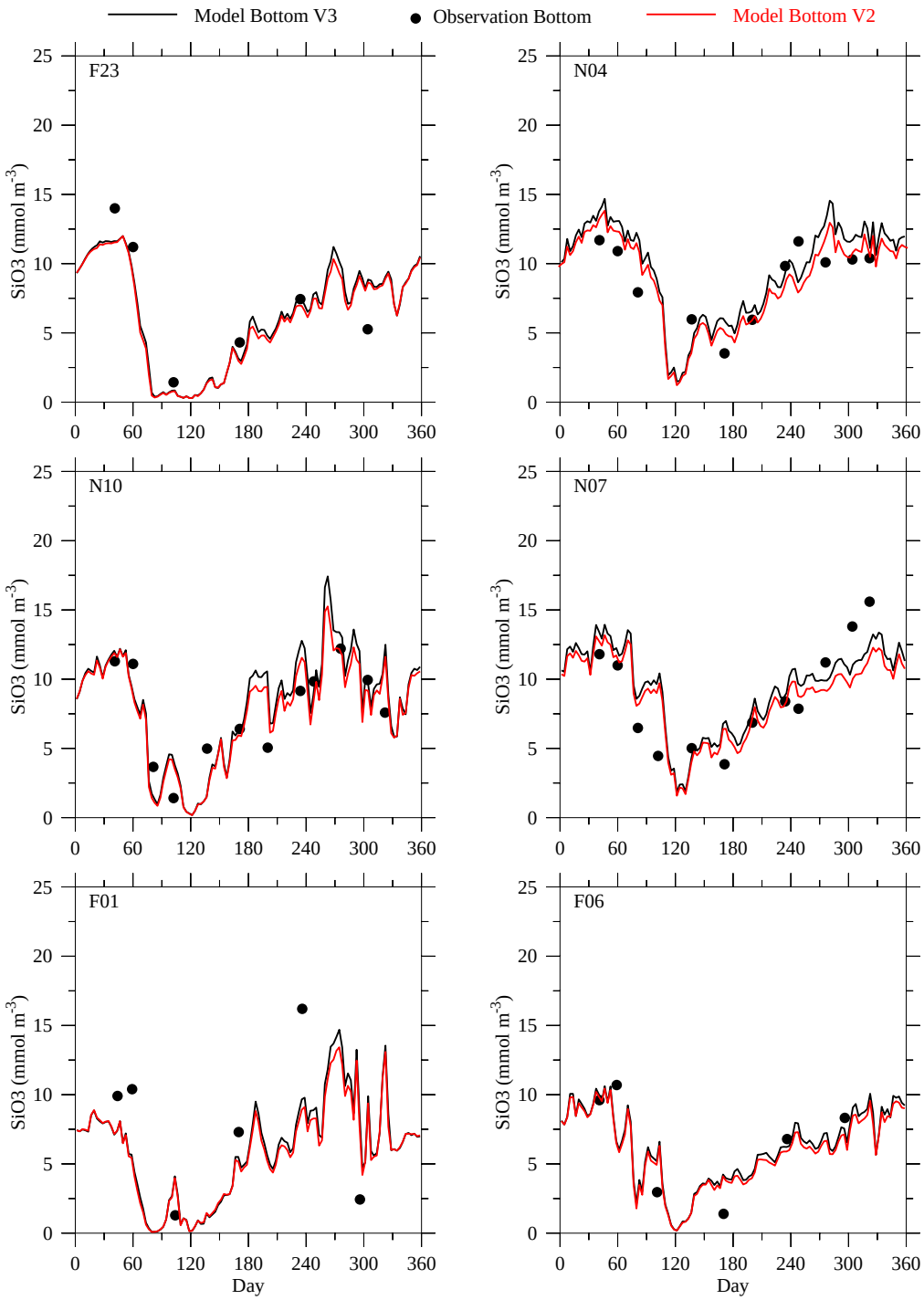

Figure 3.7 Comparison of bottom silicate between RCA version 3 (black lines) and version 2 (red lines) at selected Massachusetts Bay monitoring stations in 2006. Dots are field measurements.

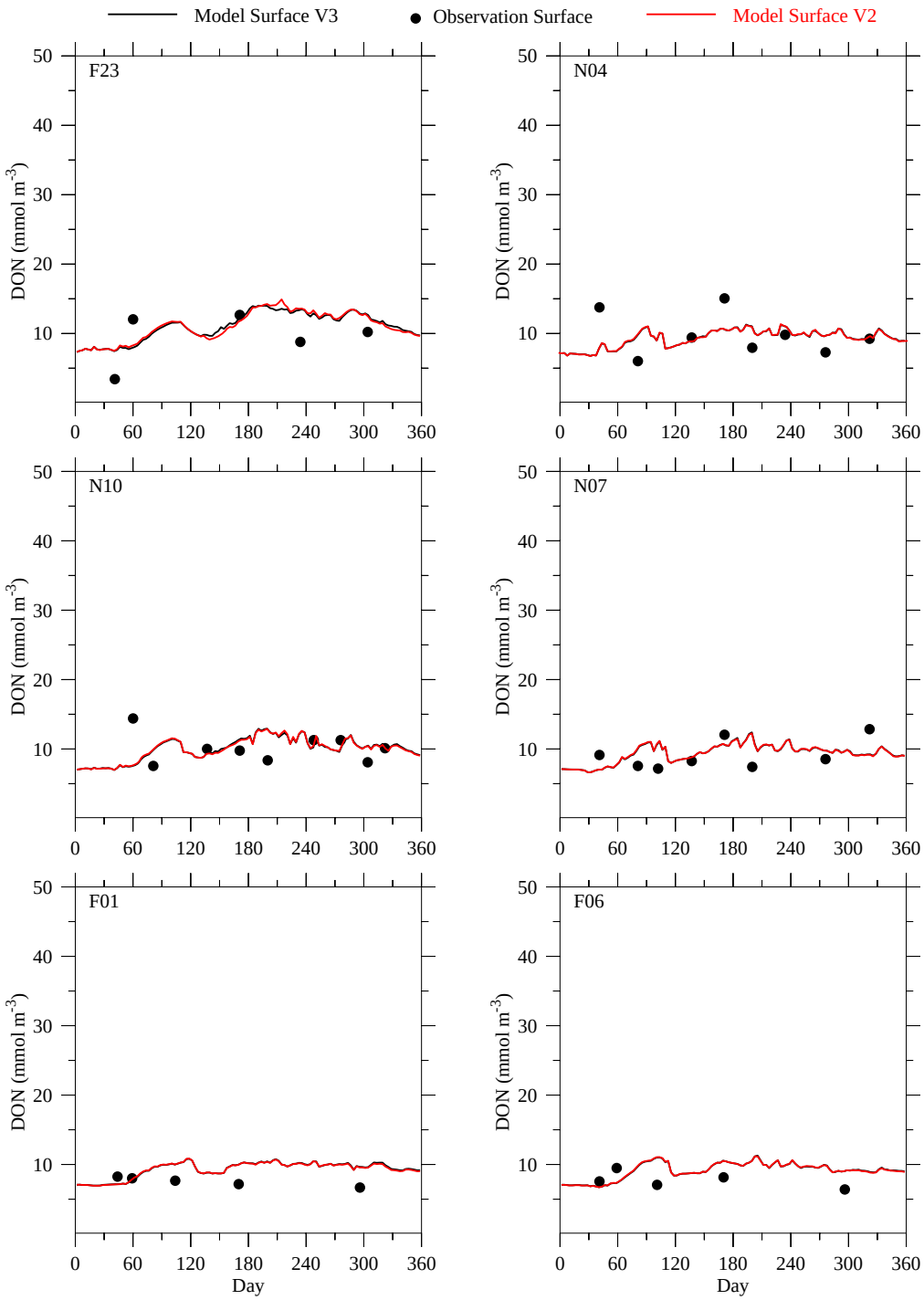

Figure 3.8 Comparison of surface dissolved organic nitrogen between RCA version 3 (black lines) and version 2 (red lines) at selected Massachusetts Bay monitoring stations in 2006. Dots are field measurements.

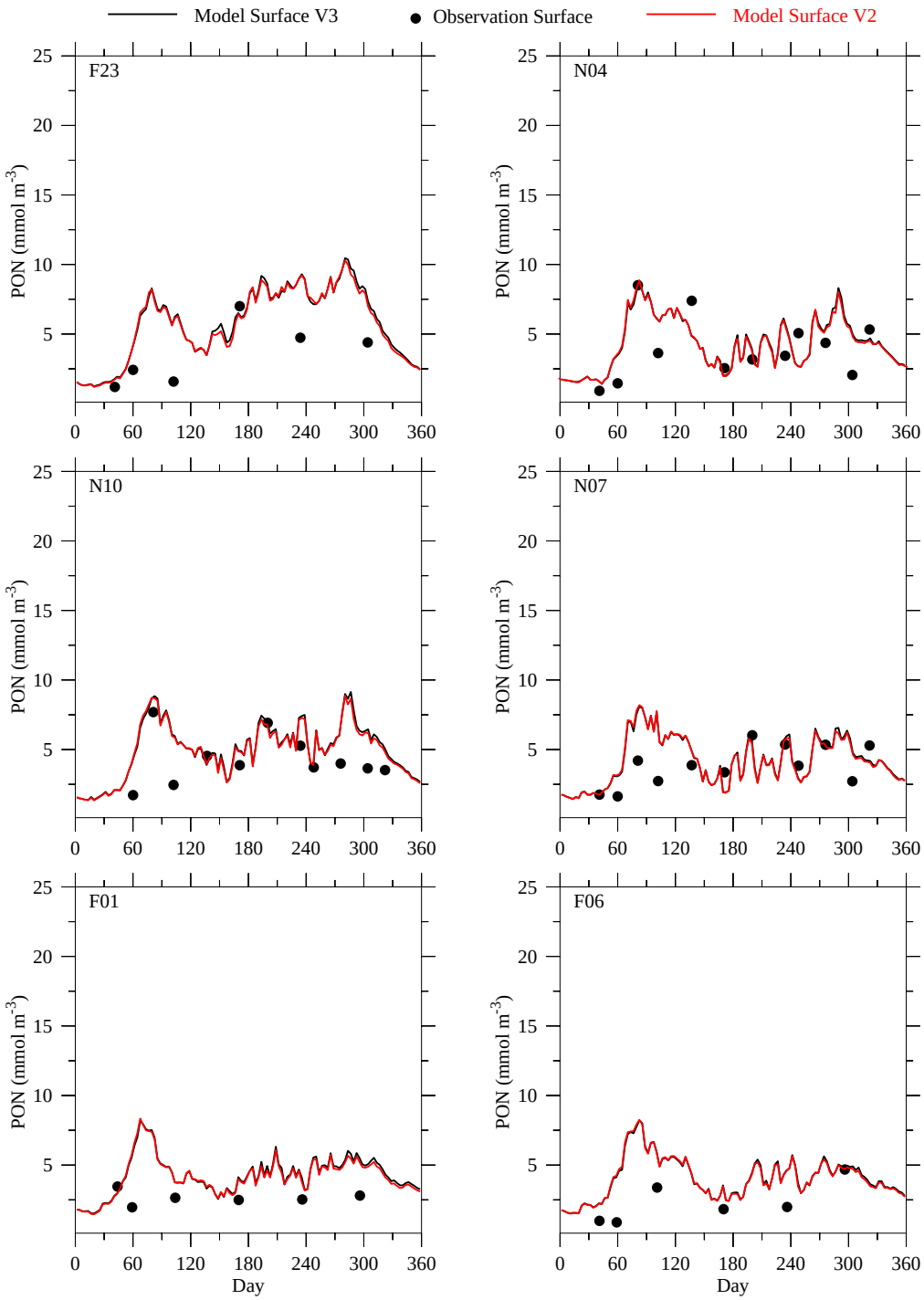

Figure 3.9 Comparison of surface particulate organic nitrogen between RCA version 3 (black lines) and version 2 (red lines) at selected Massachusetts Bay monitoring stations in 2006. Dots are field measurements.

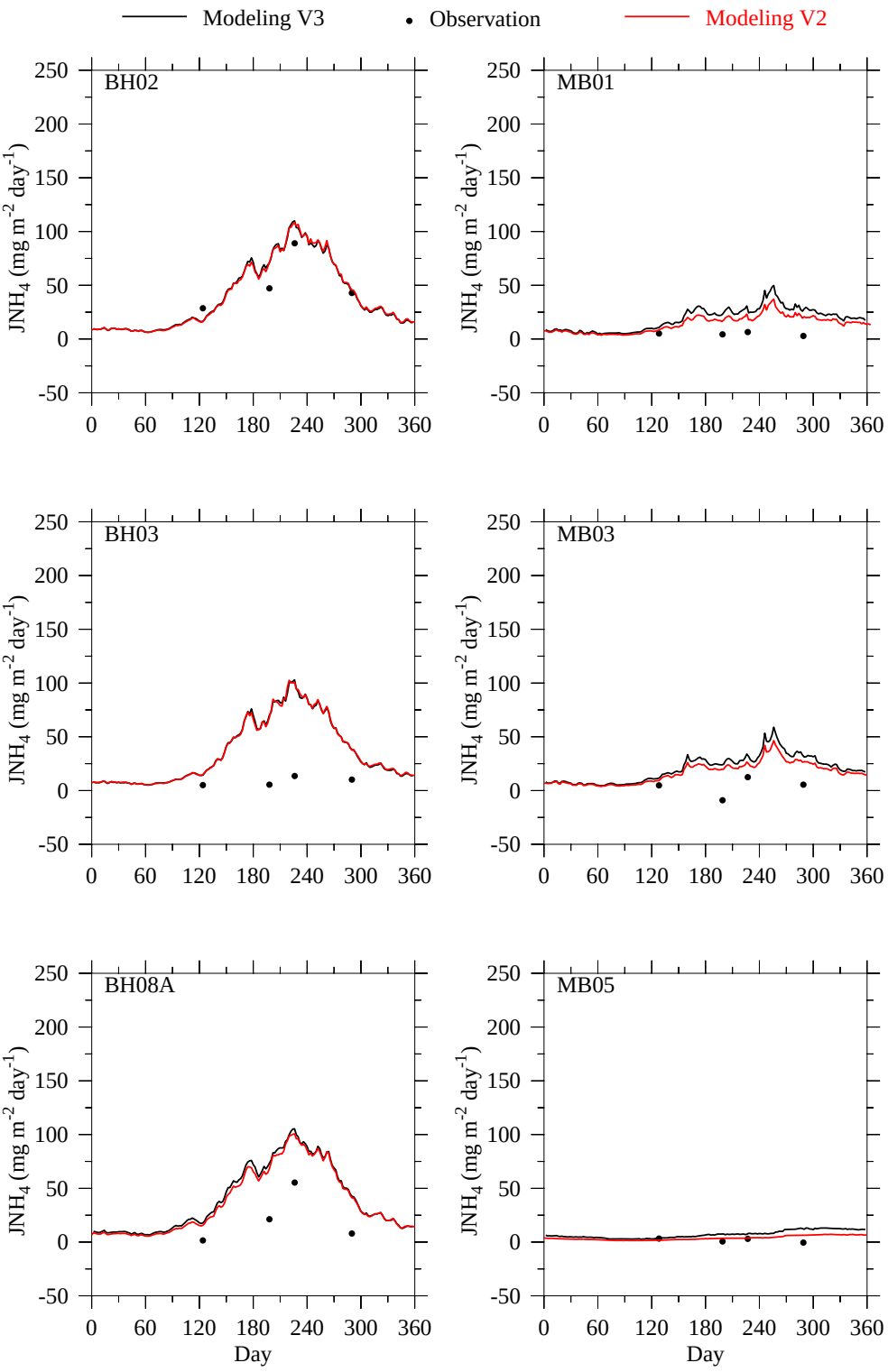

Figure 3.10 Comparison of ammonium flux at the sediment-water interface between RCA version 3 (black lines) and version 2 (red lines) at selected Massachusetts Bay monitoring stations in 2006. Dots are field measurements.

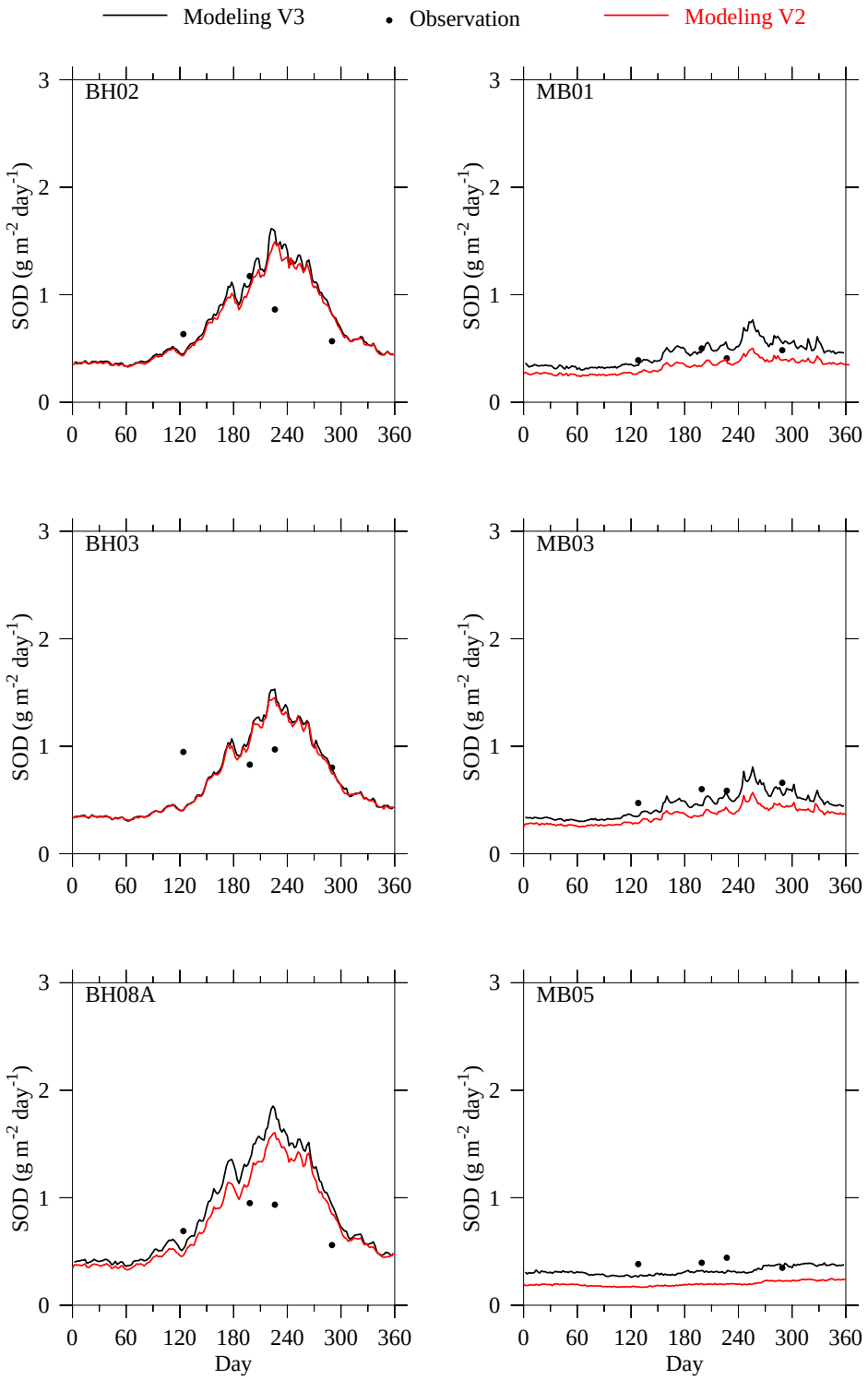

Figure 3.11 Comparison of dissolved oxygen demand at the sediment-water interface between RCA version 3 (black lines) and version 2 (red lines) at selected Massachusetts Bay monitoring stations in 2006. Dots are field measurements.

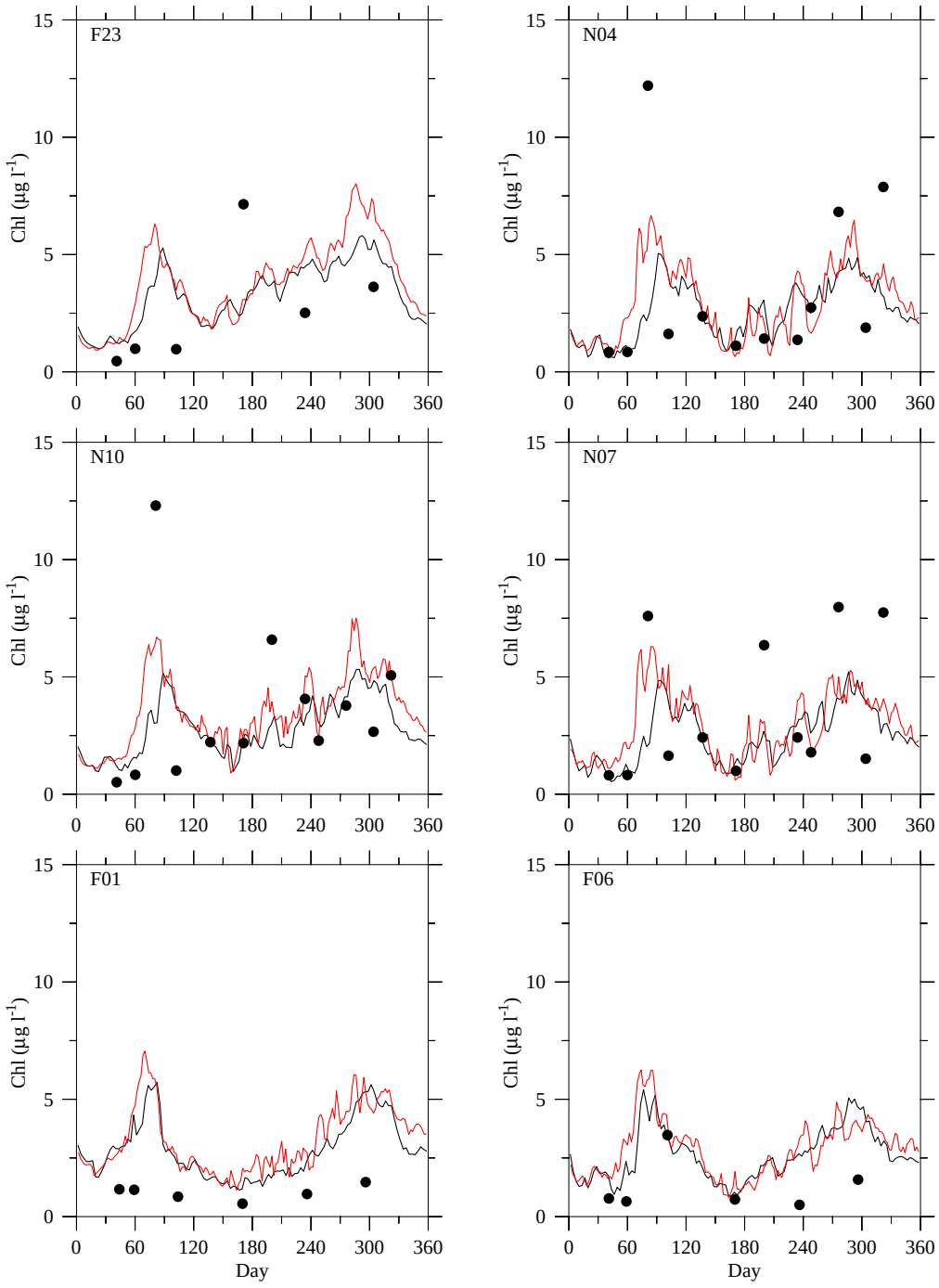

Figure 3.12 Comparison of chlorophyll in surface waters between UG-RCA (black lines) and RCA-v2 (red lines) at selected Massachusetts Bay monitoring stations in 2006. Dots are field measurements.

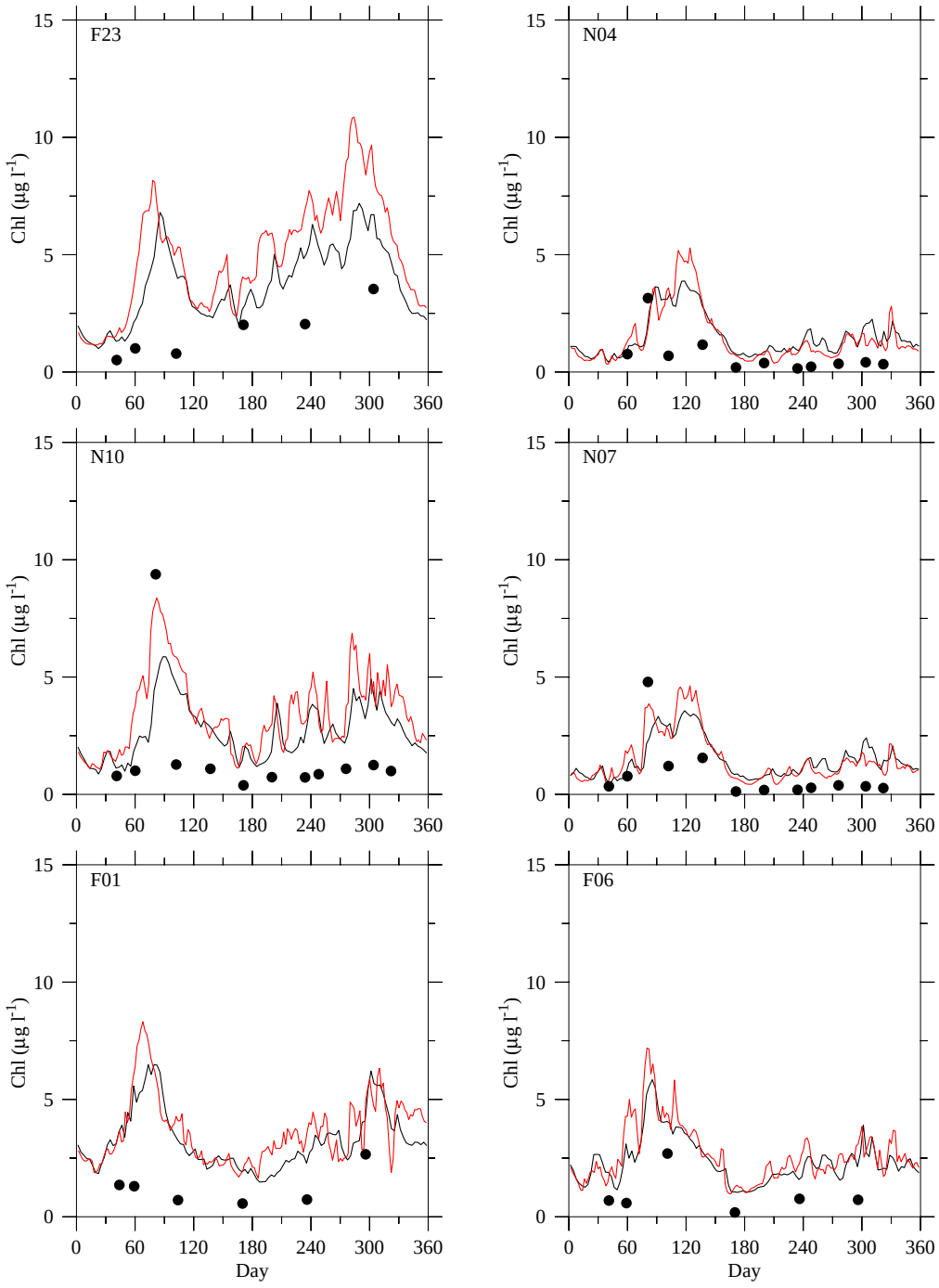

Figure 3.13 Comparison of chlorophyll in bottom waters between UG-RCA (black lines) and RCA-v2 (red lines) at selected Massachusetts Bay monitoring stations in 2006. Dots are field measurements.

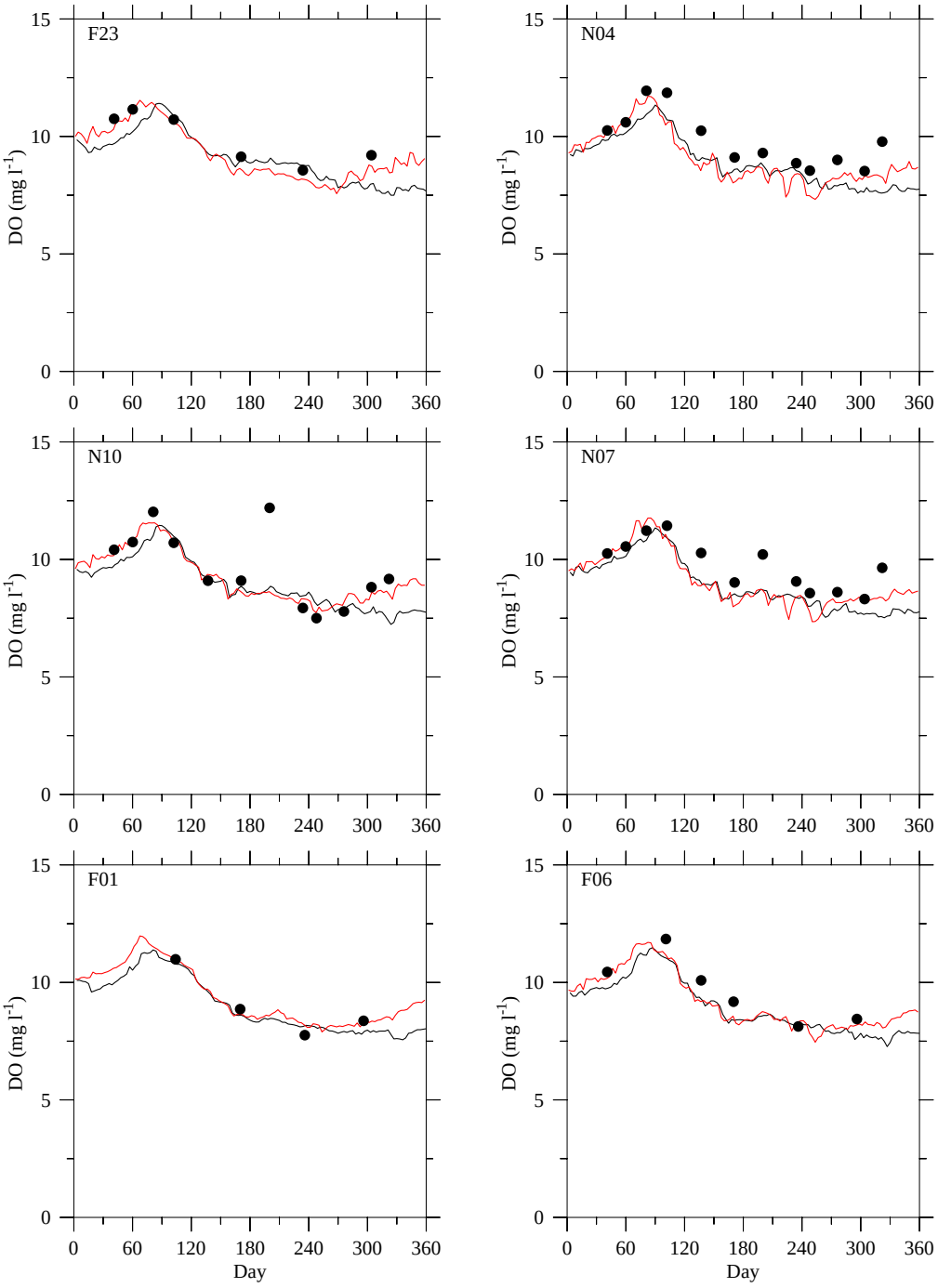

Figure 3.14 Comparison of surface dissolved oxygen between UG-RCA (black lines) and RCA-v2 (red lines) at selected Massachusetts Bay monitoring stations in 2006. Dots are field measurements.

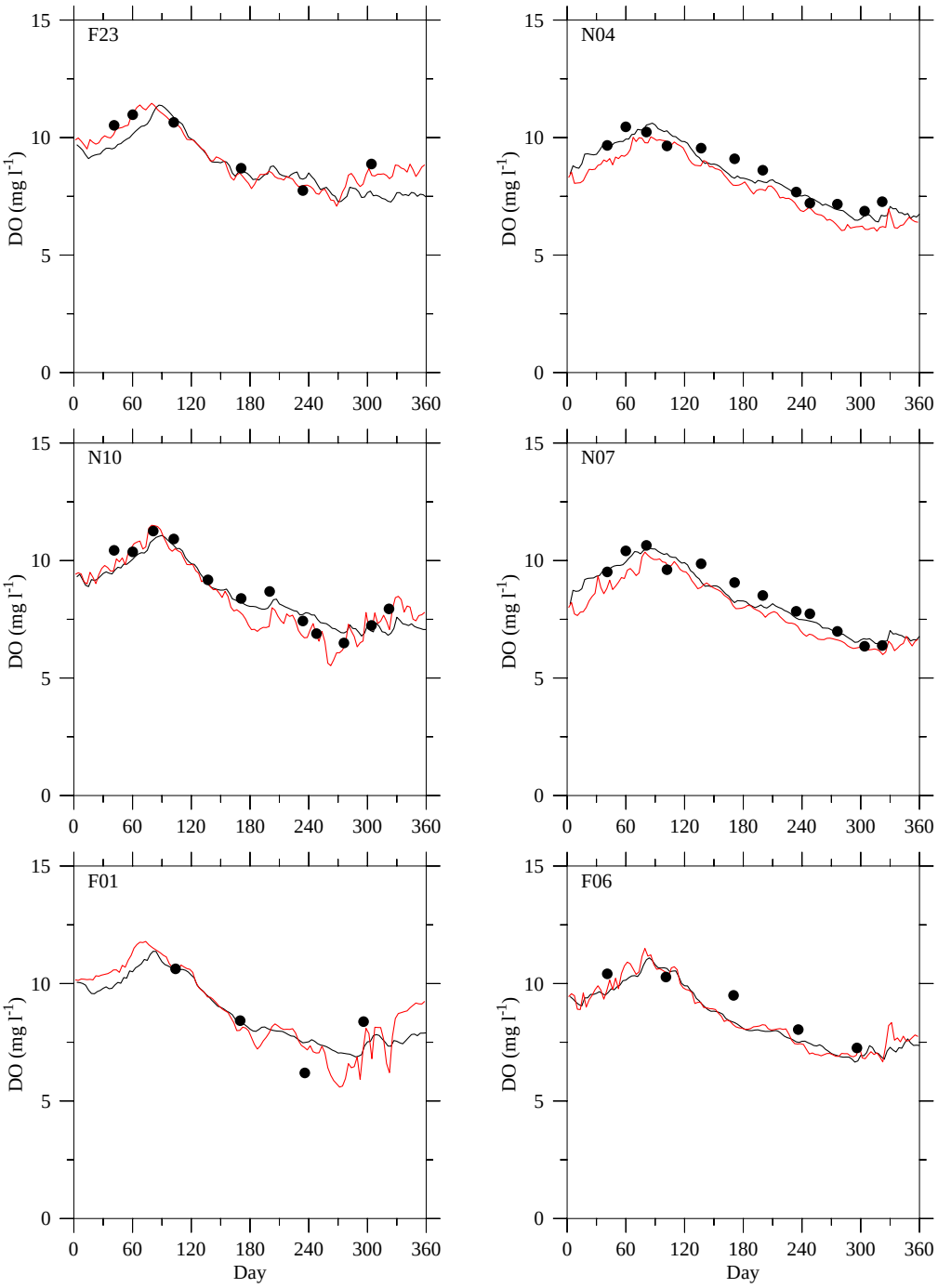

Figure 3.15 Comparison of bottom dissolved oxygen between UG-RCA (black lines) and RCA-v2 (red lines) at selected Massachusetts Bay monitoring stations in 2006. Dots are field measurements.

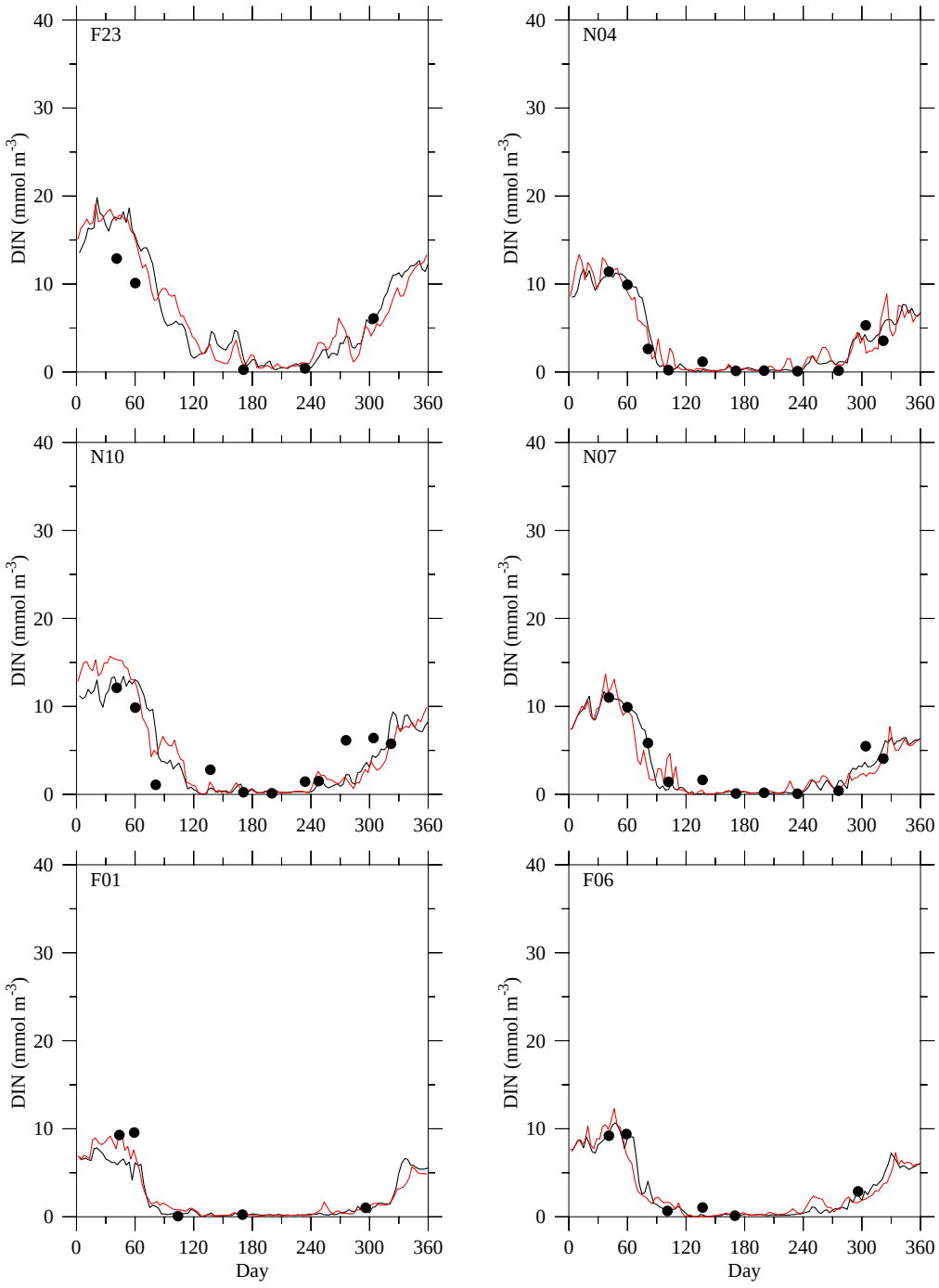

Figure 3.16 Comparison of surface dissolved inorganic nitrogen between UG-RCA (black lines) and RCA-v2 (red lines) at selected Massachusetts Bay monitoring stations in 2006. Dots are field measurements.

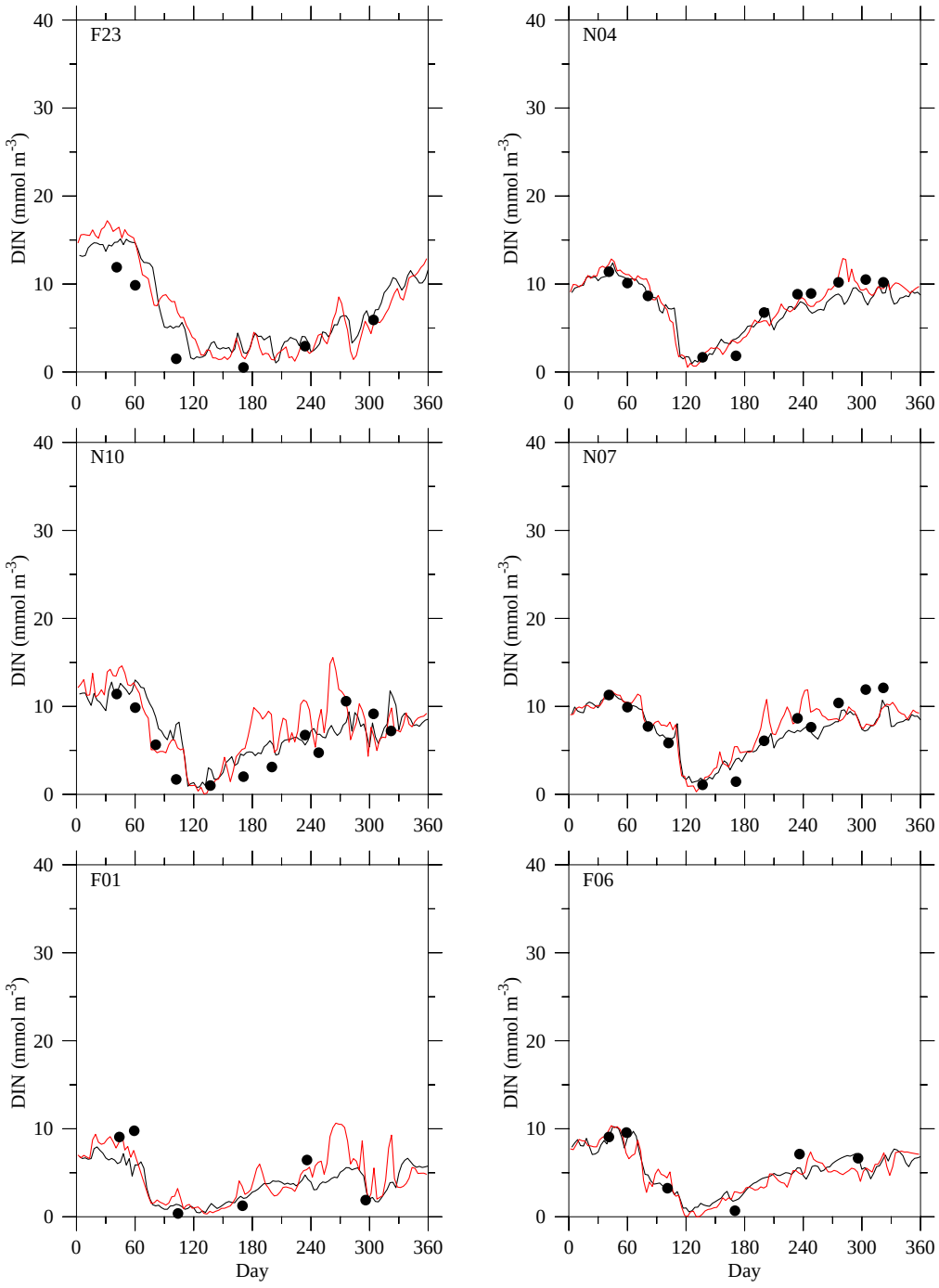

Figure 3.17 Comparison of bottom dissolved inorganic nitrogen between UG-RCA (black lines) and RCA-v2 (red lines) (red lines) at selected Massachusetts Bay monitoring stations in 2006. Dots are field measurements.

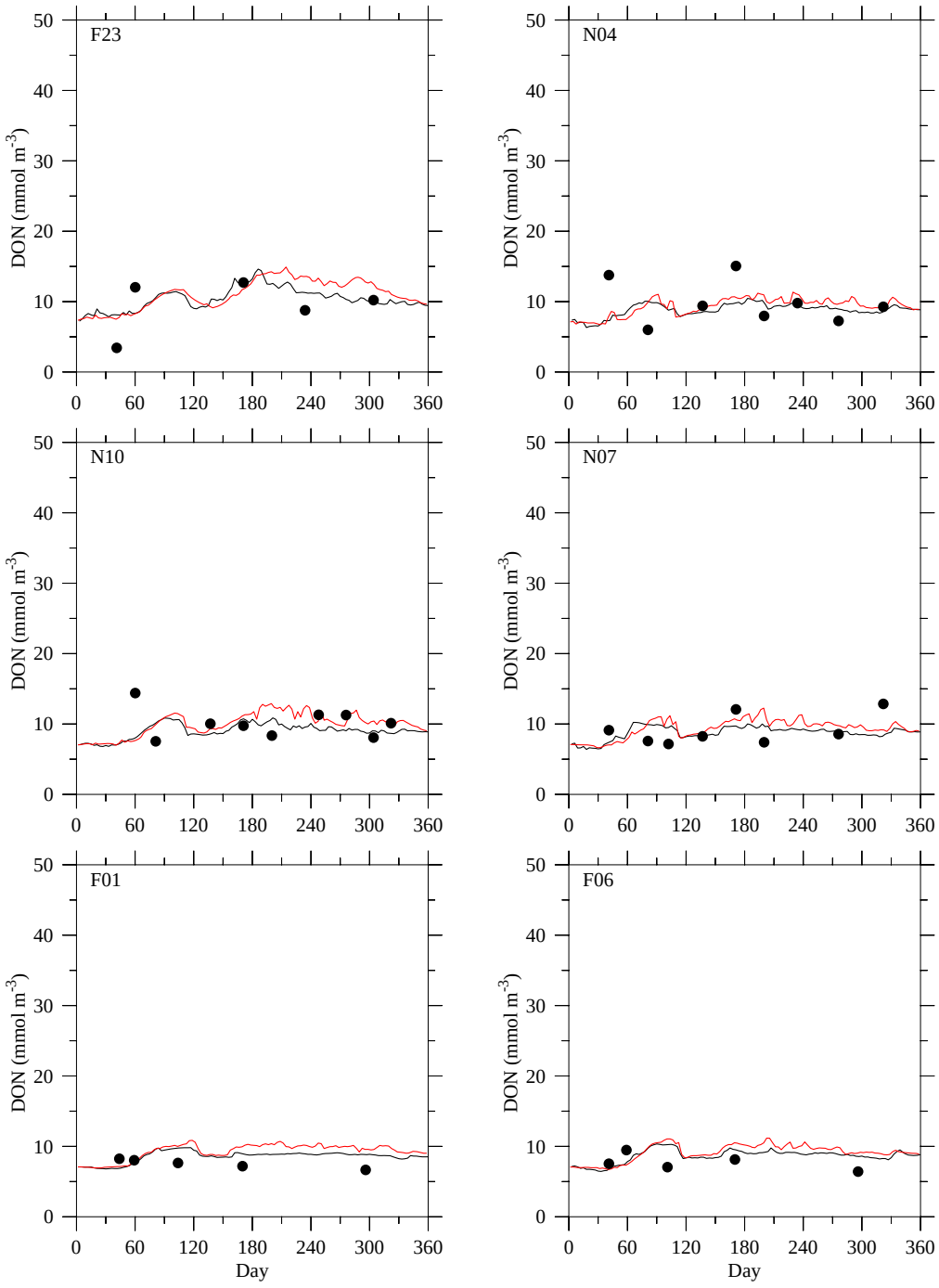

Figure 3.18 Comparison of surface dissolved organic nitrogen between UG-RCA (black lines) and RCA-v2 (red lines) at selected Massachusetts Bay monitoring stations in 2006. Dots are field measurements.

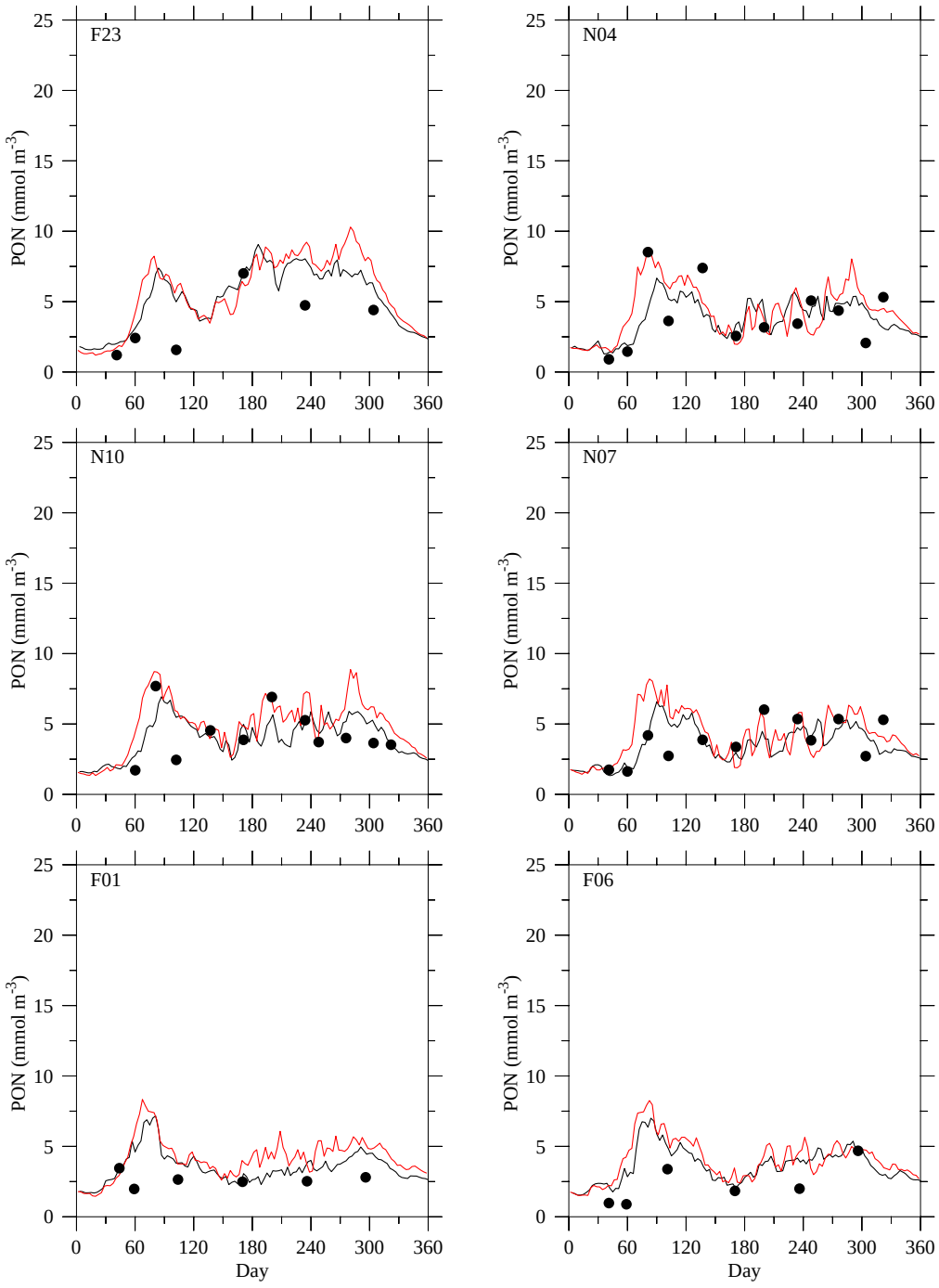

Figure 3.19 Comparison of surface particulate organic nitrogen between UG-RCA (black lines) and RCA-v2 (red lines) at selected Massachusetts Bay monitoring stations in 2006. Dots are field measurements.

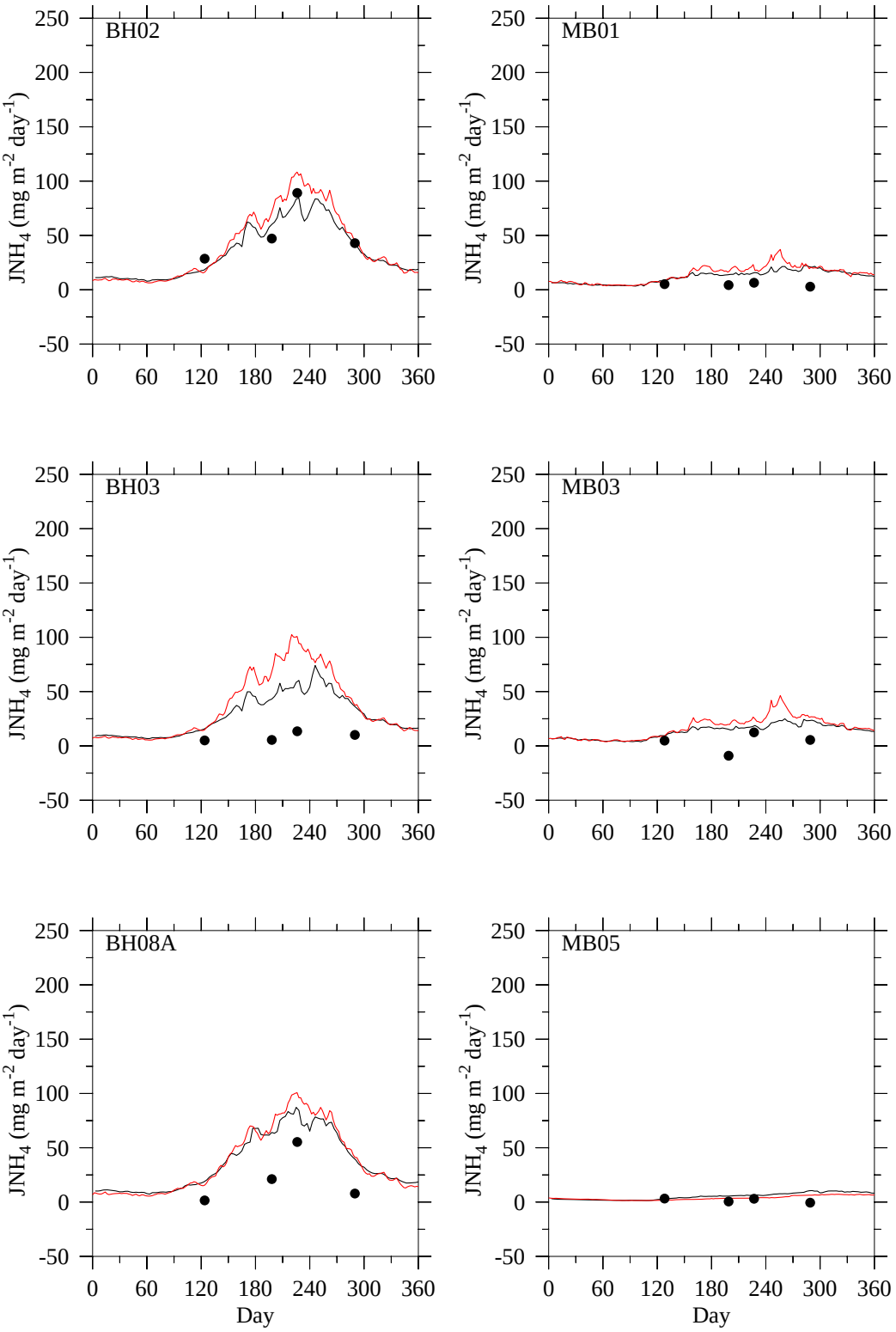

Figure 3.20 Comparison of ammonium flux at the sediment-water interface between UG-RCA (black lines) and RCA-v2 (red lines) at selected Massachusetts Bay monitoring stations in 2006. Dots are field measurements.

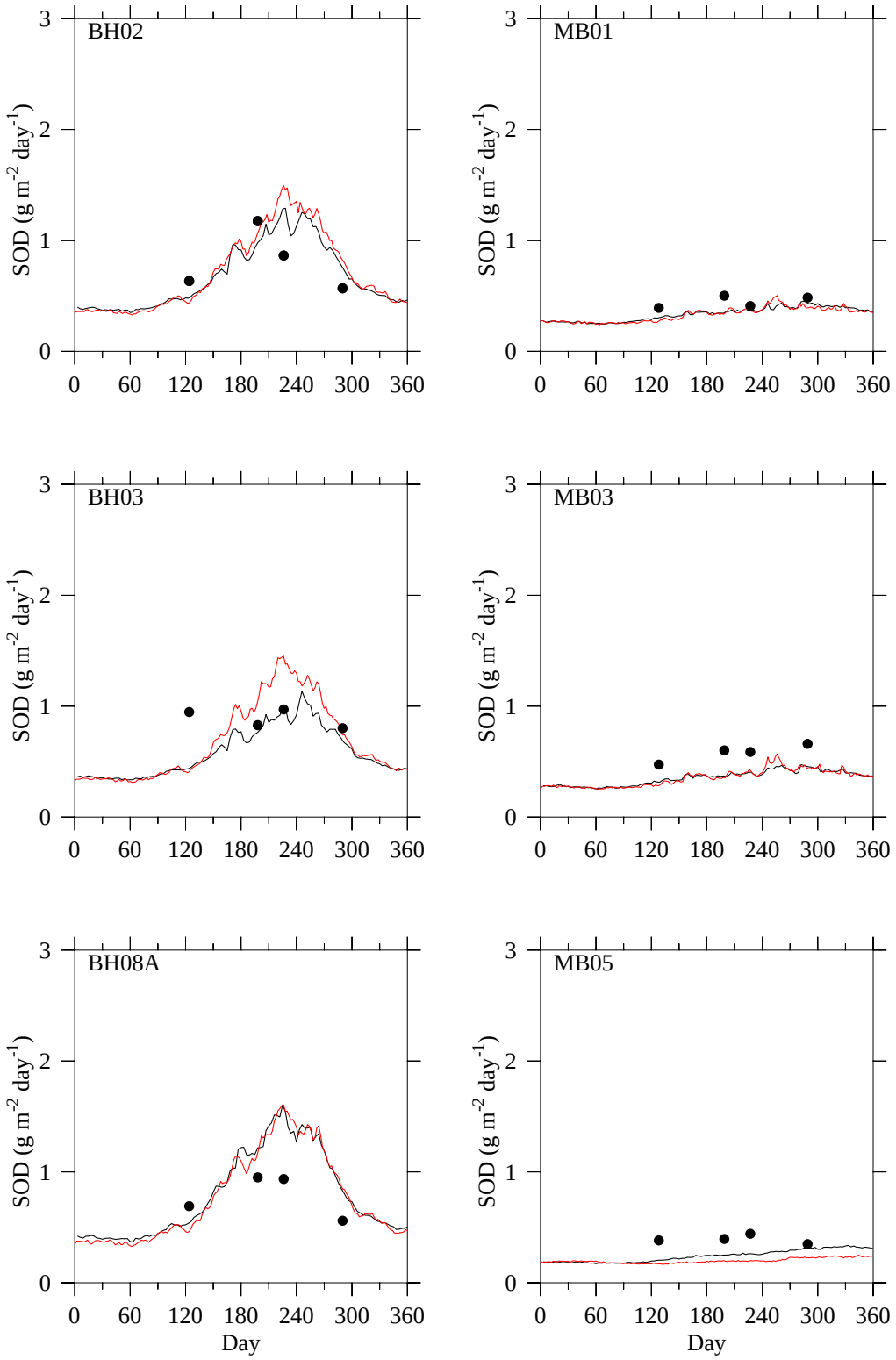

Figure 3.21 Comparison of dissolved oxygen demand at the sediment-water interface between UG-RCA (black lines) and RCA-v2 (red lines) at selected Massachusetts Bay monitoring stations in 2006. Dots are field measurements.

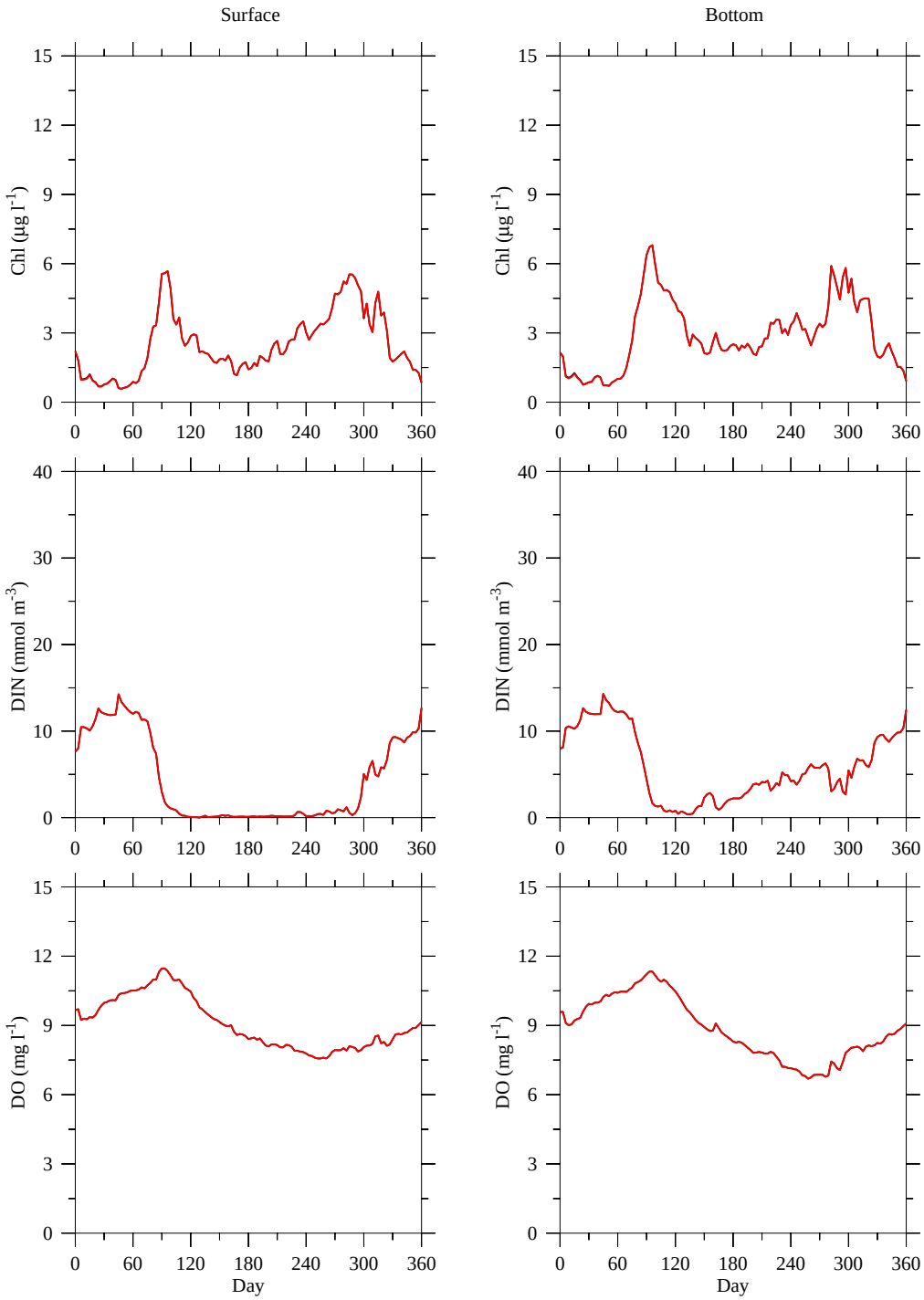

Figure 3.22 Example of comparison between total short-wave radiation-driven (red) and PAR-driven (black) simulation of chlorophyll, DIN and DO in surface and bottom waters at Station N10, simulated by UG-RCA for 2008.

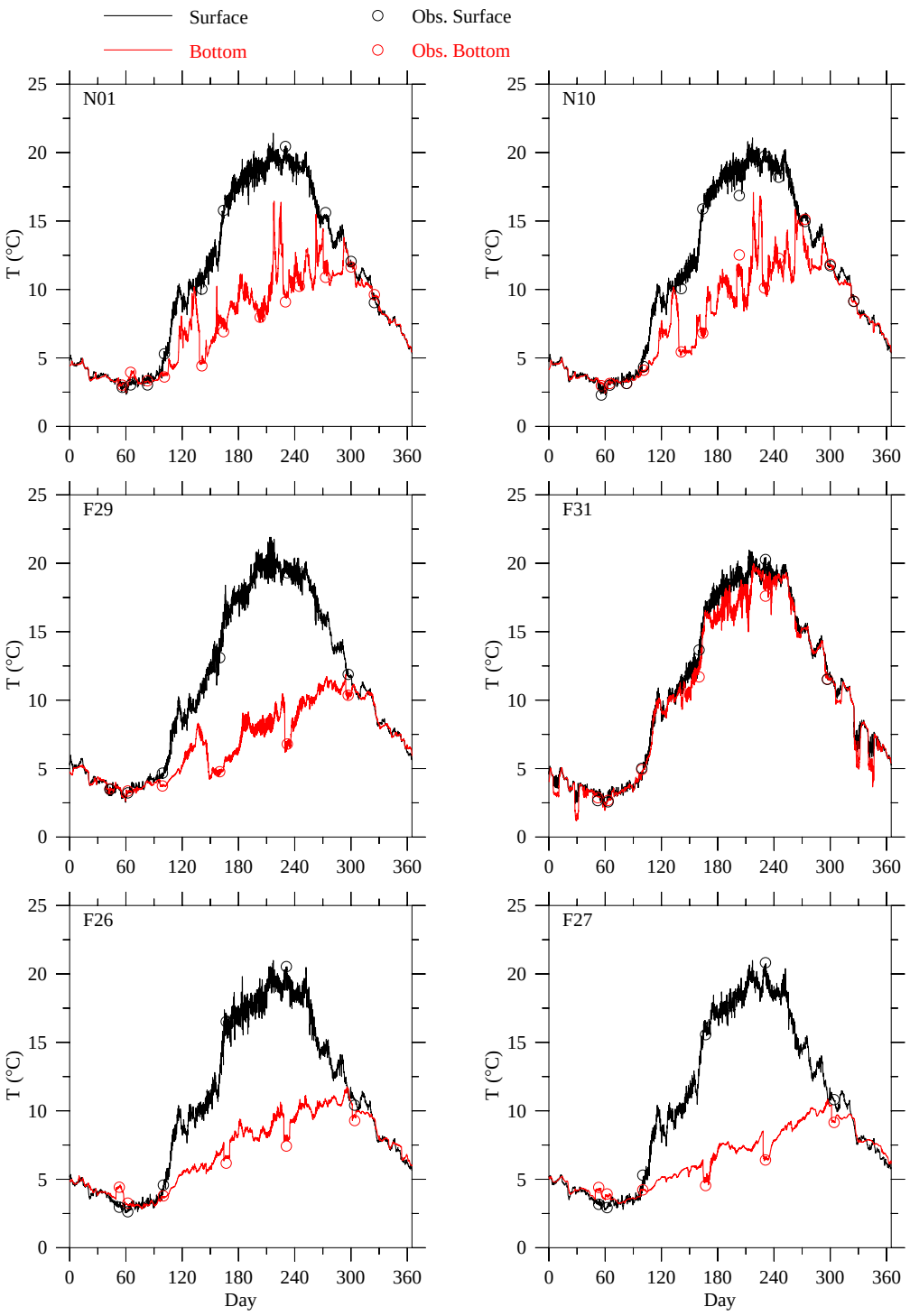

Figure 4.1 Comparison of observed (circles) and modeled (lines) time-series data of temperature at selected Massachusetts Bay monitoring stations in 2008.

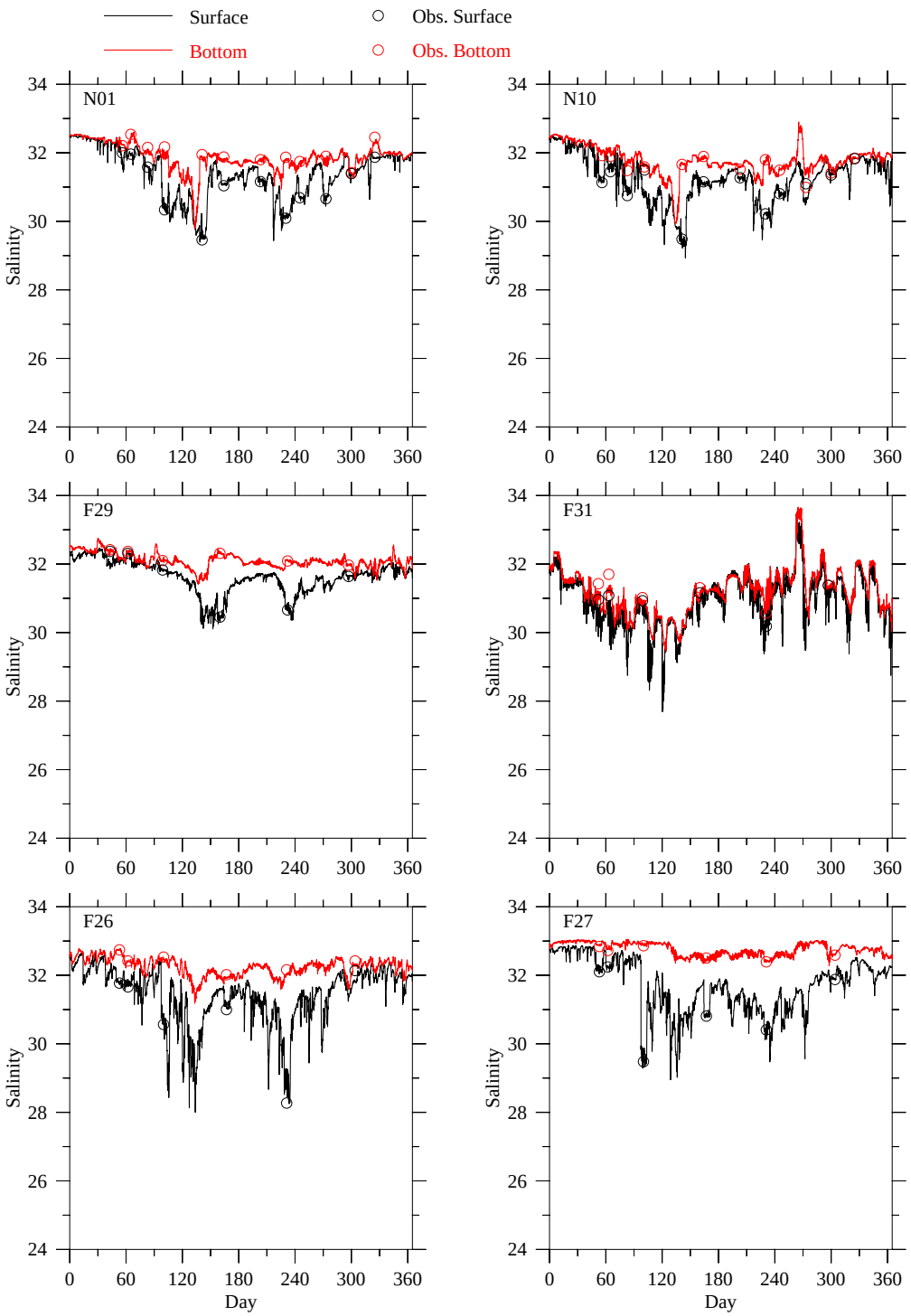

Figure 4.2 Comparison of observed (circles) and modeled (lines) time-series data of salinity at selected Massachusetts Bay monitoring stations in 2008.

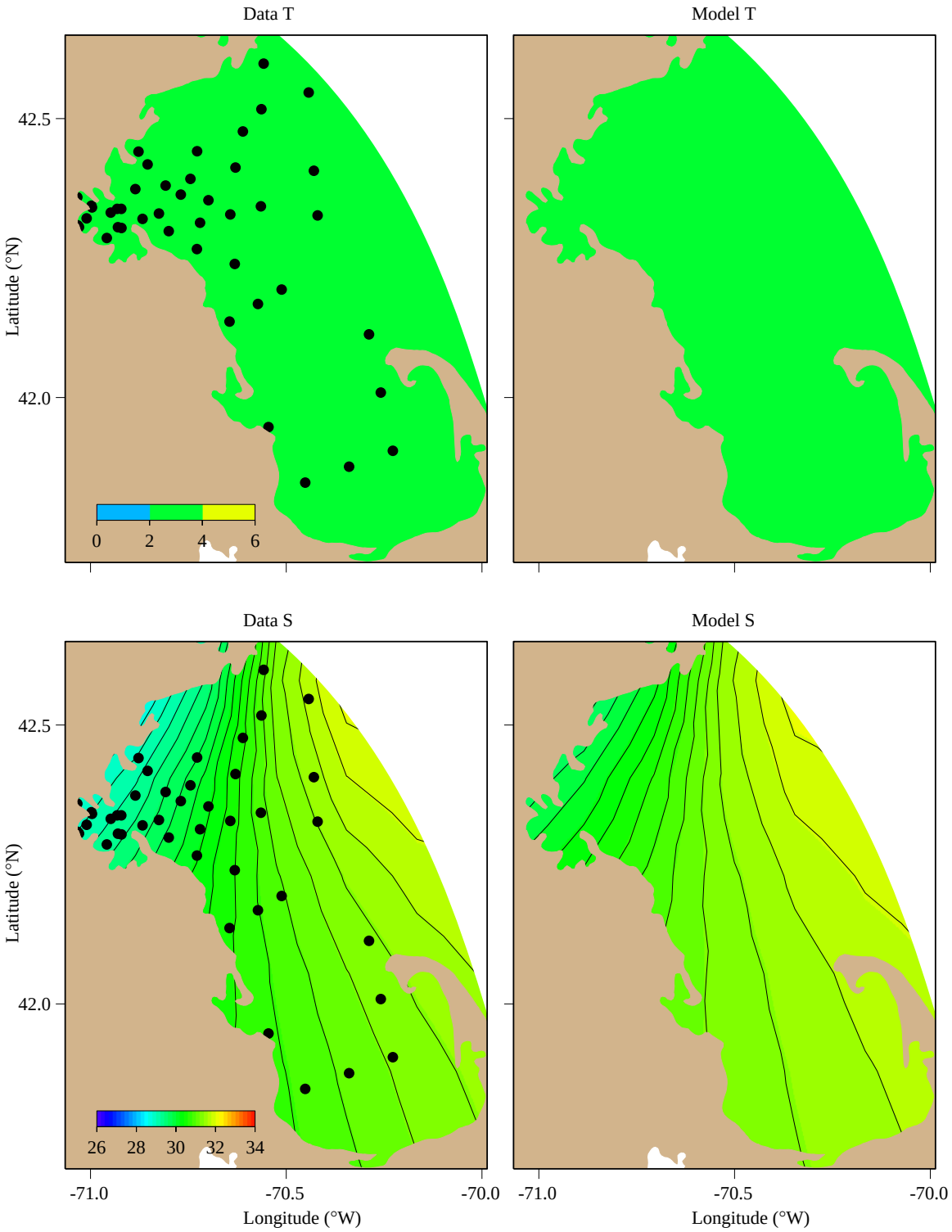

Figure 4.3 Comparison between observed (left) and model-computed (right) near-surface temperatures (upper panels) and salinities (lower panels) in February 2008.

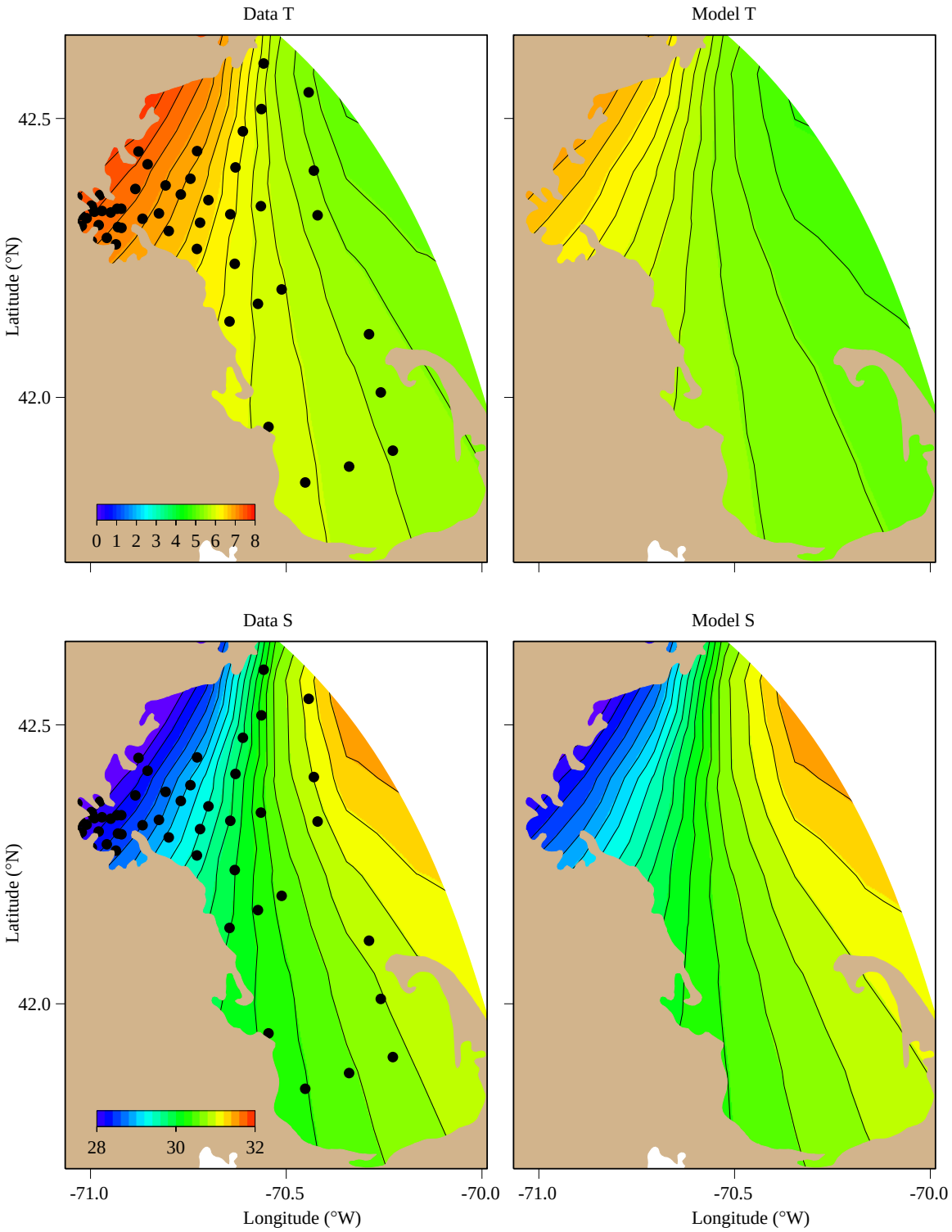

Figure 4.4 Comparison between observed (left) and model-computed (right) near-surface temperatures (upper panels) and salinities (lower panels) in April 2008.

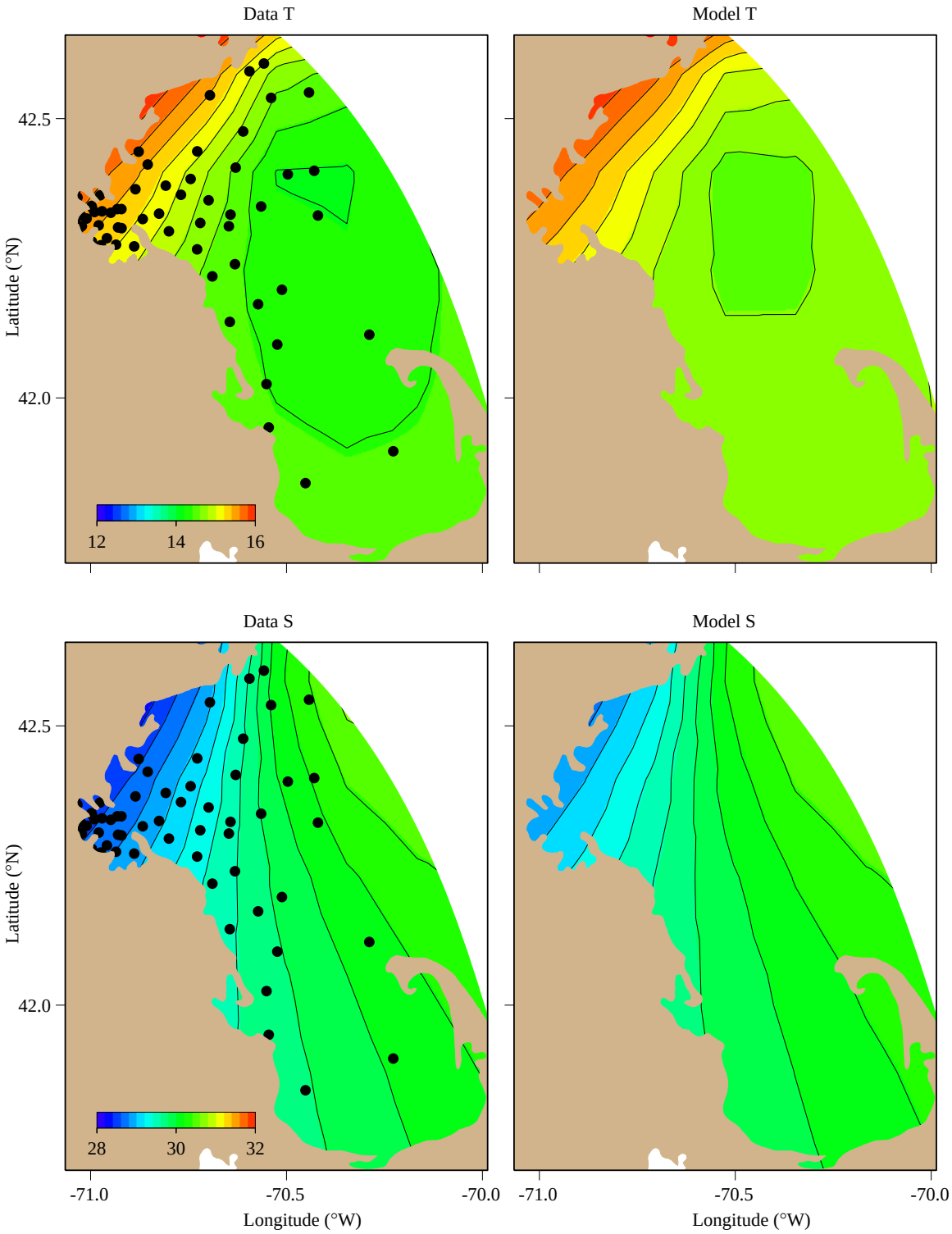

Figure 4.5 Comparison between observed (left) and model-computed (right) near-surface temperatures (upper panels) and salinities (lower panels) in June 2008.

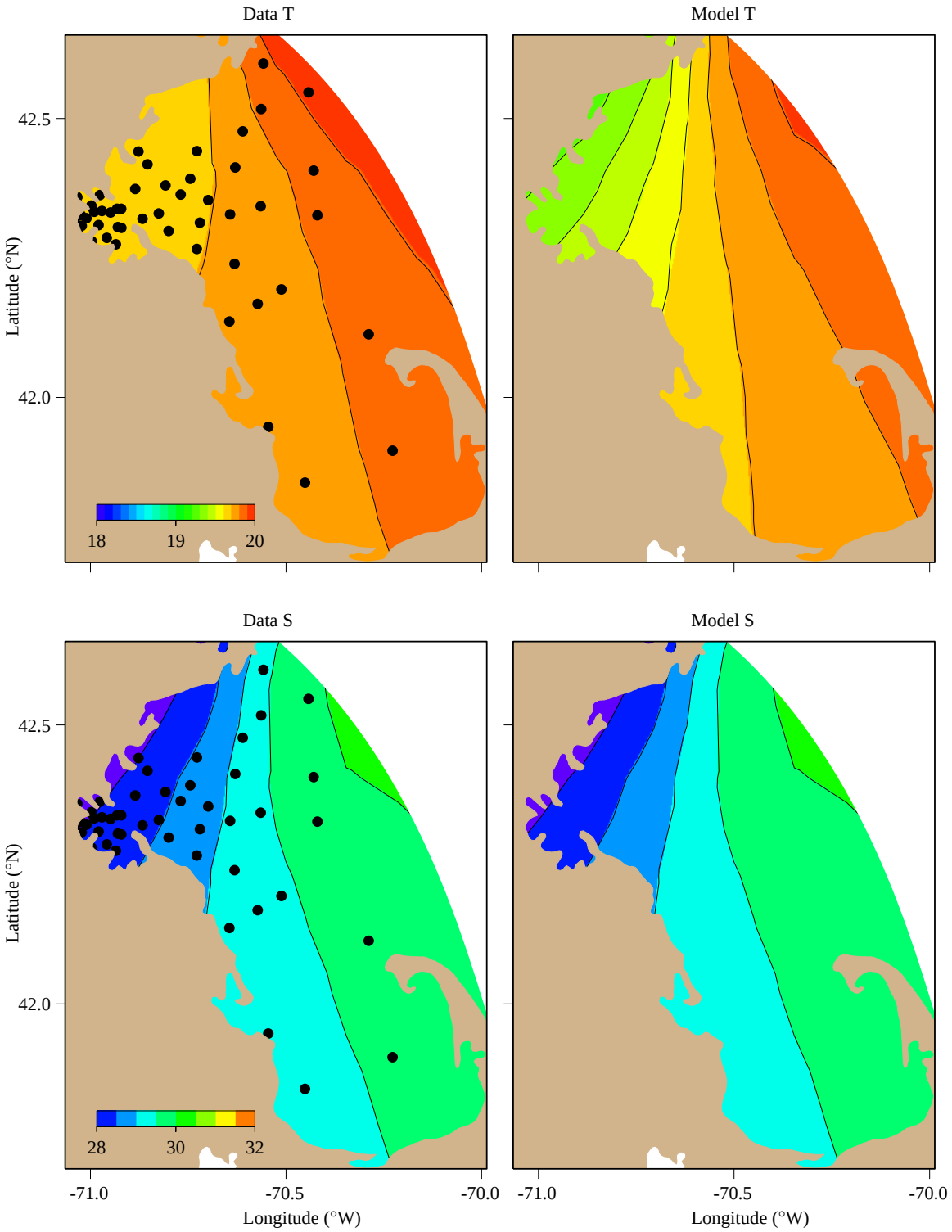

Figure 4.6 Comparison between observed (left) and model-computed (right) near-surface temperatures (upper panels) and salinities (lower panels) in August 2008.

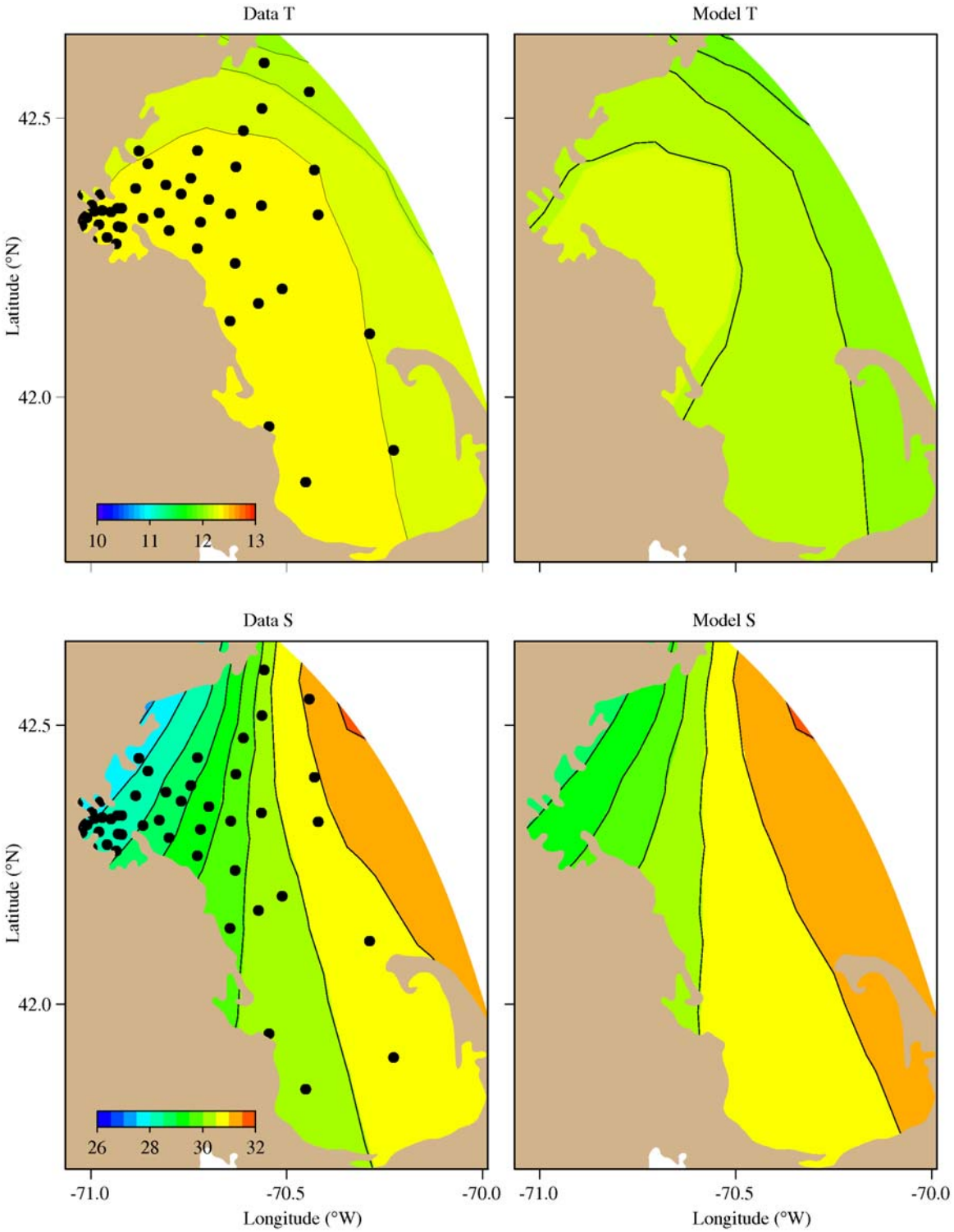

Figure 4.7 Comparison between observed (left) and model-computed (right) near-surface temperatures (upper panels) and salinities (lower panels) in October 2008.

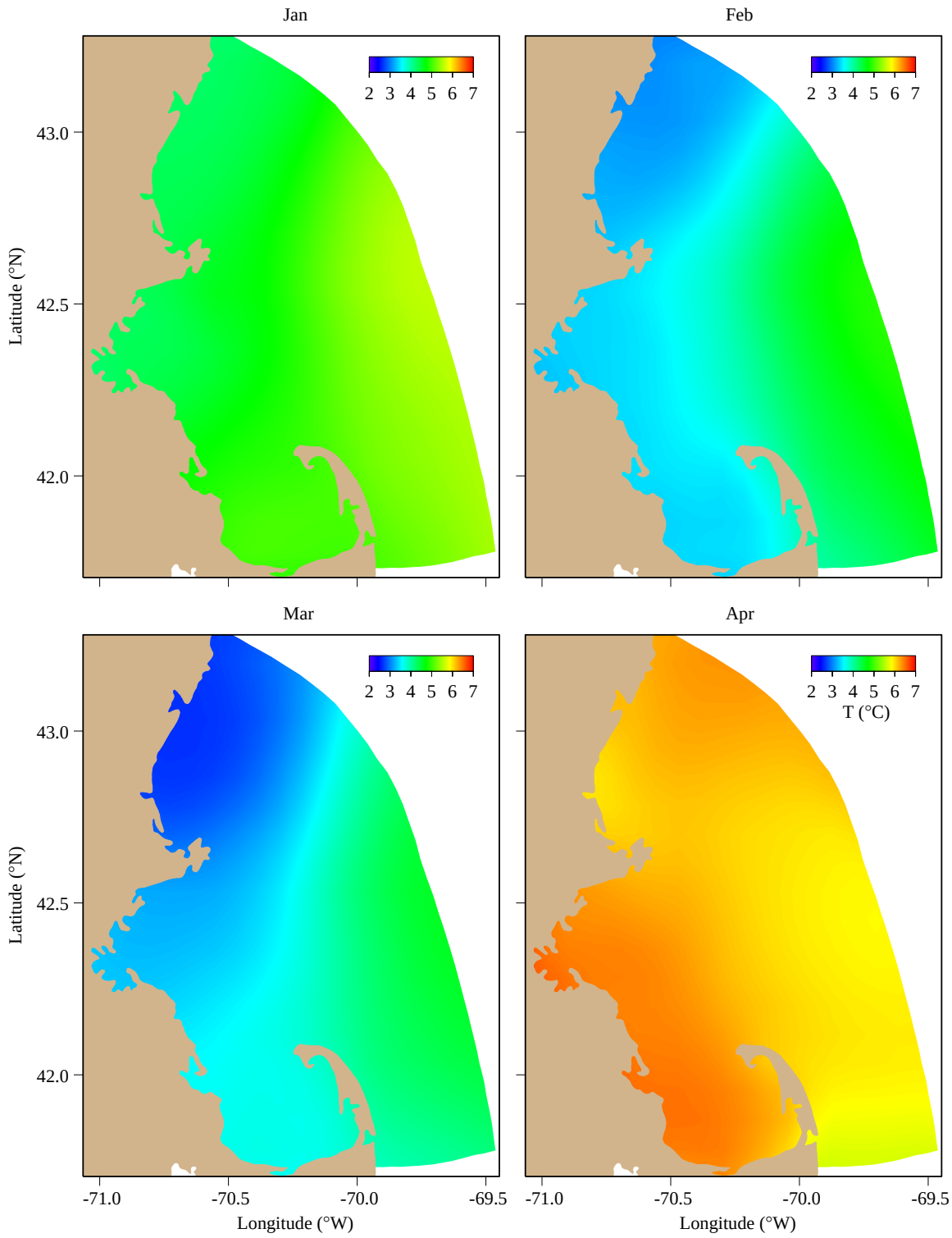

Figure 4.8 Model-predicted monthly-averaged surface temperature in January, February, March and April, 2008.

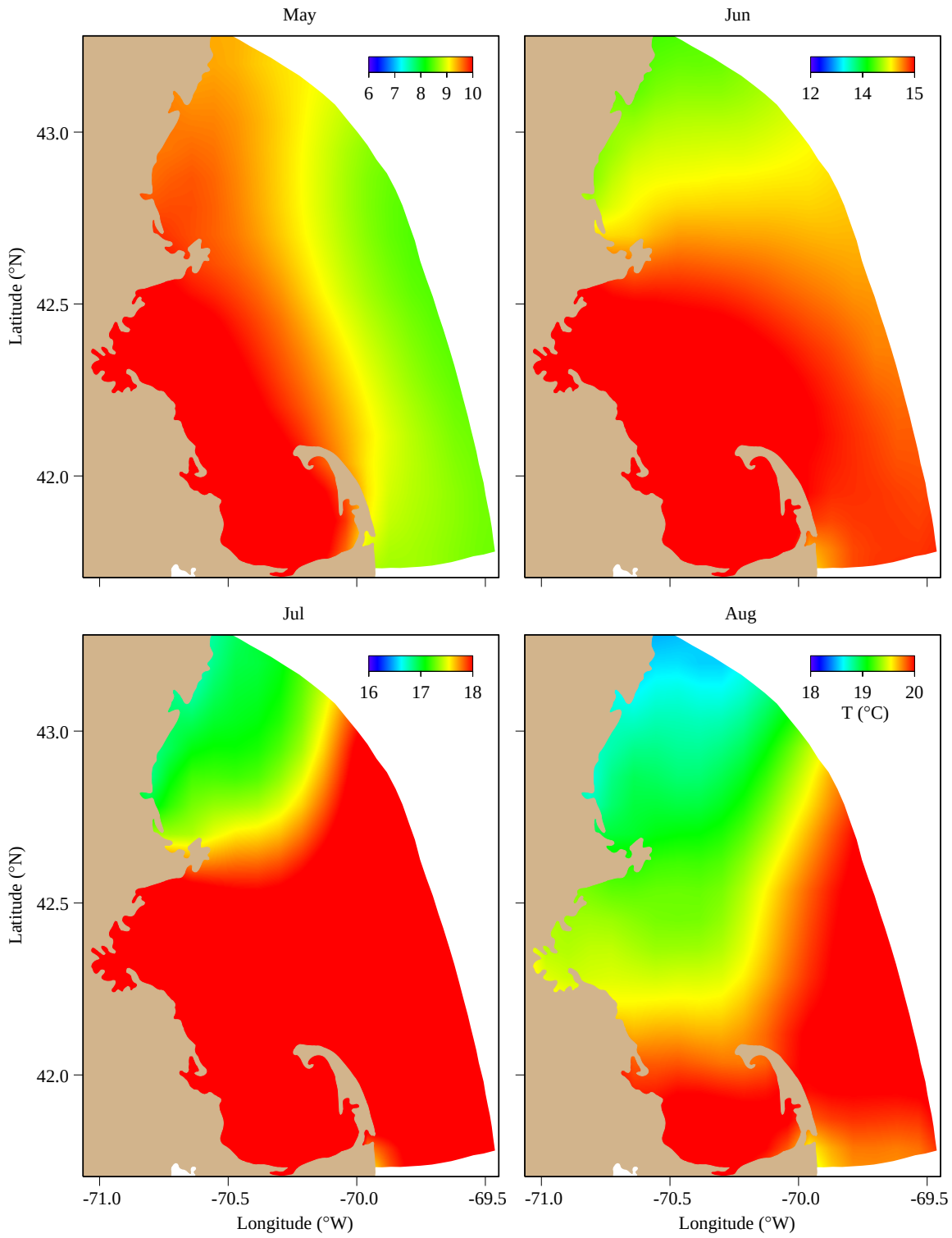

Figure 4.9 Model-predicted monthly-averaged surface temperature in May, June, July and August, 2008.

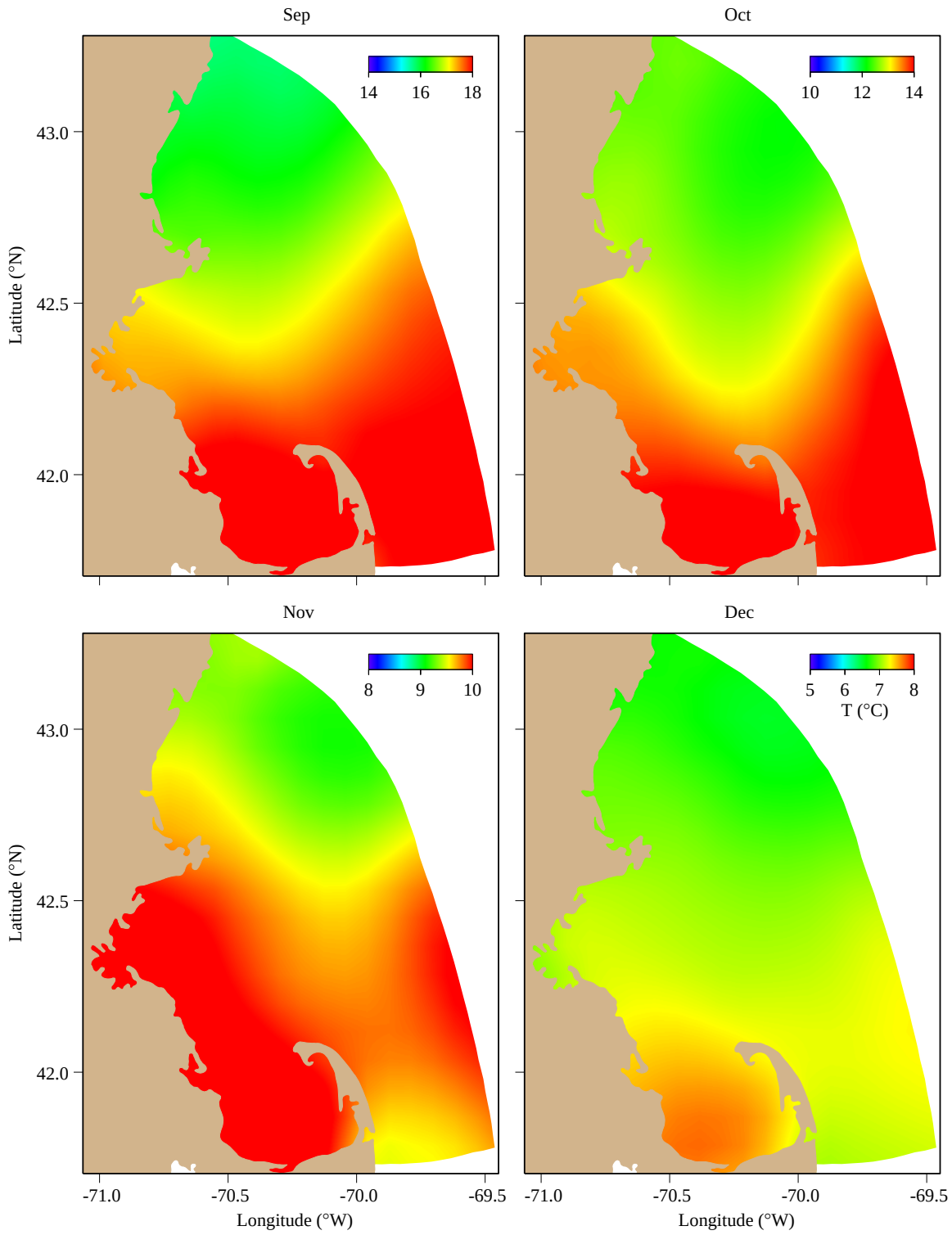

Figure 4.10 Model-predicted monthly-averaged surface temperature in September, October, November and December, 2008.

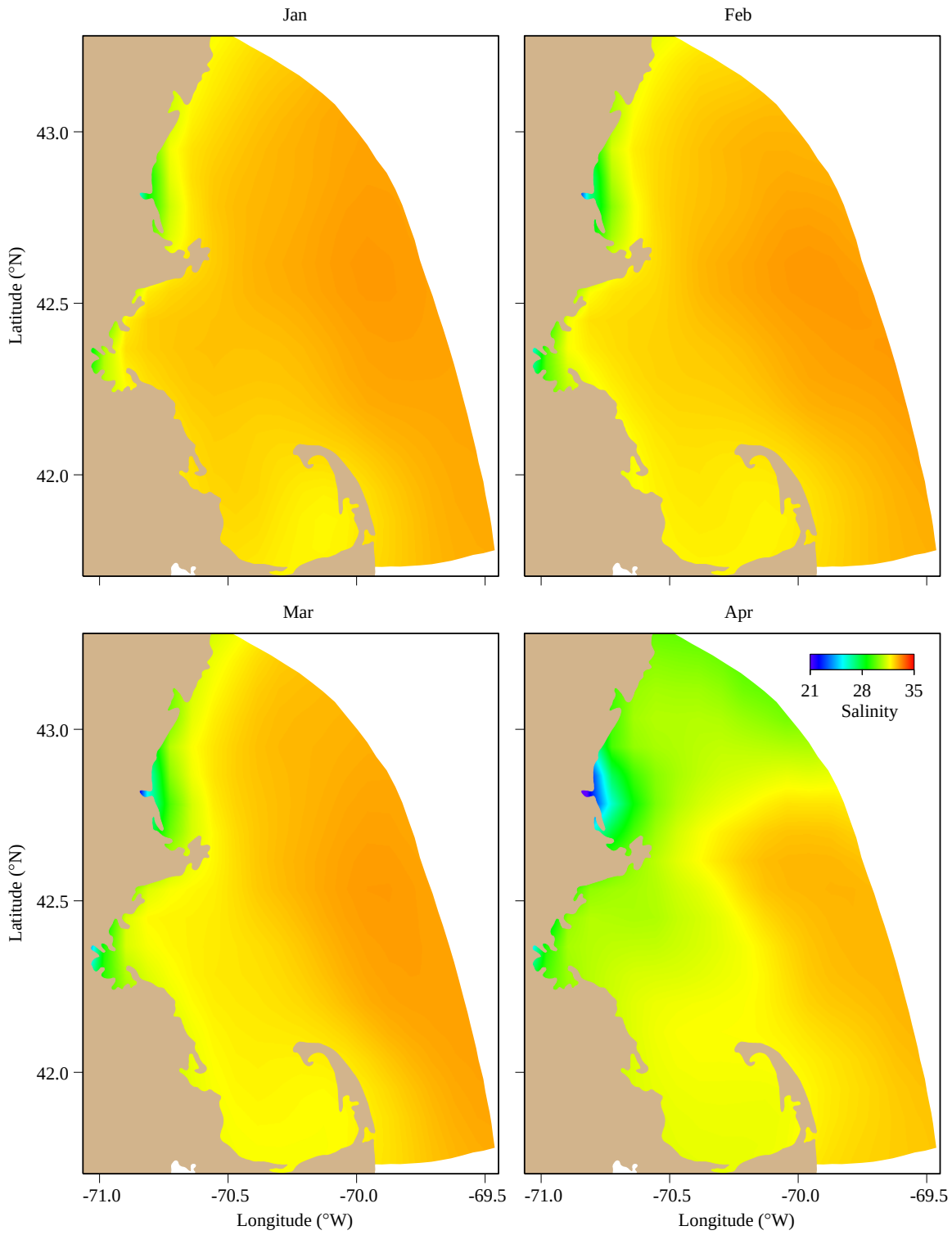

Figure 4.11 Model-predicted monthly-averaged surface salinity in January, February, March and April, 2008.

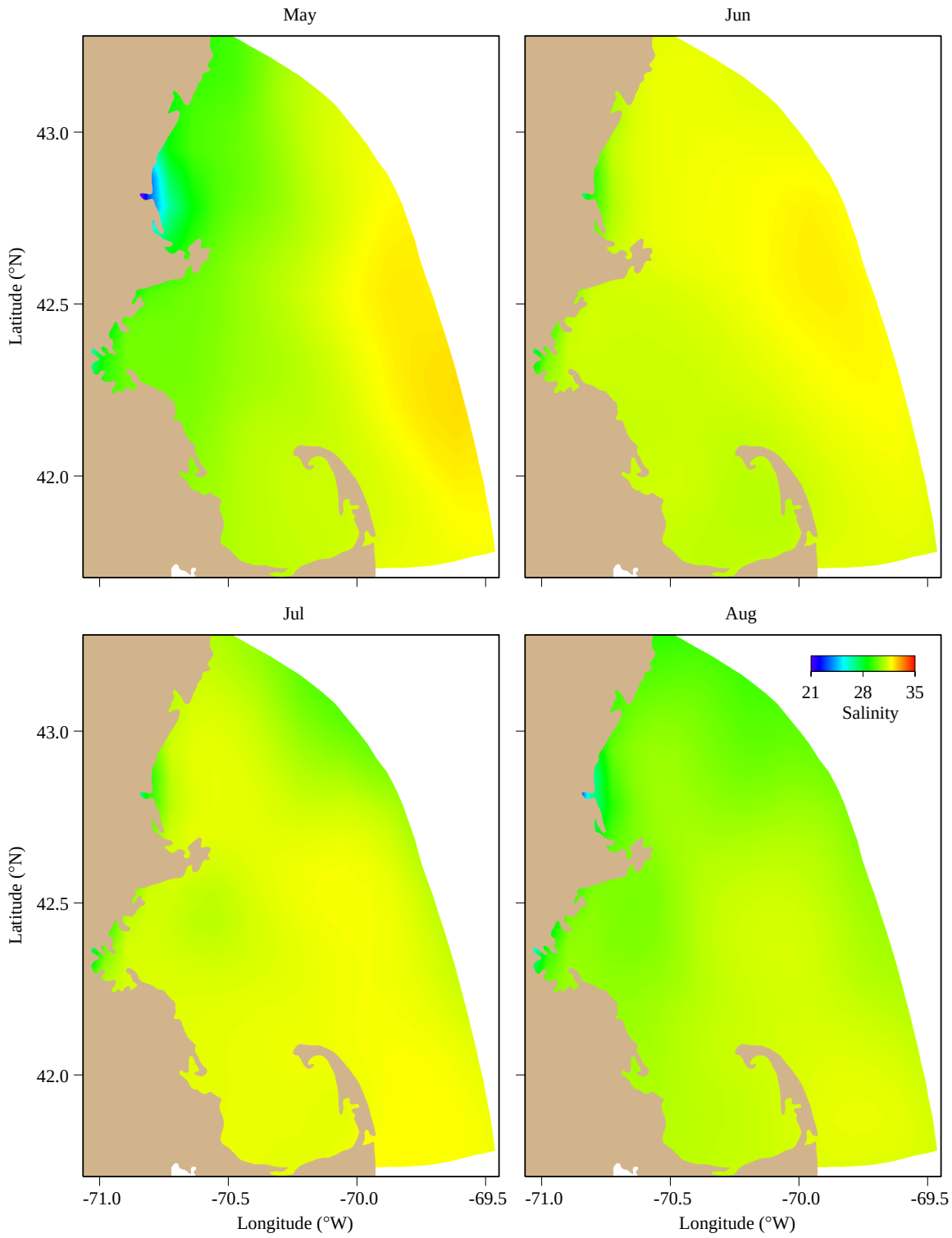

Figure 4.12 Model-predicted monthly-averaged surface salinity in May, June, July and August, 2008.

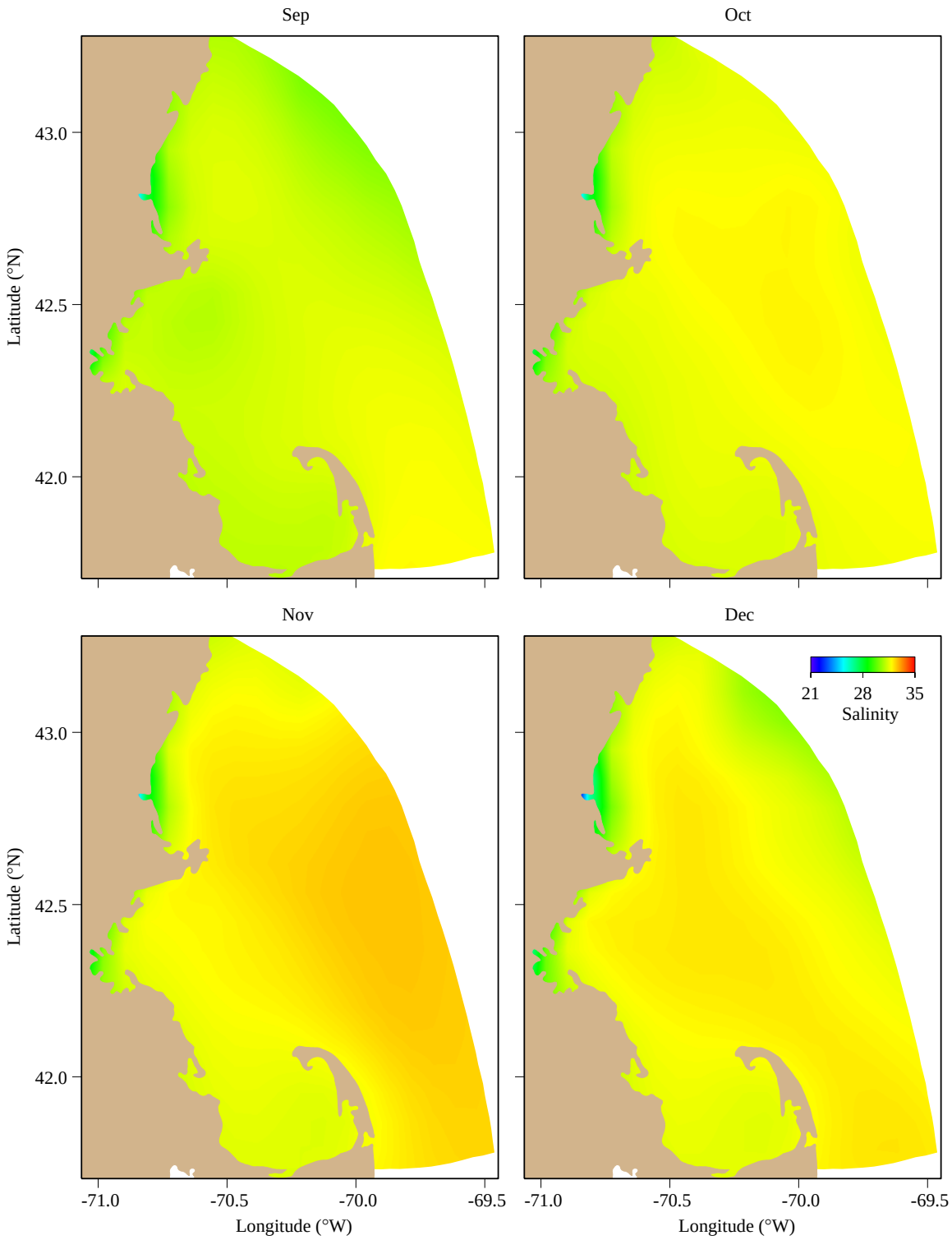

Figure 4.13 Model-predicted monthly-averaged surface salinity in September, October, November and December, 2008.

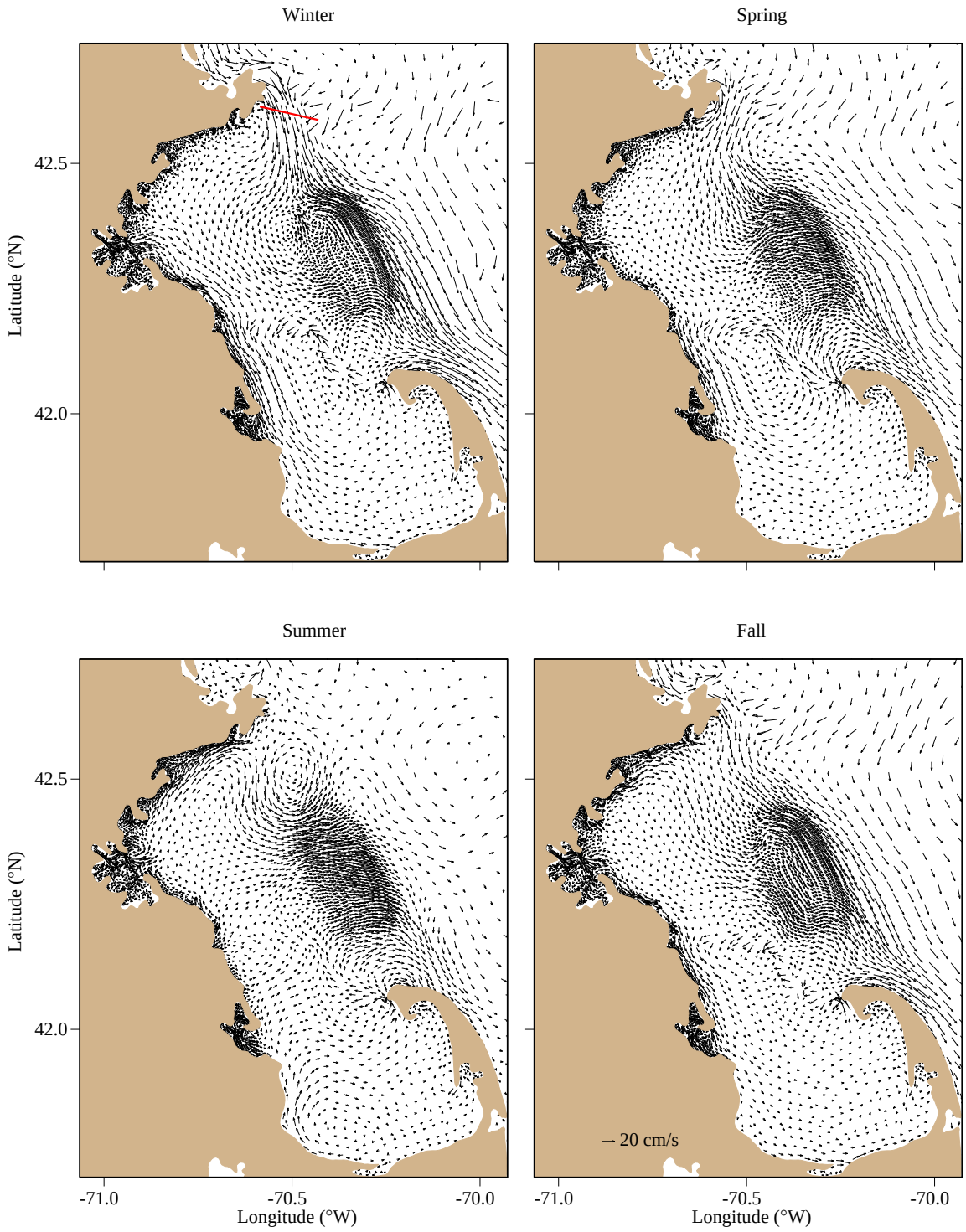

Figure 4.14 Model-predicted seasonally-averaged surface current in 2008. Red line indicates the transect on which daily transport was calculated (see Figure 4.15).

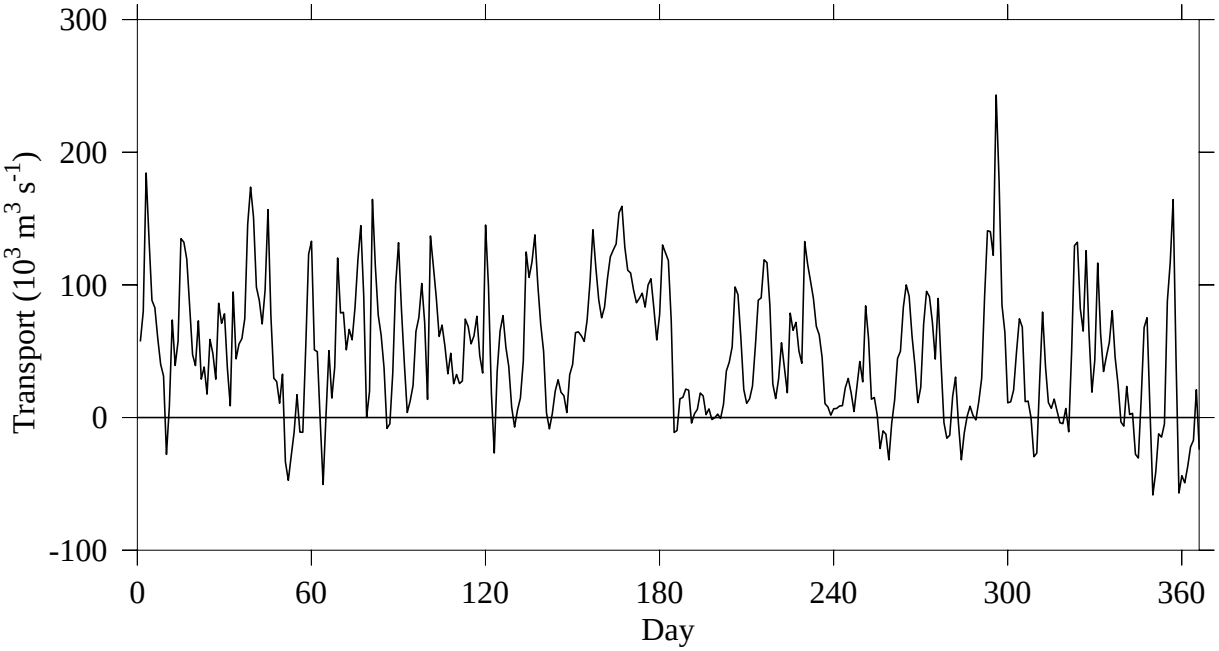

Figure 4.15 Daily averaged water transport across the Cape Ann transect depicted in Figure 4.14. Positive values are southwestward transport toward Massachusetts Bay.

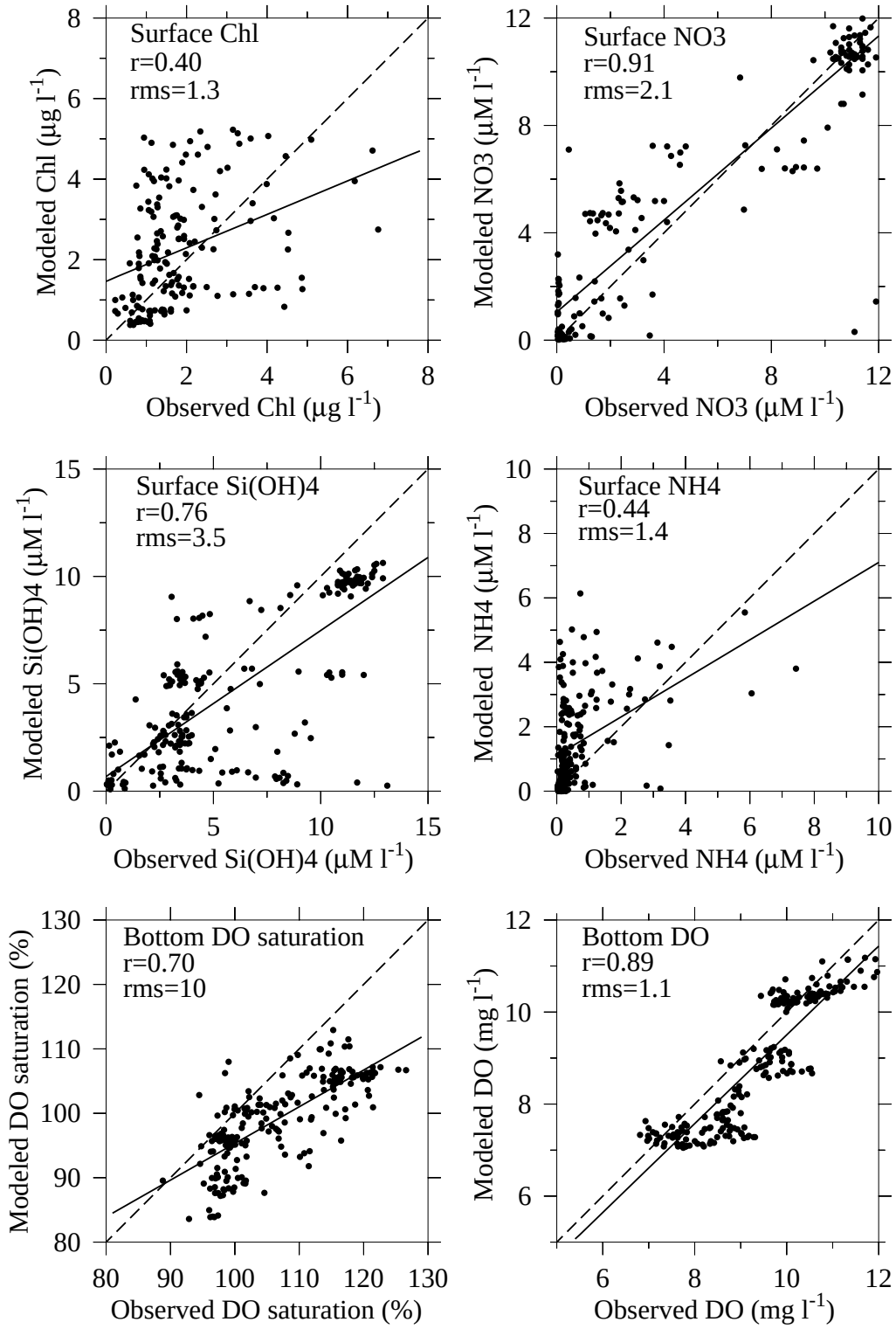

Figure 4.16 Overall correlation and regression (solid lines) between observed (abscissa) and modeled (ordinate) results of key parameters in 2008. The dashed lines indicate the equal relationship between observed and modeled results.

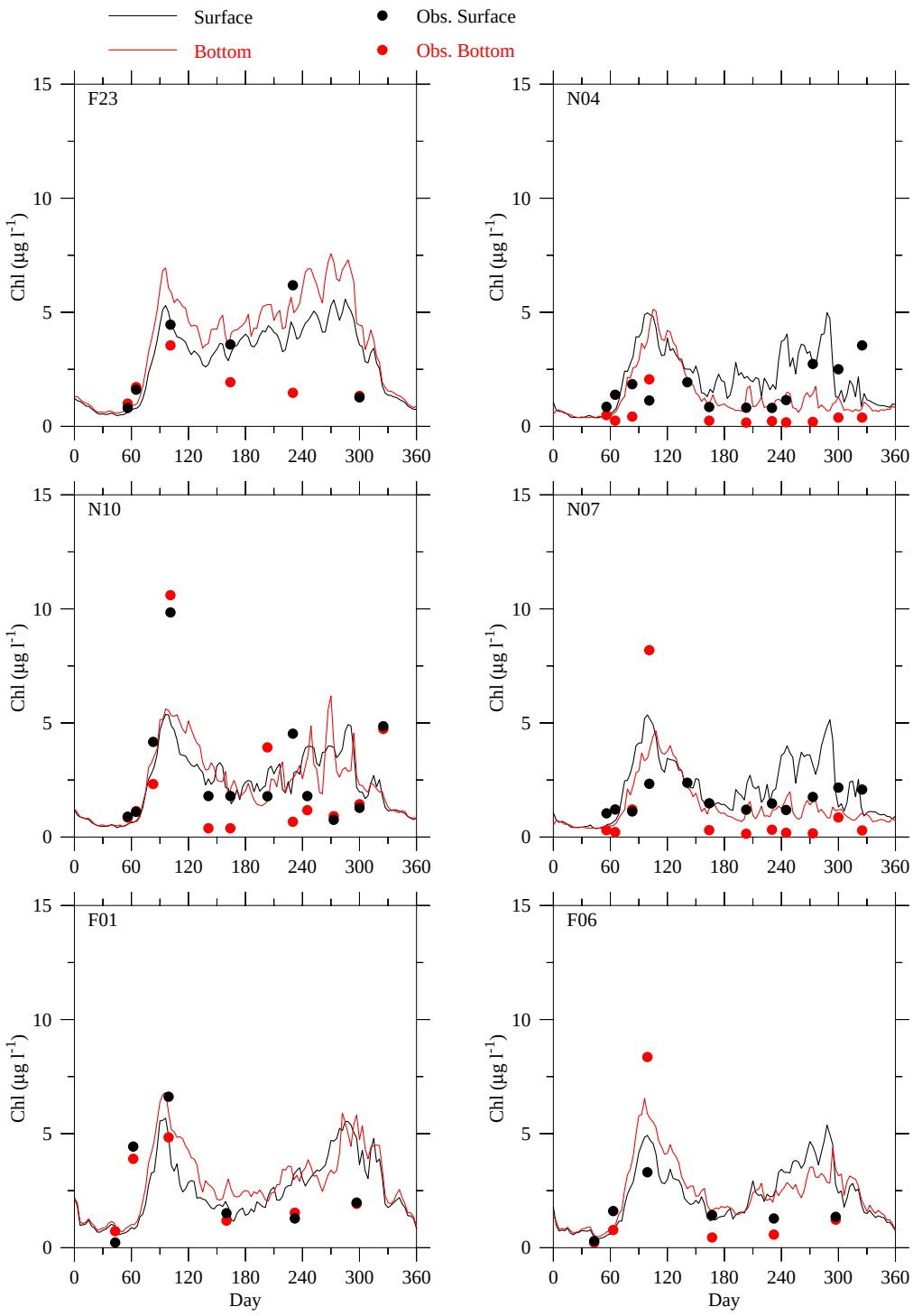

Figure 4.17 Comparison of observed (dots) and modeled (lines) time-series data of chlorophyll at selected Massachusetts Bay monitoring stations in 2008.

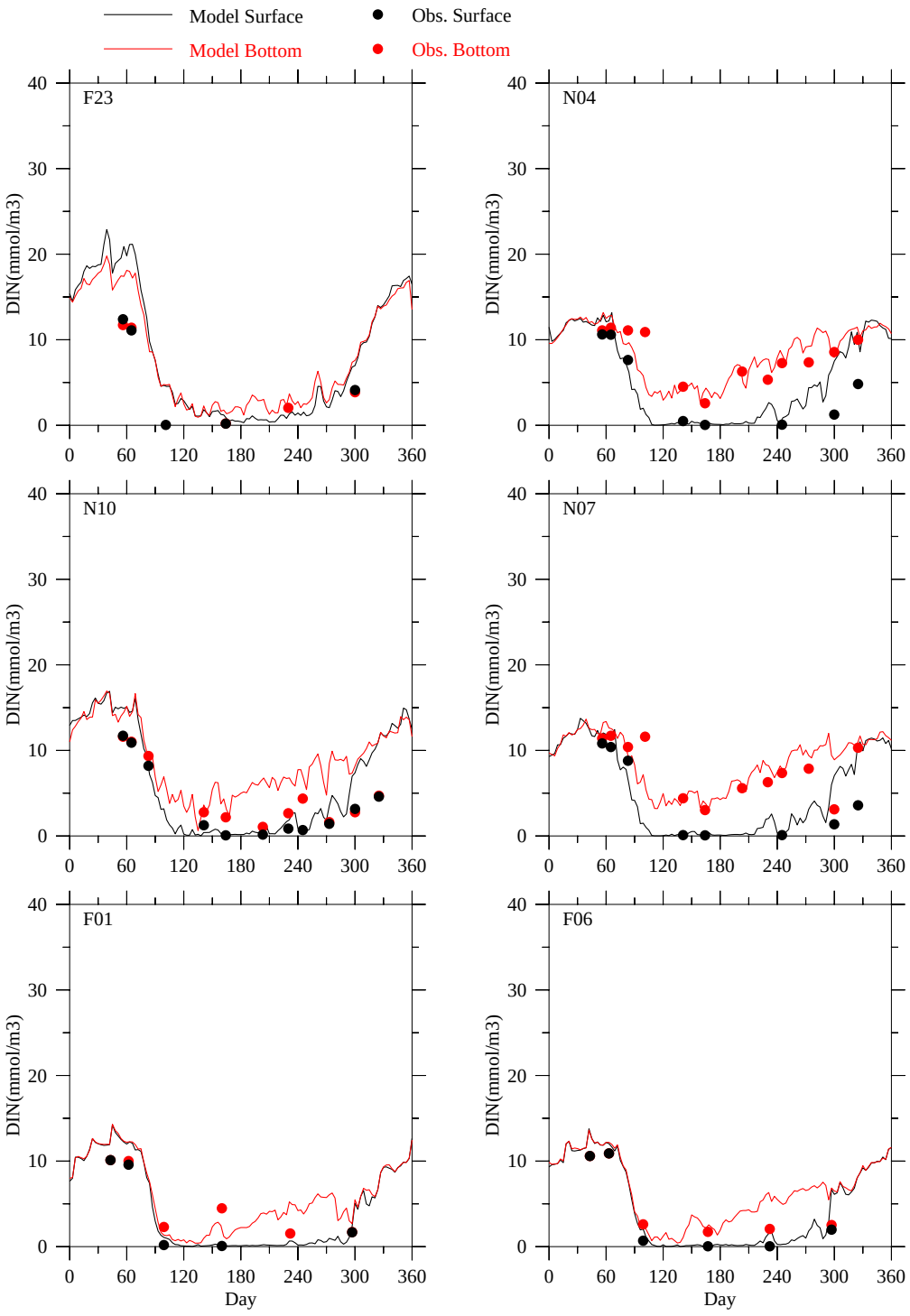

Figure 4.18 Comparison of observed (dots) and modeled (lines) time-series data of DIN at selected Massachusetts Bay monitoring stations in 2008.

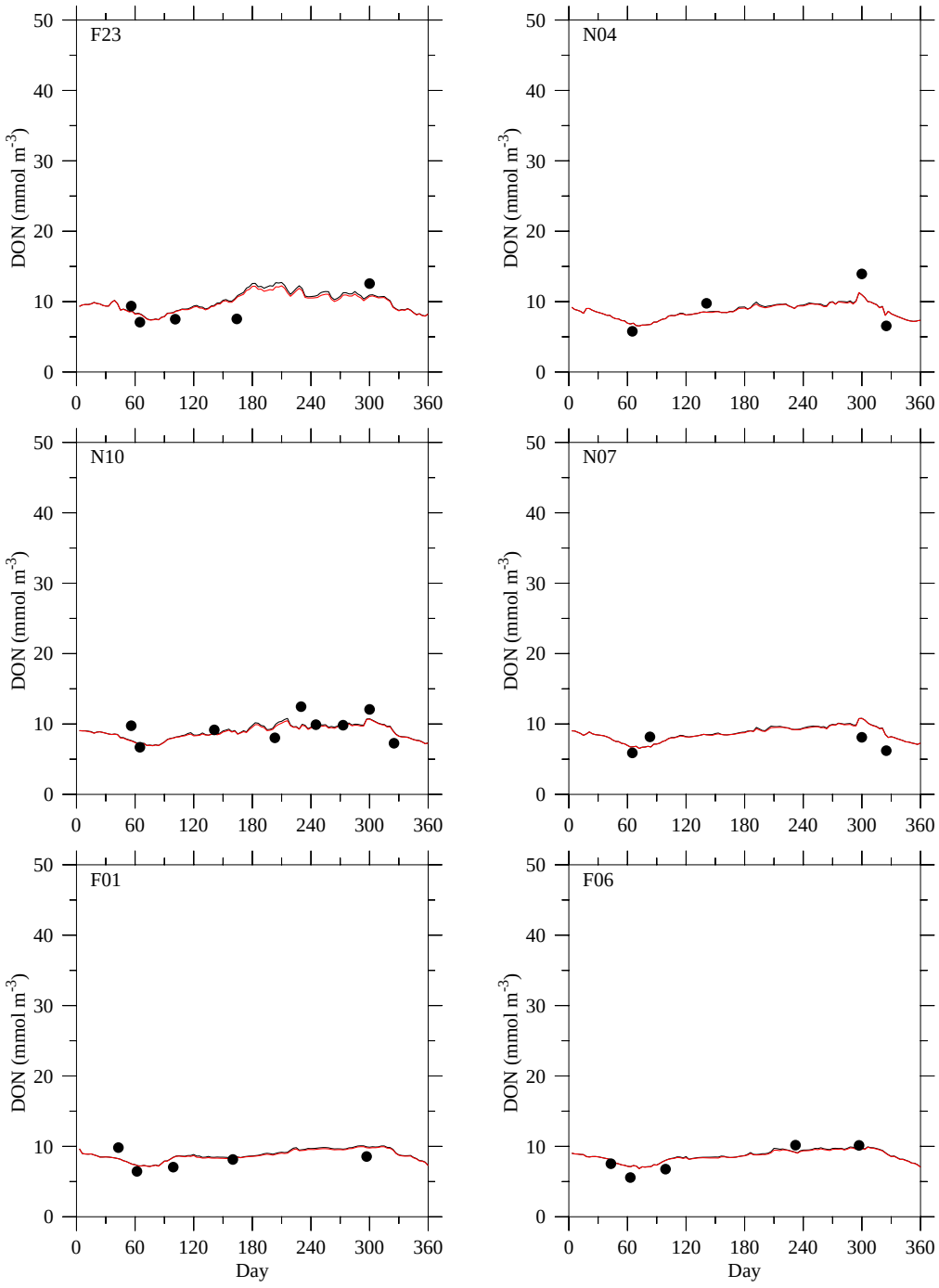

Figure 4.19 Comparison of observed (dots) and modeled (lines) time-series data of DON at selected Massachusetts Bay monitoring stations in 2008.

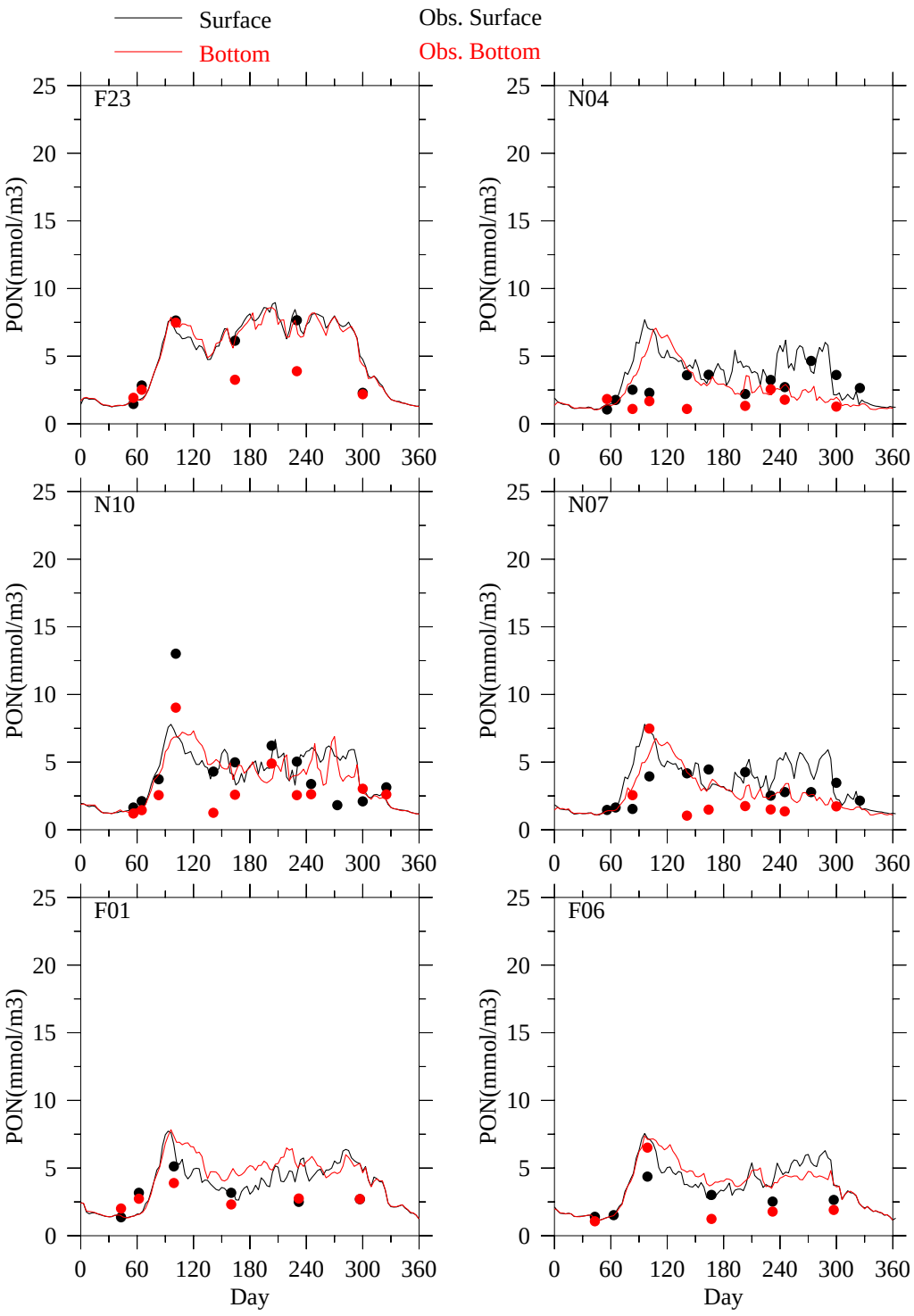

Figure 4.20 Comparison of observed (dots) and modeled (lines) time-series data of PON at selected Massachusetts Bay monitoring stations in 2008.

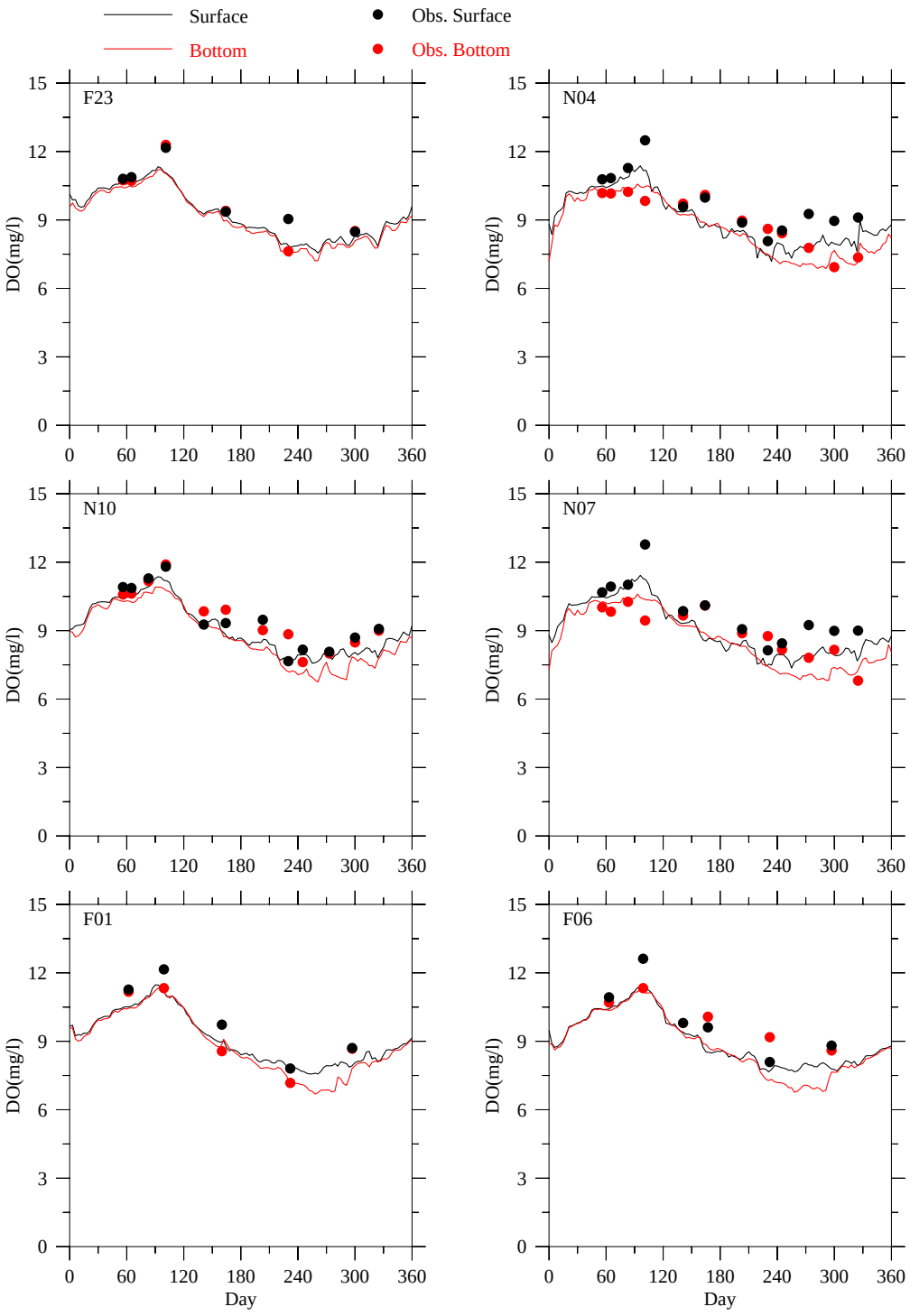

Figure 4.21 Comparison of observed (dots) and modeled (lines) time-series data of DO at selected Massachusetts Bay monitoring stations in 2008.

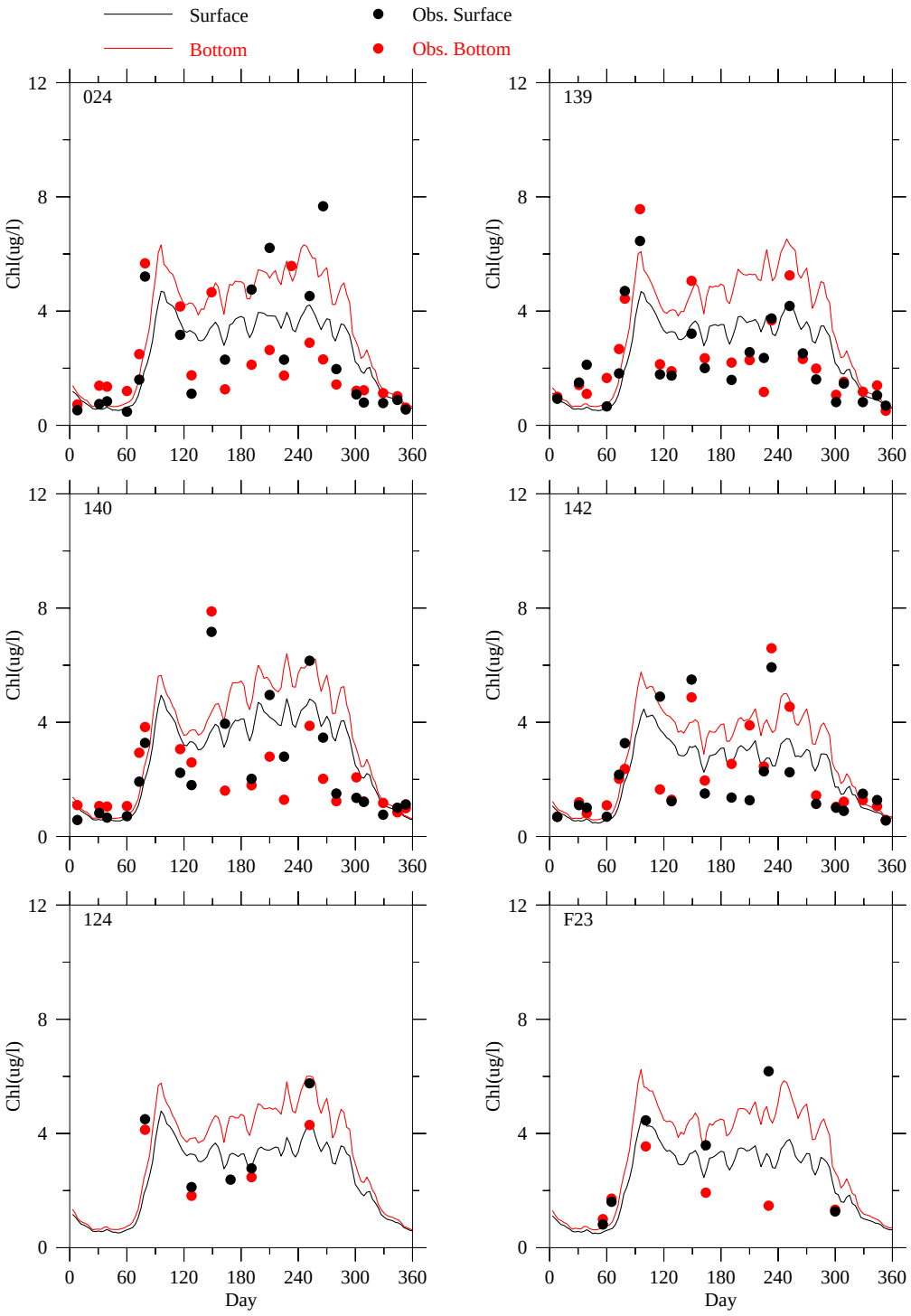

Figure 4.22 Comparison of observed (dots) and modeled (lines) time-series data of chlorophyll at selected Boston Harbor monitoring stations in 2008.

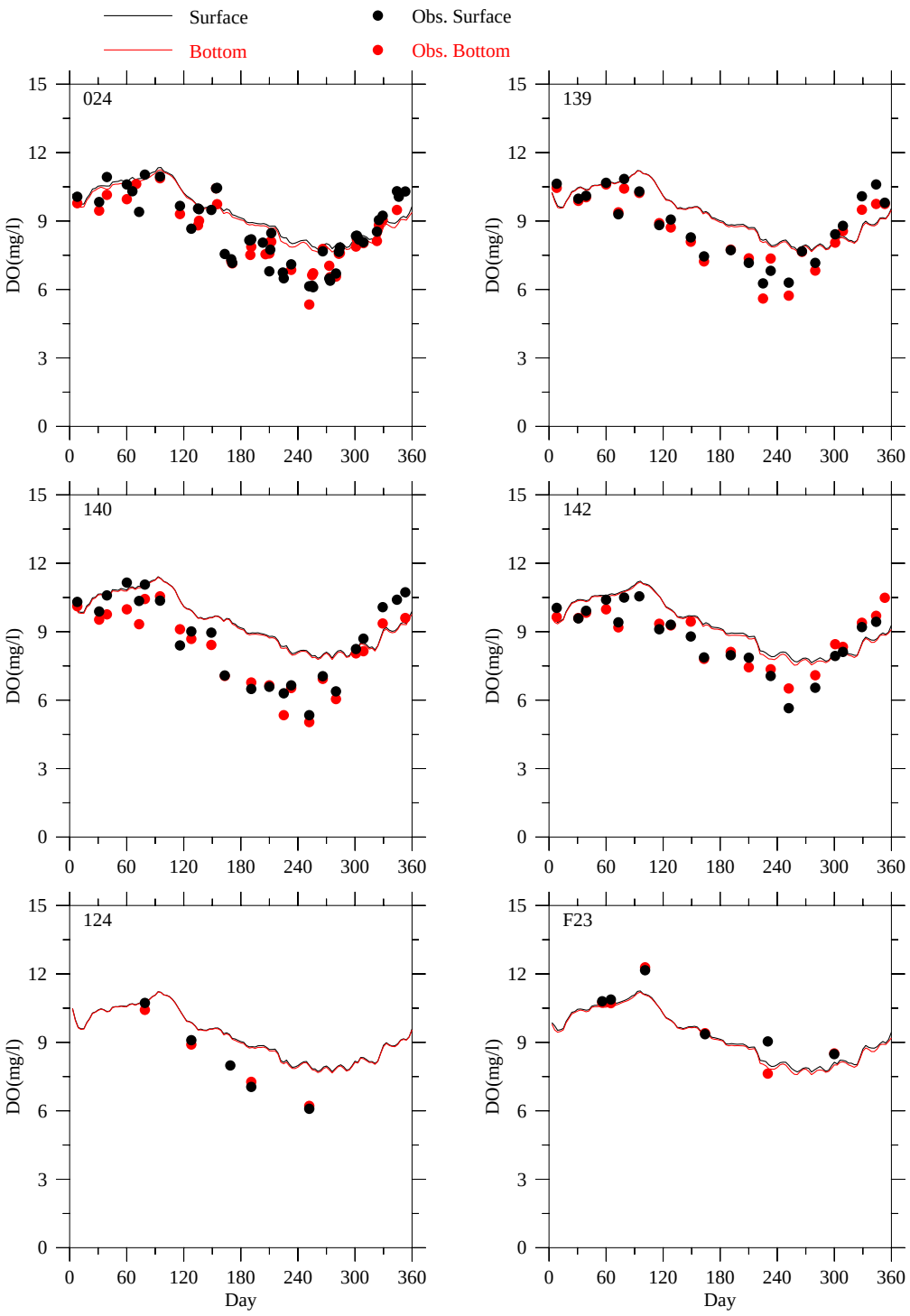

Figure 4.23 Comparison of observed (dots) and modeled (lines) time-series data of DO at selected Boston Harbor monitoring stations in 2008.

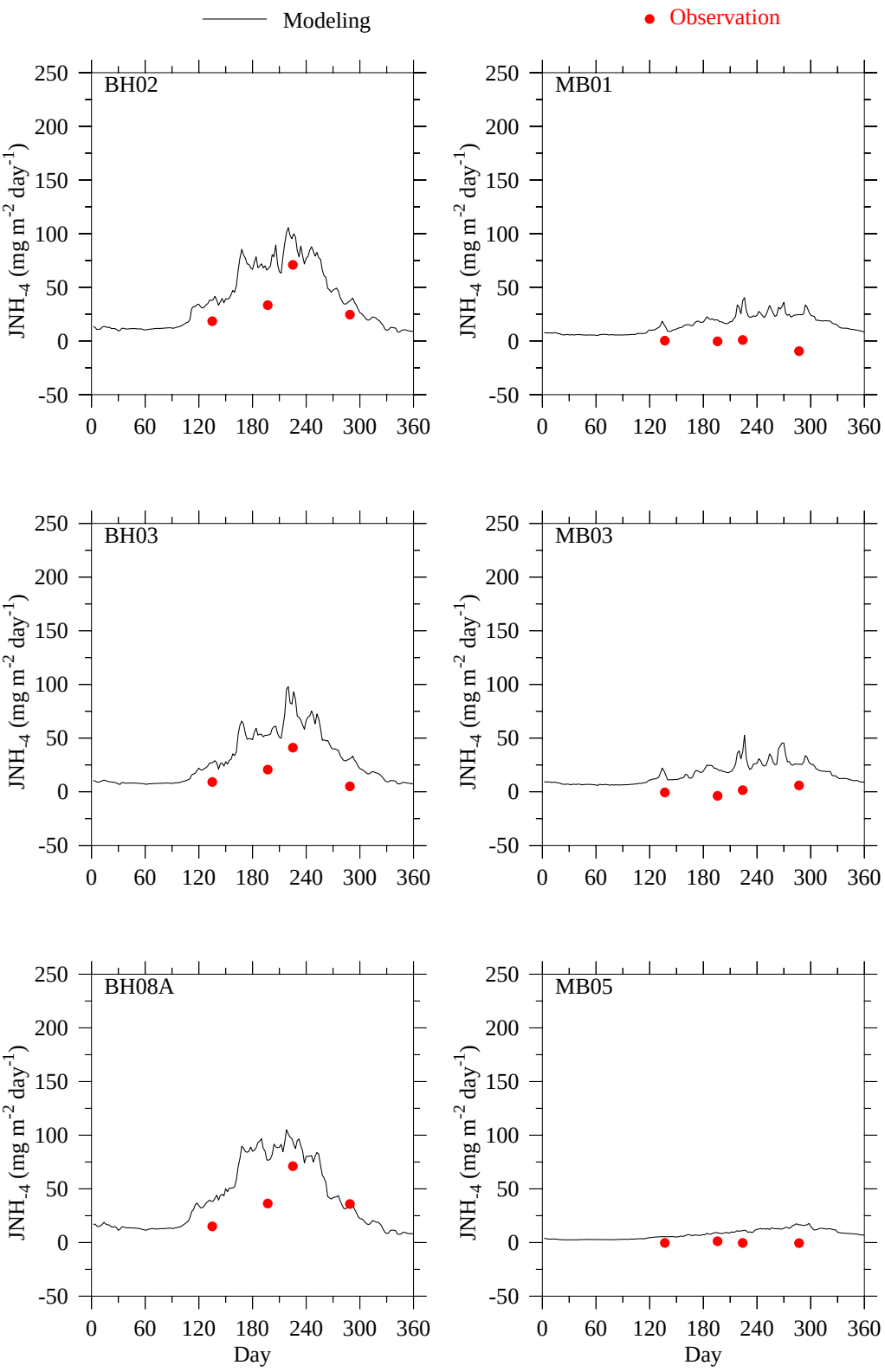

Figure 4.24 Comparison of observed (dots) and modeled (lines) time-series data of sediment NH_4^+ flux at monitoring stations in 2008.

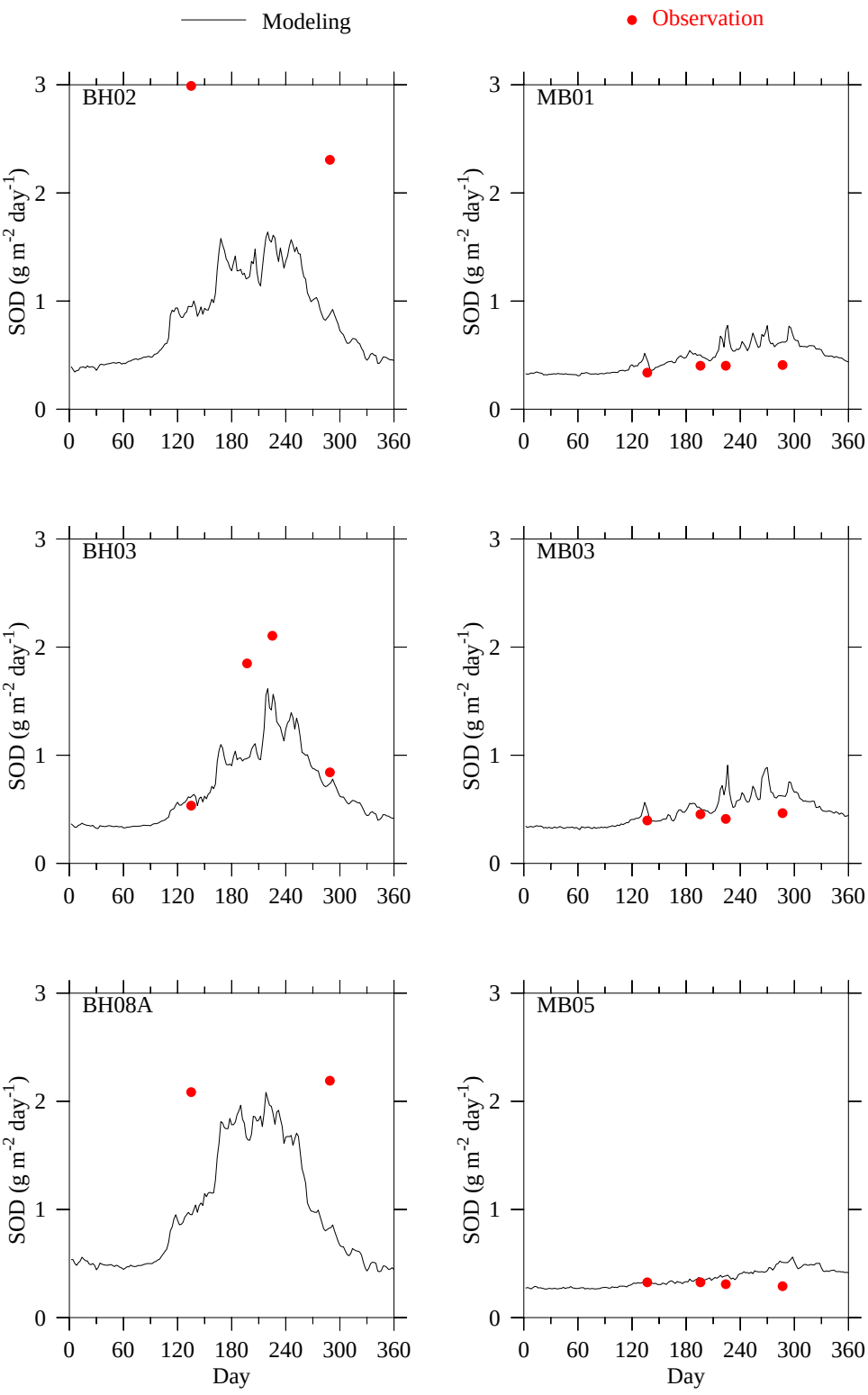

Figure 4.25 Comparison of observed (dots) and modeled (lines) time-series data of sediment oxygen demand at monitoring stations in 2008.

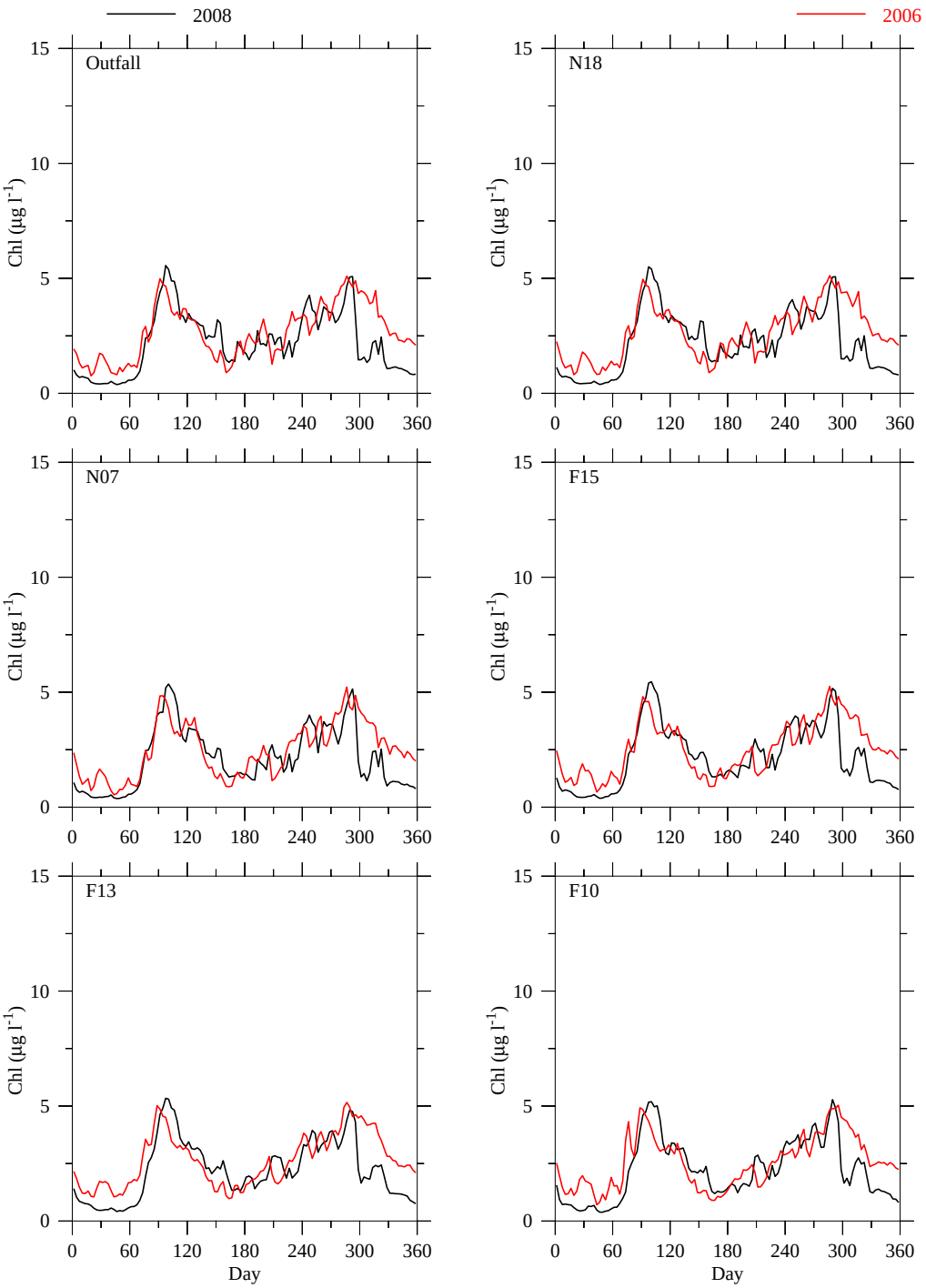

Figure 4.26 Seasonal and interannual variations in surface chlorophyll concentration at the MWRA outfall and Stations N18, N07, F15, F13 and F10 computed for 2006 (red line) and 2008 (black line).

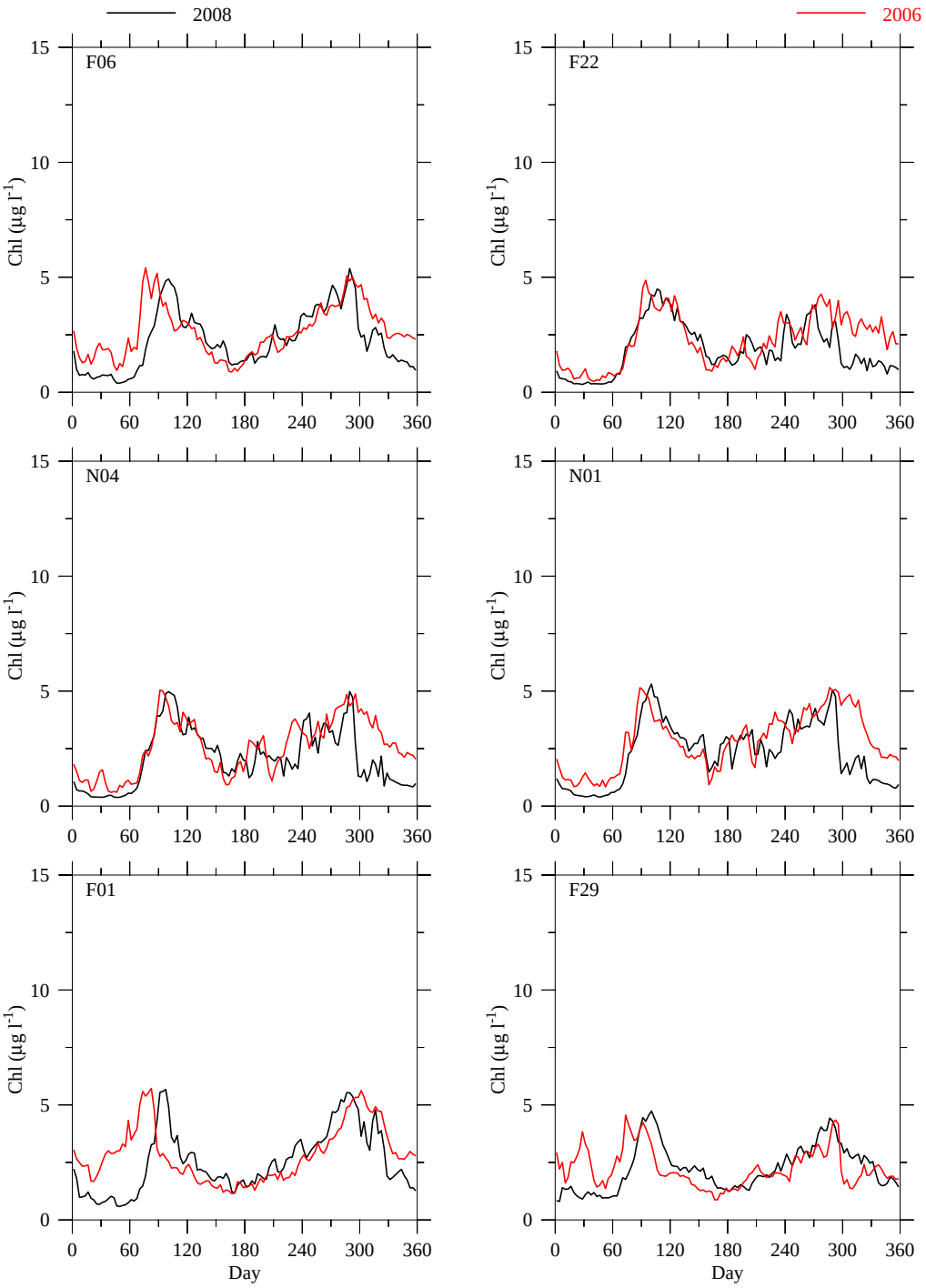

Figure 4.27 Seasonal and interannual variations in surface chlorophyll concentration at Stations F06, F22, N04, N01, F01 and F29 computed for 2006 (red line) and 2008 (black line).

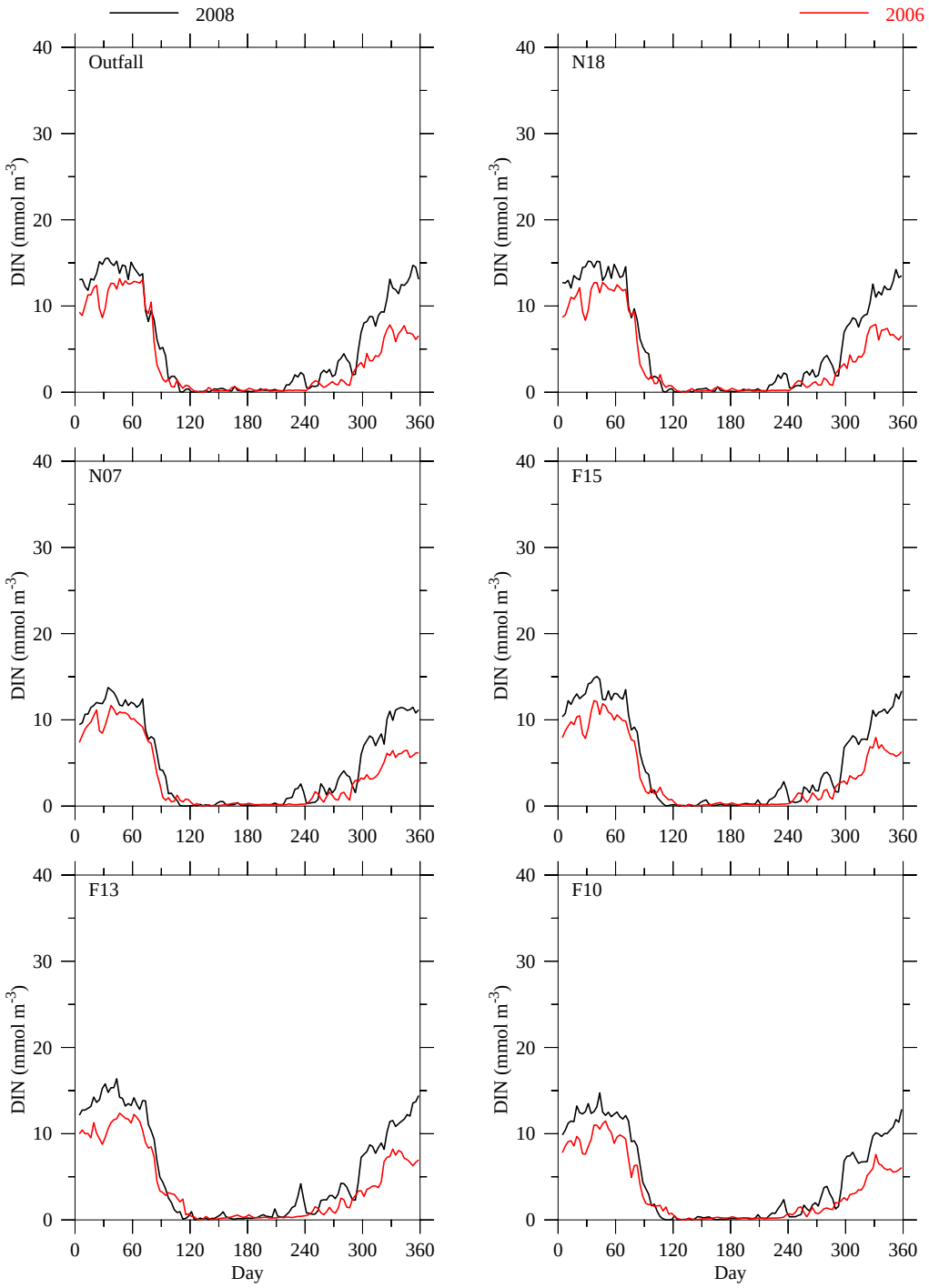

Figure 4.28 Seasonal and interannual variations in surface DIN concentration at the MWRA outfall and Stations N18, N07, F15, F13 and F10 computed for 2006 (red line) and 2008 (black line).

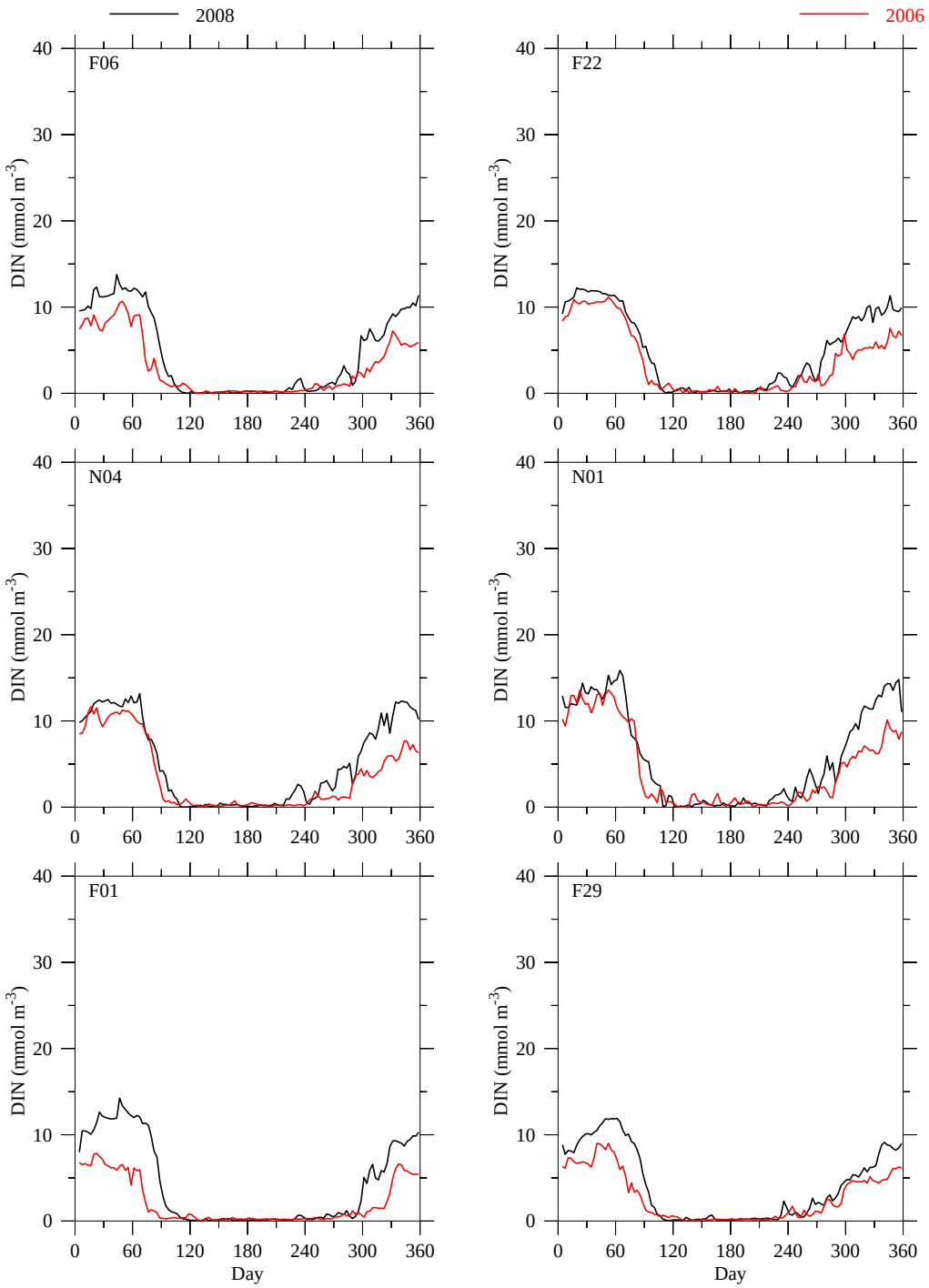

Figure 4.29 Seasonal and interannual variations in surface DIN concentration at Stations F06, F22, N04, N01, F01 and F29 computed for 2006 (red line) and 2008 (black line).

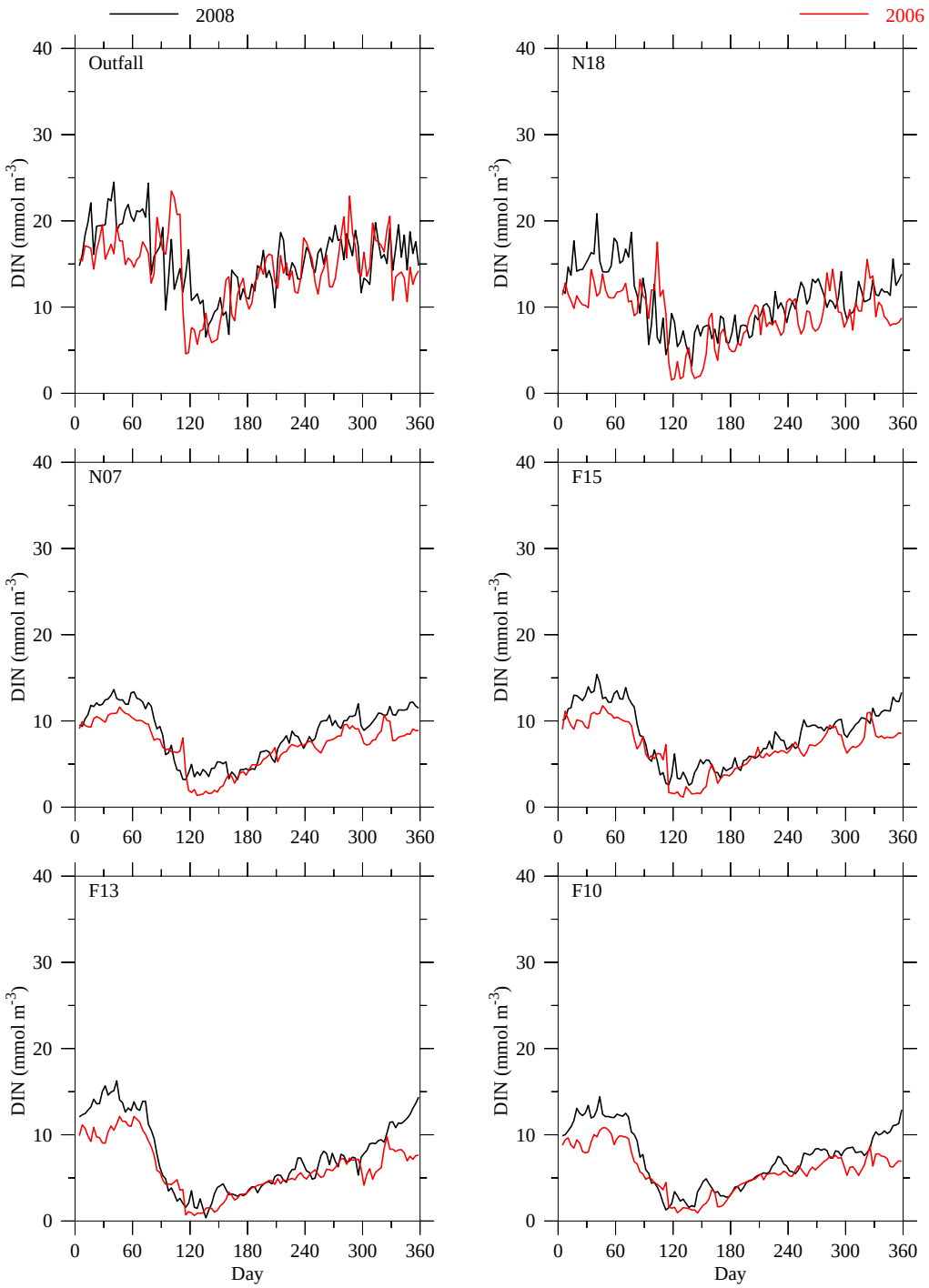

Figure 4.30 Seasonal and interannual variations in bottom DIN concentration at the MWRA outfall and Stations N18, N07, F15, F13 and F10 computed for 2006 (red line) and 2008 (black line).

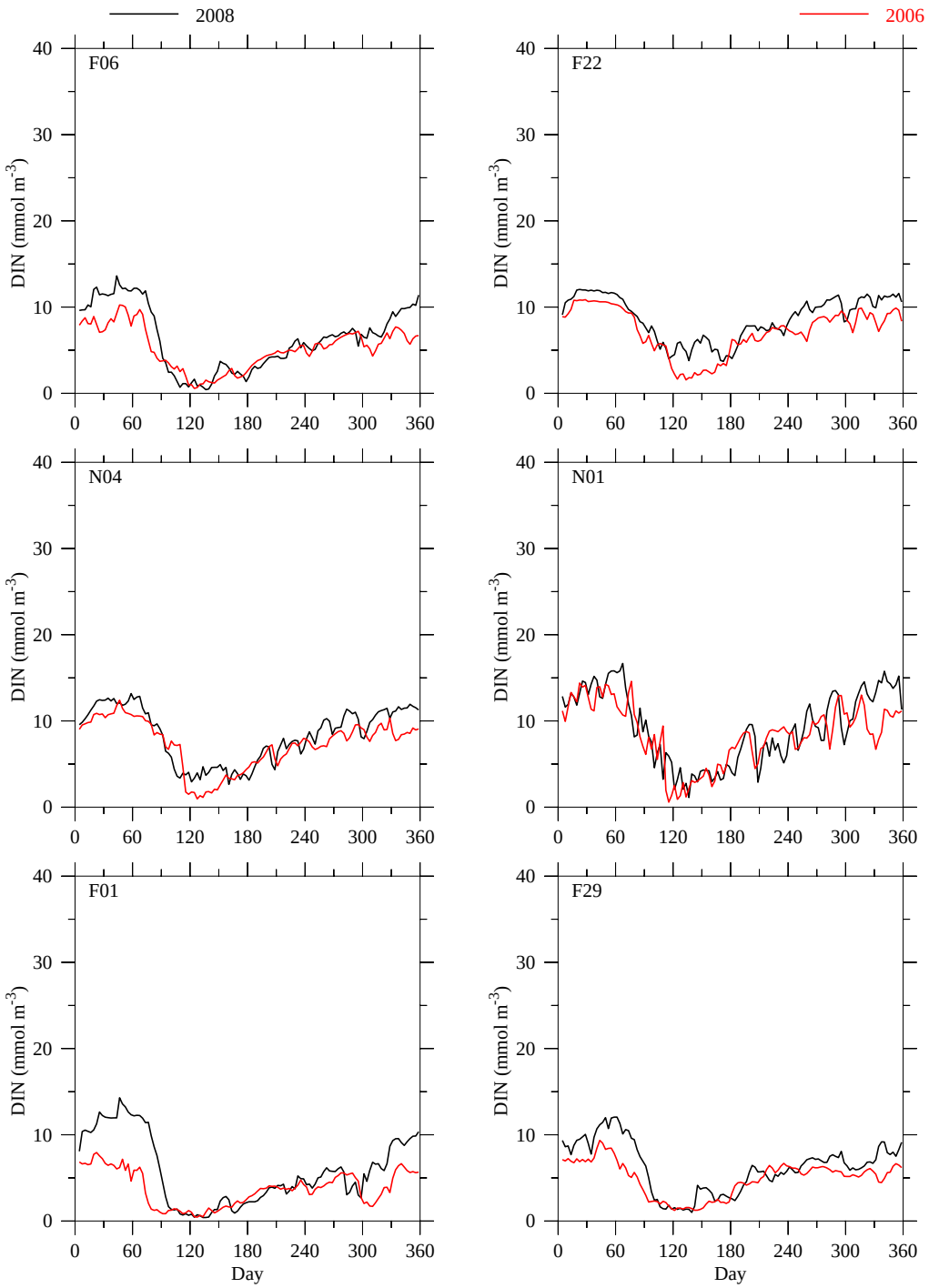

Figure 4.31 Seasonal and interannual variations in bottom DIN concentration at Stations F06, F22, N04, N01, F01 and F29 computed for 2006 (red line) and 2008 (black line).

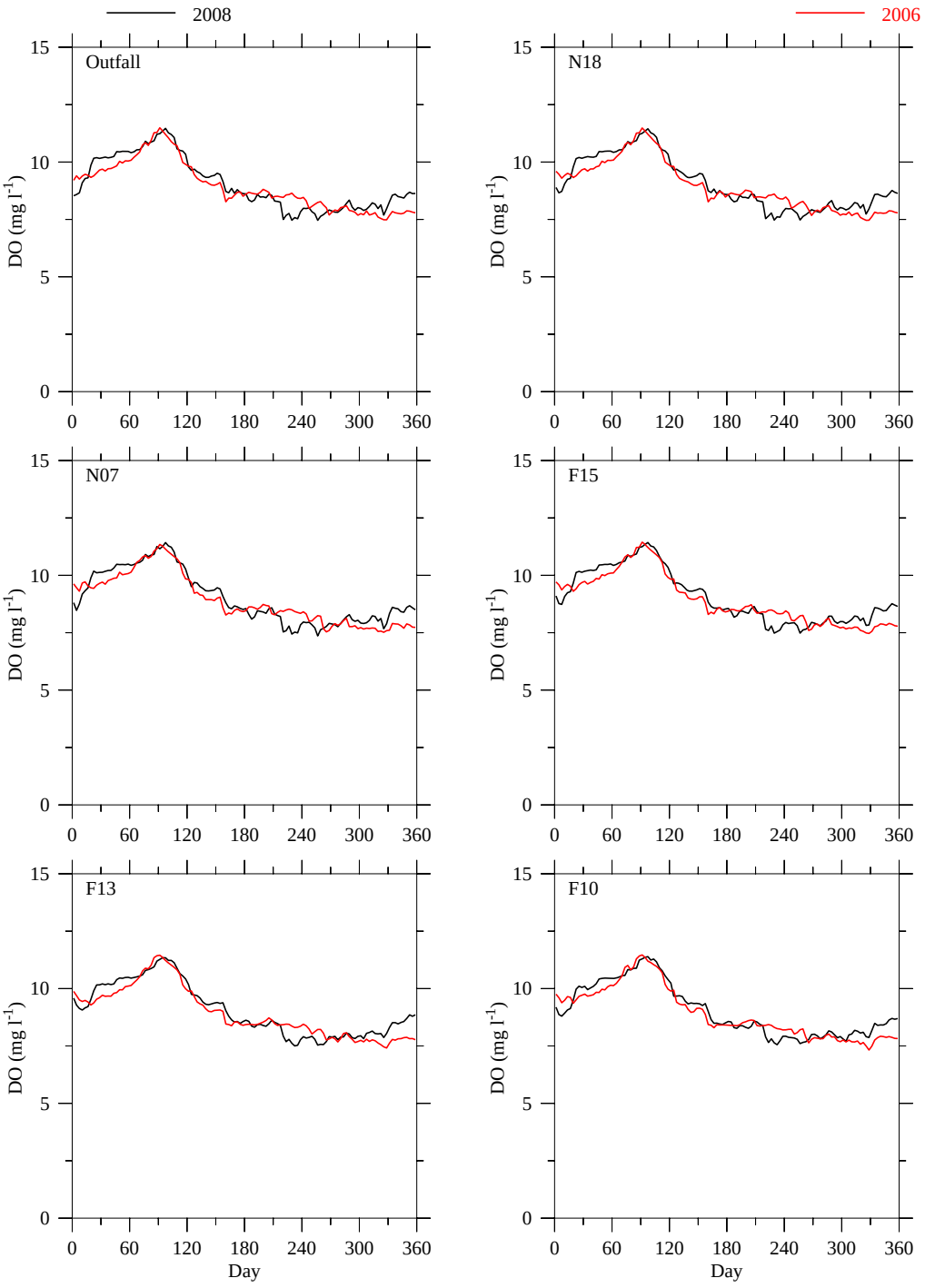

Figure 4.32 Seasonal and interannual variations in surface DO concentration at the MWRA outfall and Stations N18, N07, F15, F13 and F10 computed for 2006 (red line) and 2008 (black line).

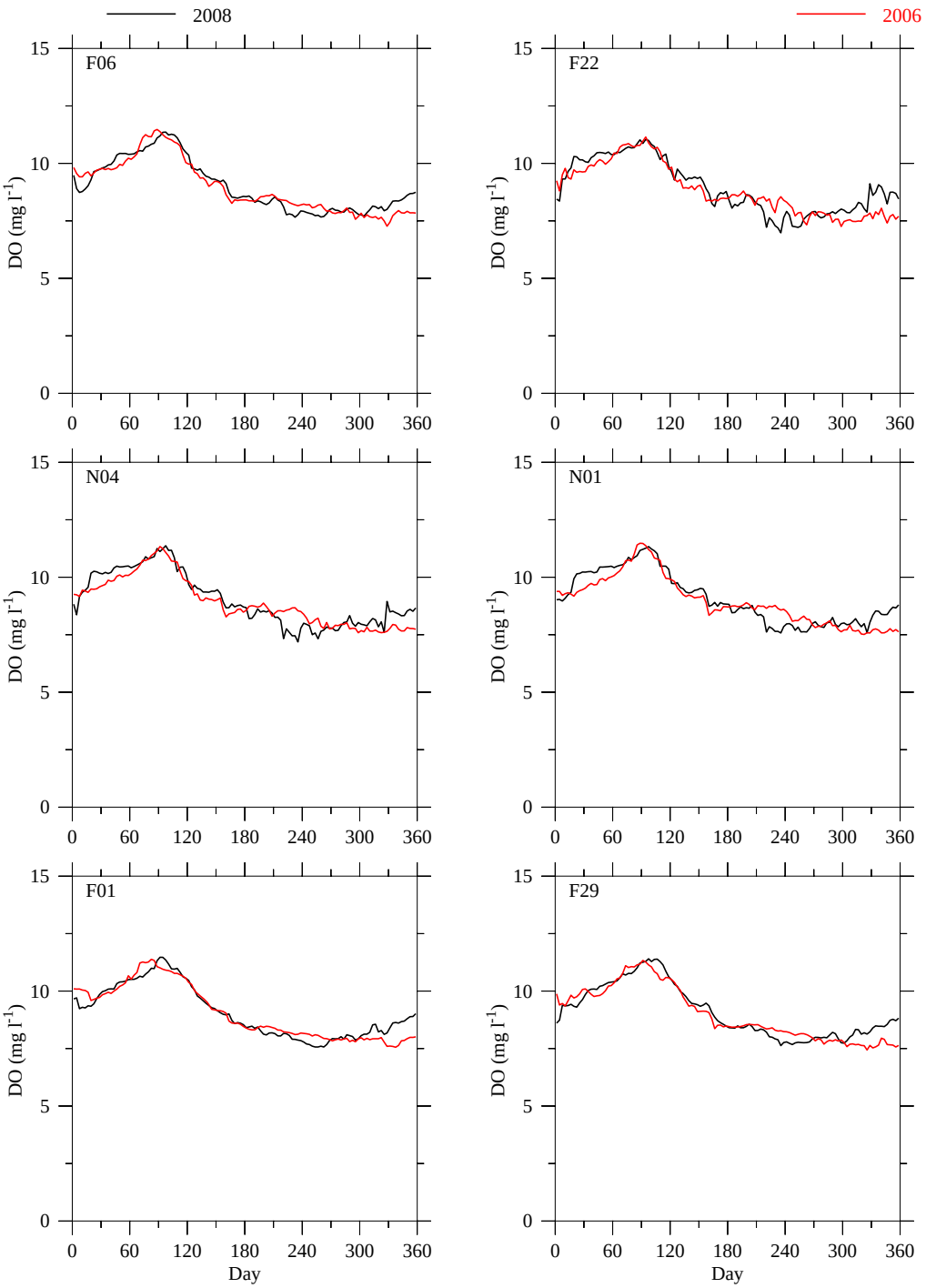

Figure 4.33 Seasonal and interannual variations in surface DO concentration at Stations F06, F22, N04, N01, F01 and F29 computed for 2006 (red line) and 2008 (black line).

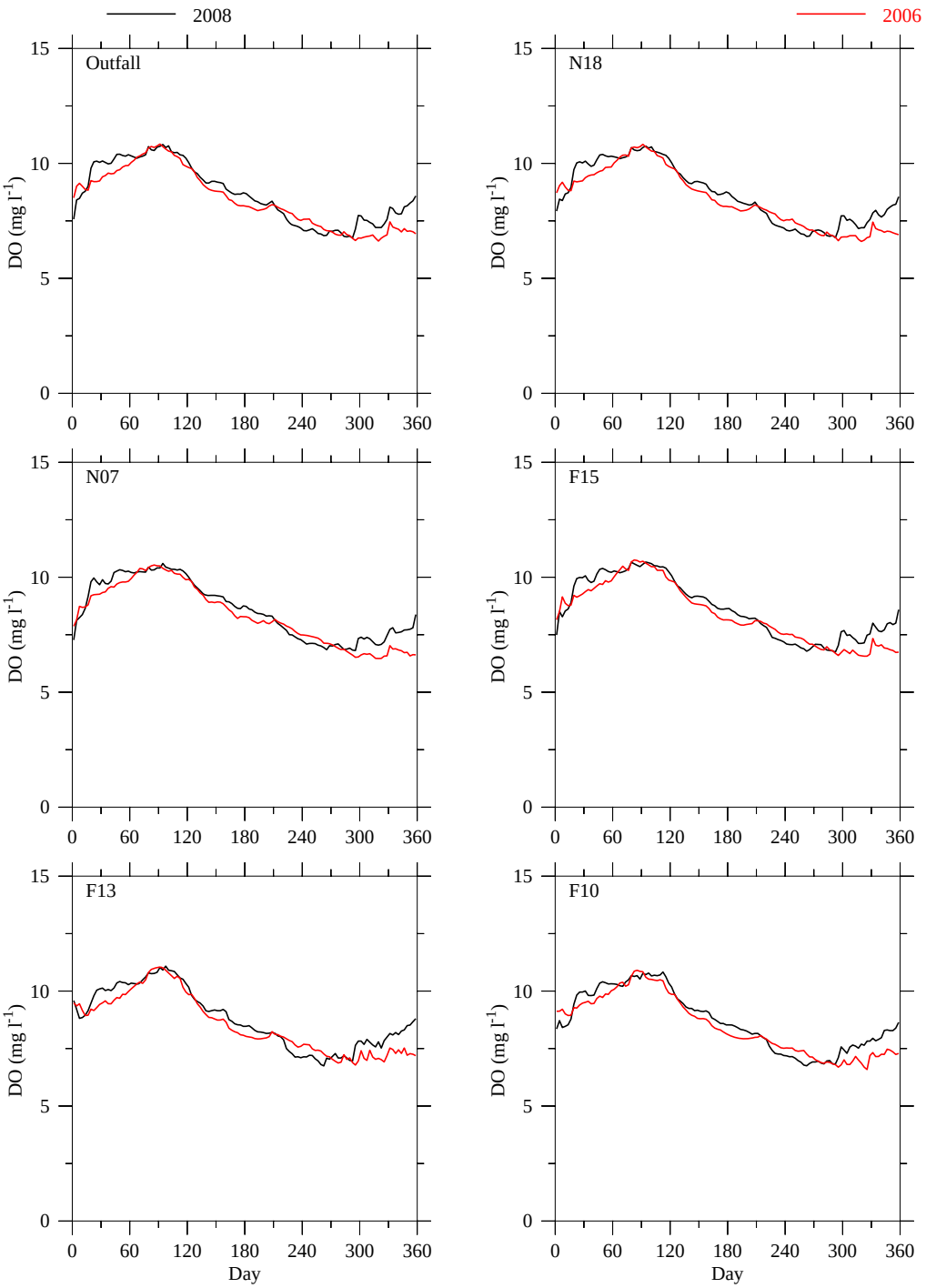

Figure 4.34 Seasonal and interannual variations in bottom DO concentration at the MWRA outfall and Stations N18, N07, F15, F13 and F10 computed for 2006 (red line) and 2008 (black line).

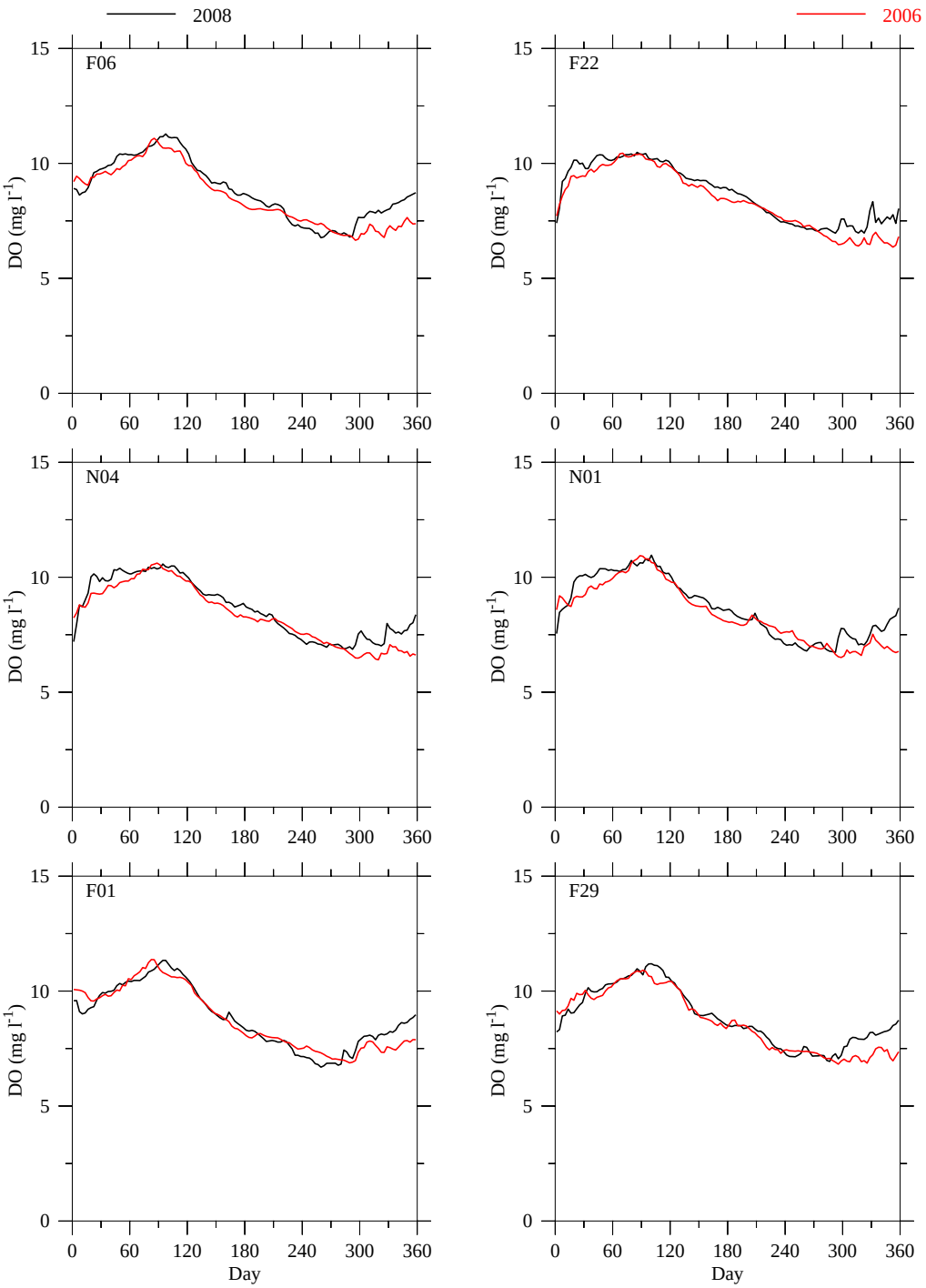

Figure 4.35 Seasonal and interannual variations in bottom DO concentration at Stations F06, F22, N04, N01, F01 and F29 computed for 2006 (red line) and 2008 (black line).

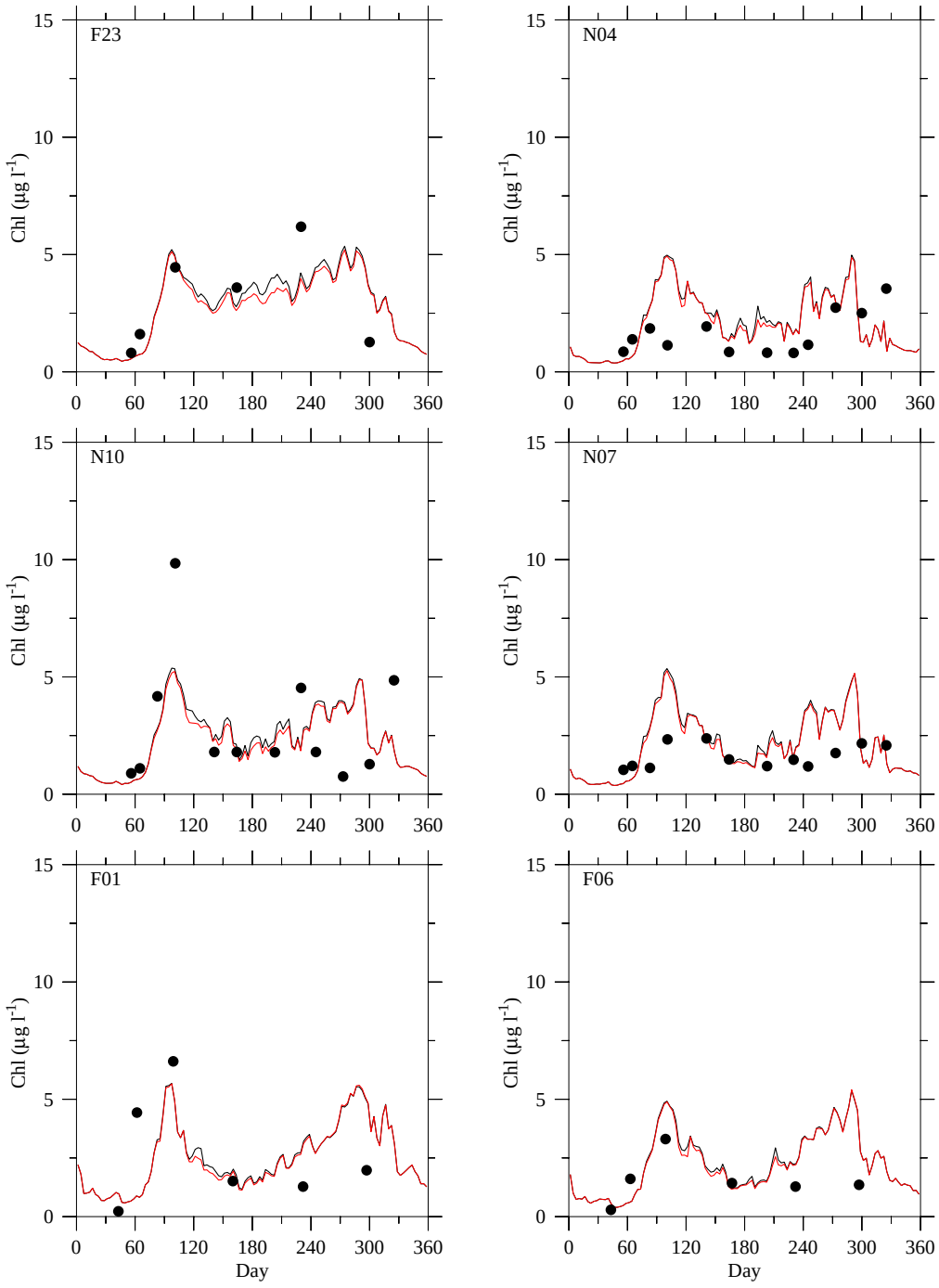

Figure 5.1 Comparison of surface chlorophyll concentration between the Control (black) and Non-sewage (red) experiments at selected monitoring stations in 2008.

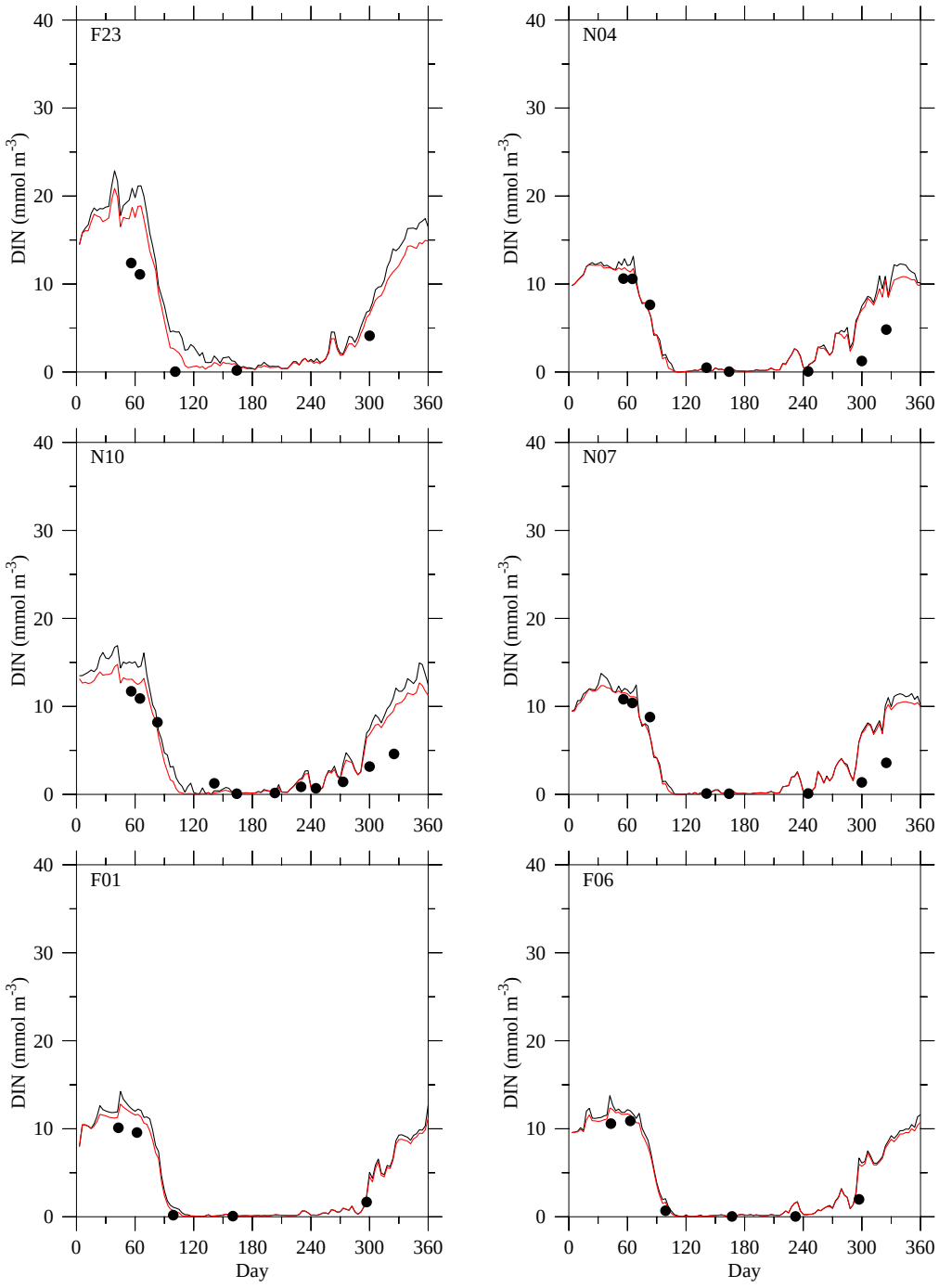

Figure 5.2 Comparison of surface DIN concentration between the Control (black) and Non-sewage (red) experiments at selected monitoring stations in 2008.

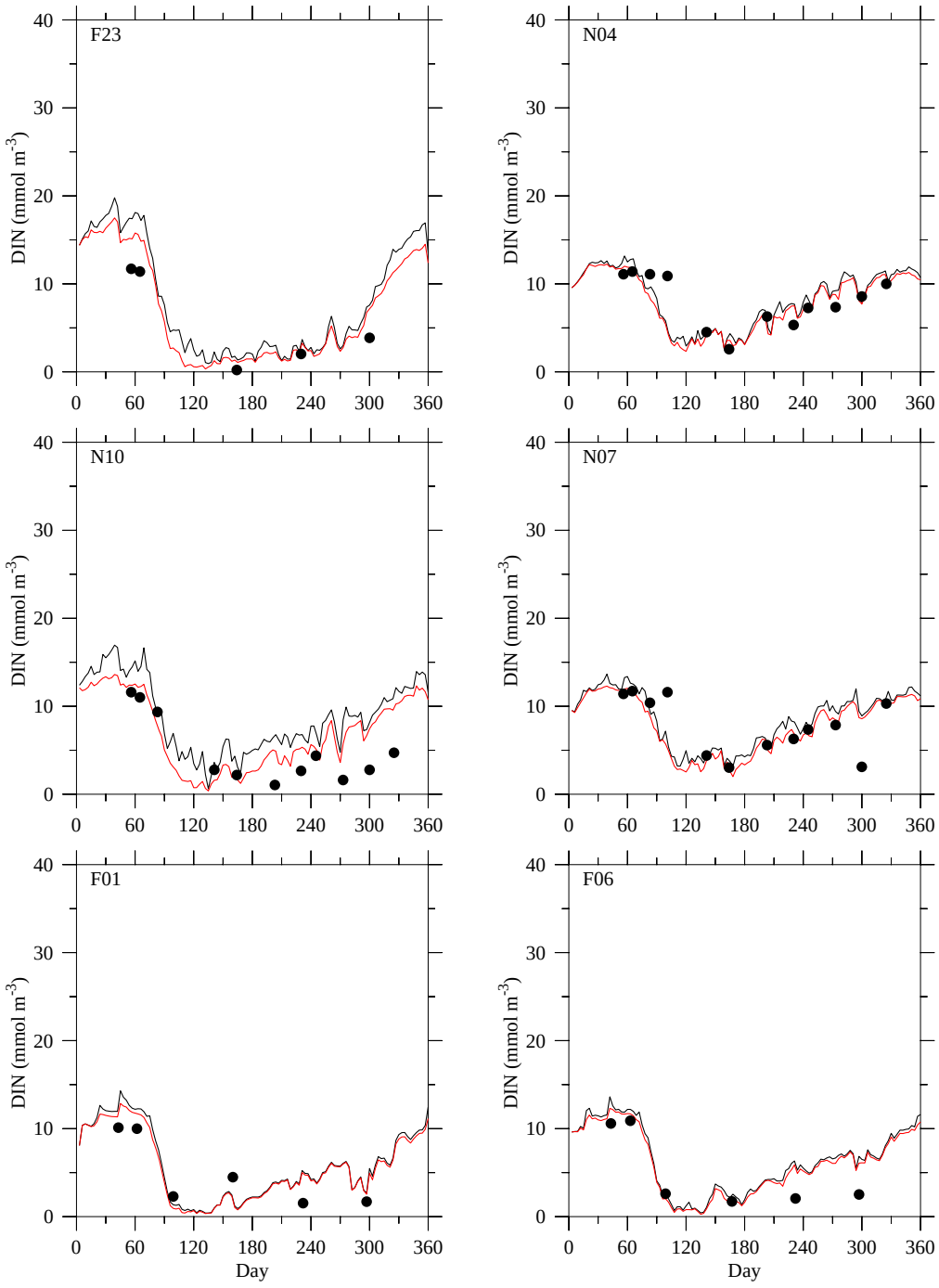

Figure 5.3 Comparison of bottom DIN concentration between the Control (black) and Non-sewage (red) experiments at selected monitoring stations in 2008.

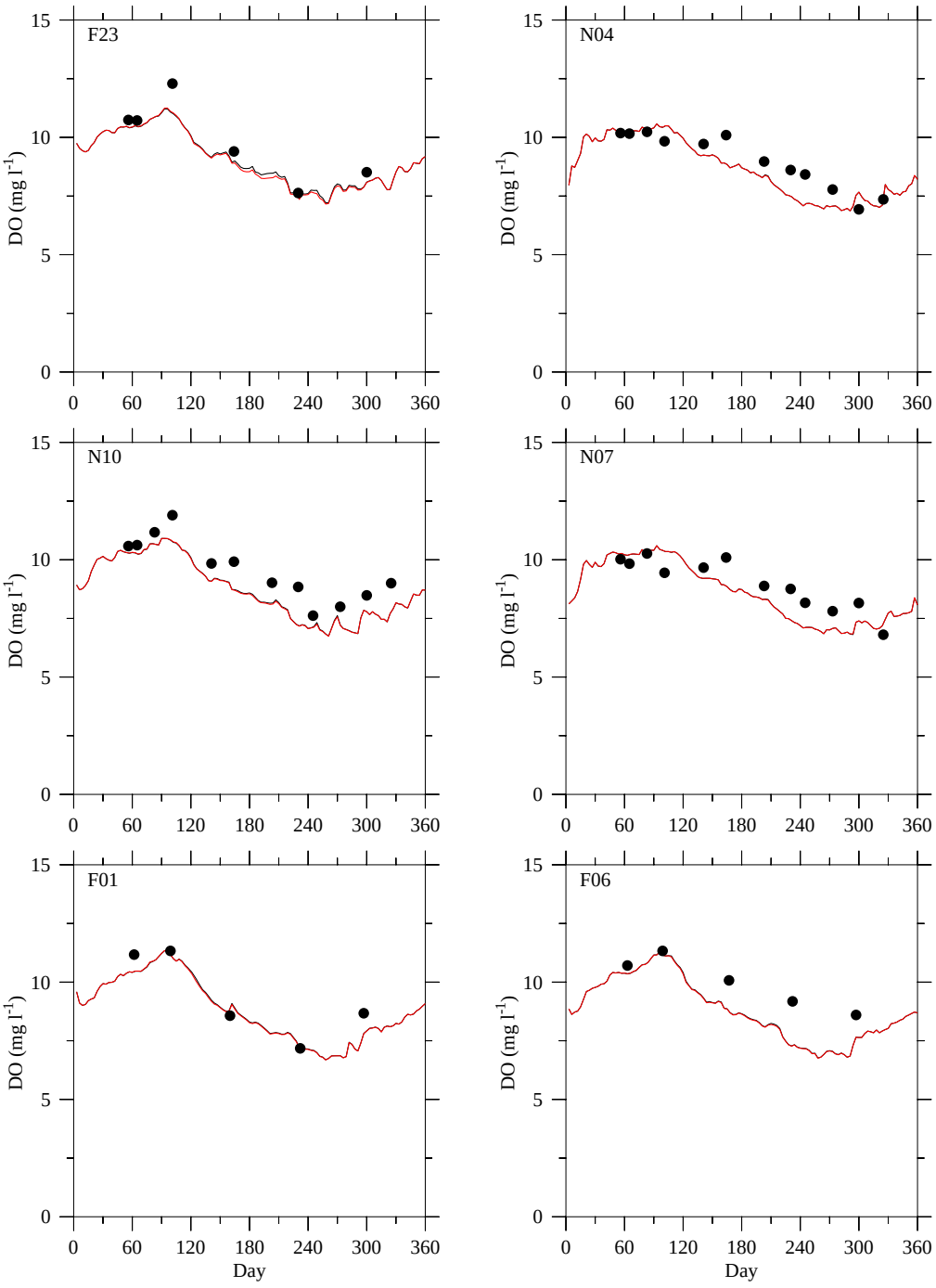

Figure 5.4 Comparison of bottom dissolved oxygen concentration between the Control (black) and Non-sewage (red) experiments at selected monitoring stations in 2008.

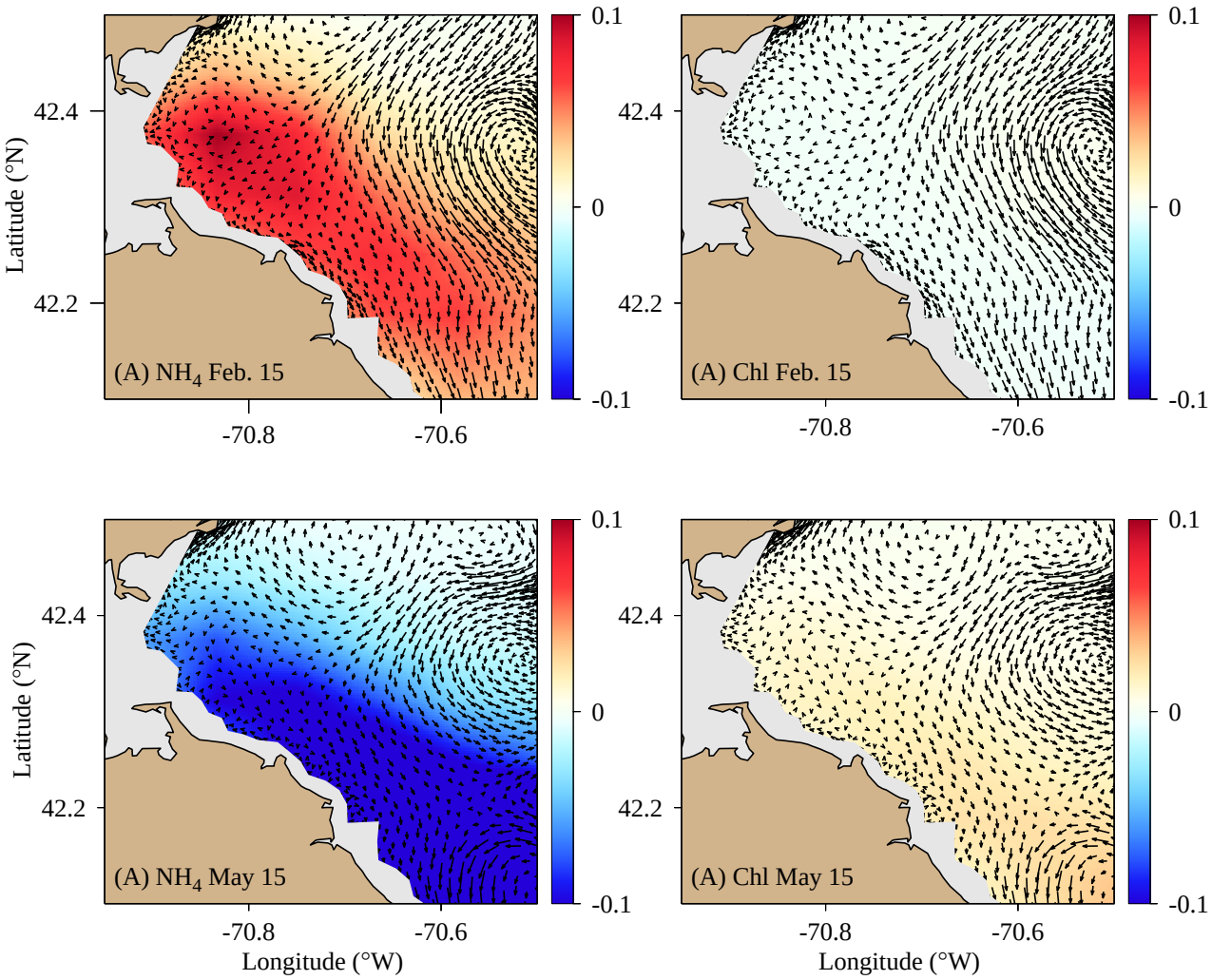

Figure 5.5 Current and differences in NH_4^+ and chlorophyll concentrations at 15-m depth on Feb 15 (upper panels) and May 15 (lower panels) between the Control and Non-sewage experiments in 2008. Red indicates Control is greater than Non-sewage.

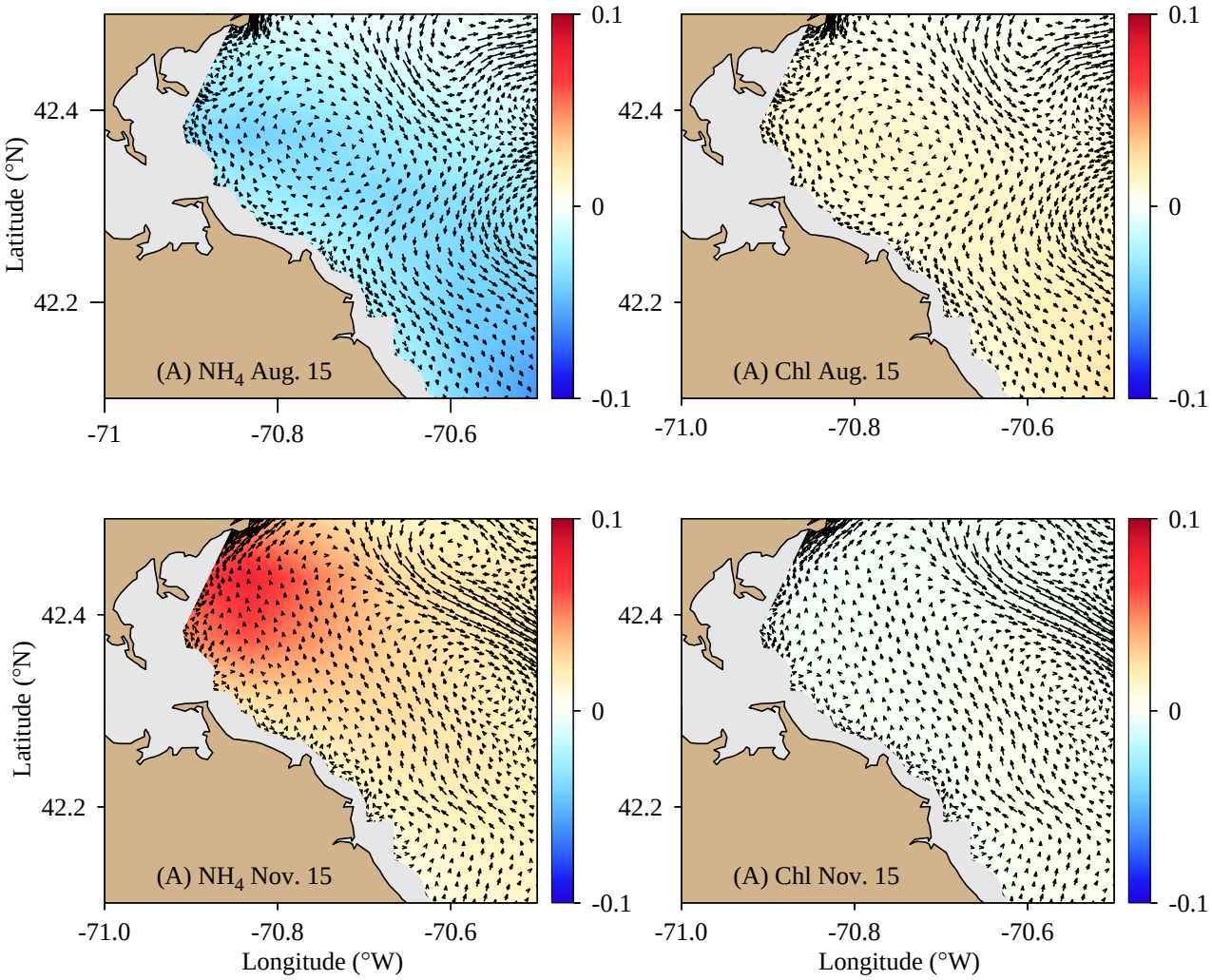

Figure 5.6 Current and differences in NH_4^+ and chlorophyll concentrations at 15-m depth on Aug. 15 (upper panels) and Nov. 15 (lower panels) between the Control and Non-sewage experiments in 2008. Red indicates Control is greater than Non-sewage.

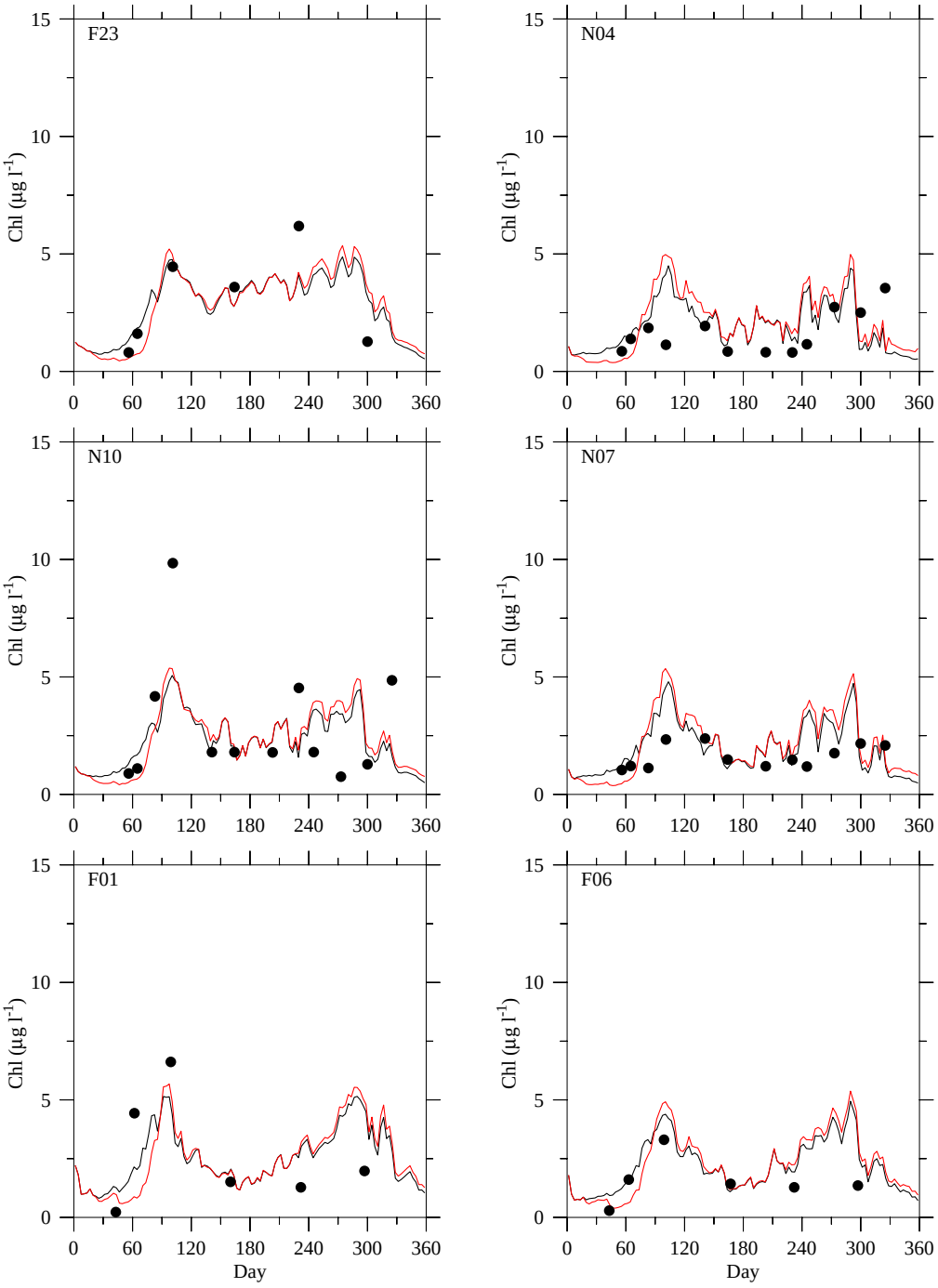

Figure 5.7 Comparison between reduced-data (black) and full-data simulation of chlorophyll in surface waters. Dots are observation data.

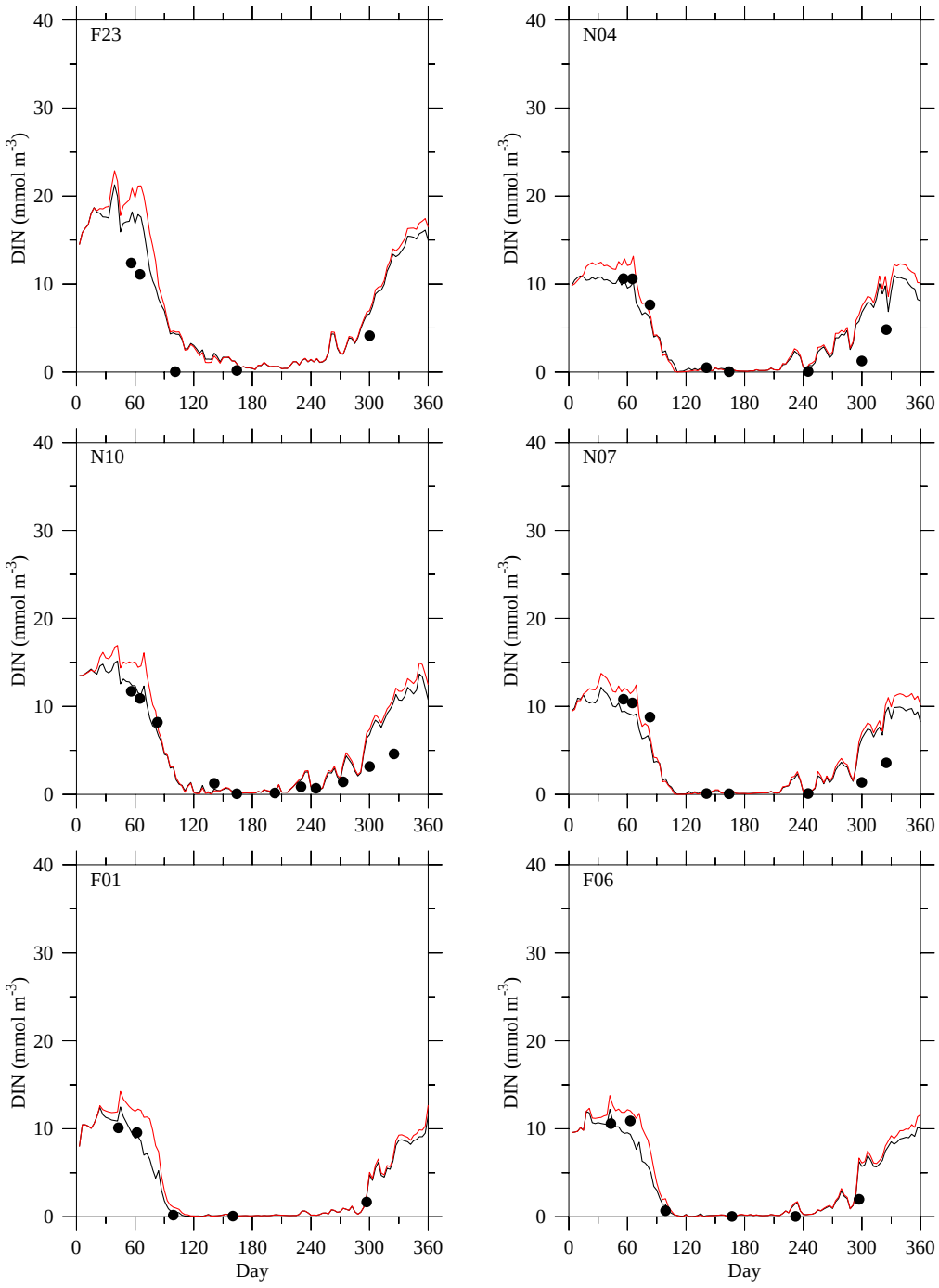

Figure 5.8 Comparison between reduced-data (black) and full-data simulation of DIN in surface waters. Dots are observation data.

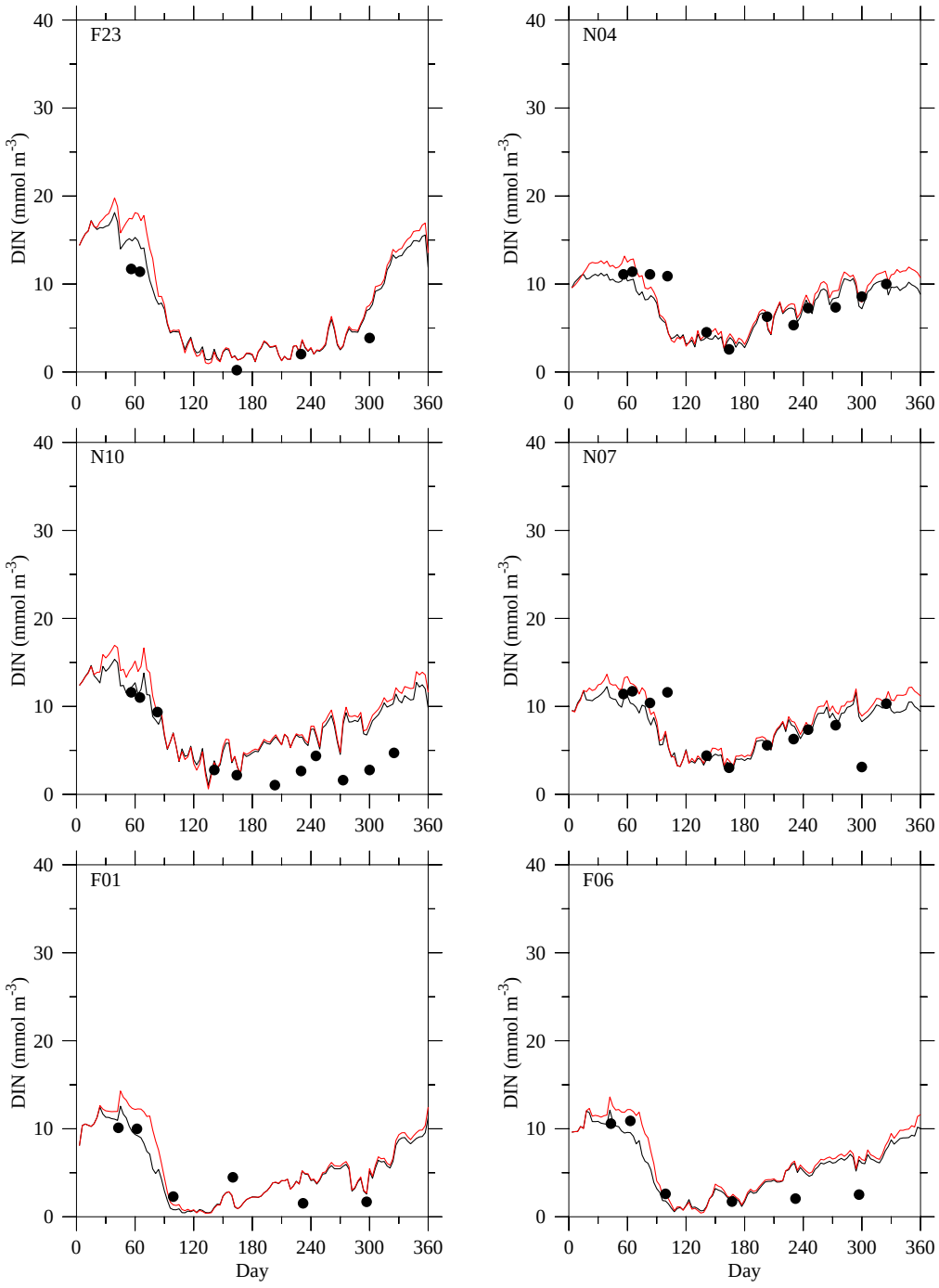

Figure 5.9 Comparison between reduced-data (black) and full-data simulation of DIN in bottom waters. Dots are observation data.

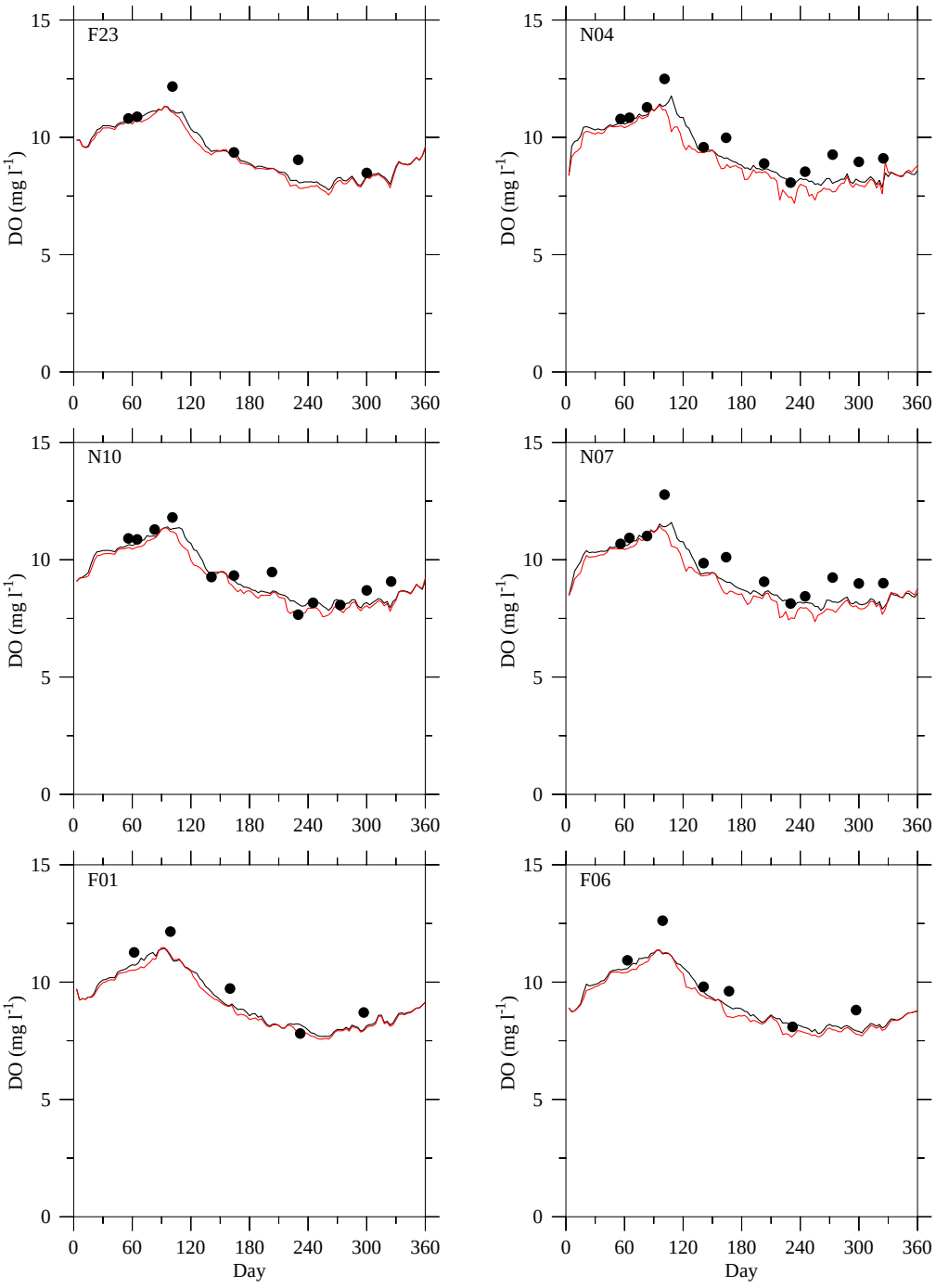

Figure 5.10 Comparison between reduced-data (black) and full-data simulation of DO in surface waters. Dots are observation data.

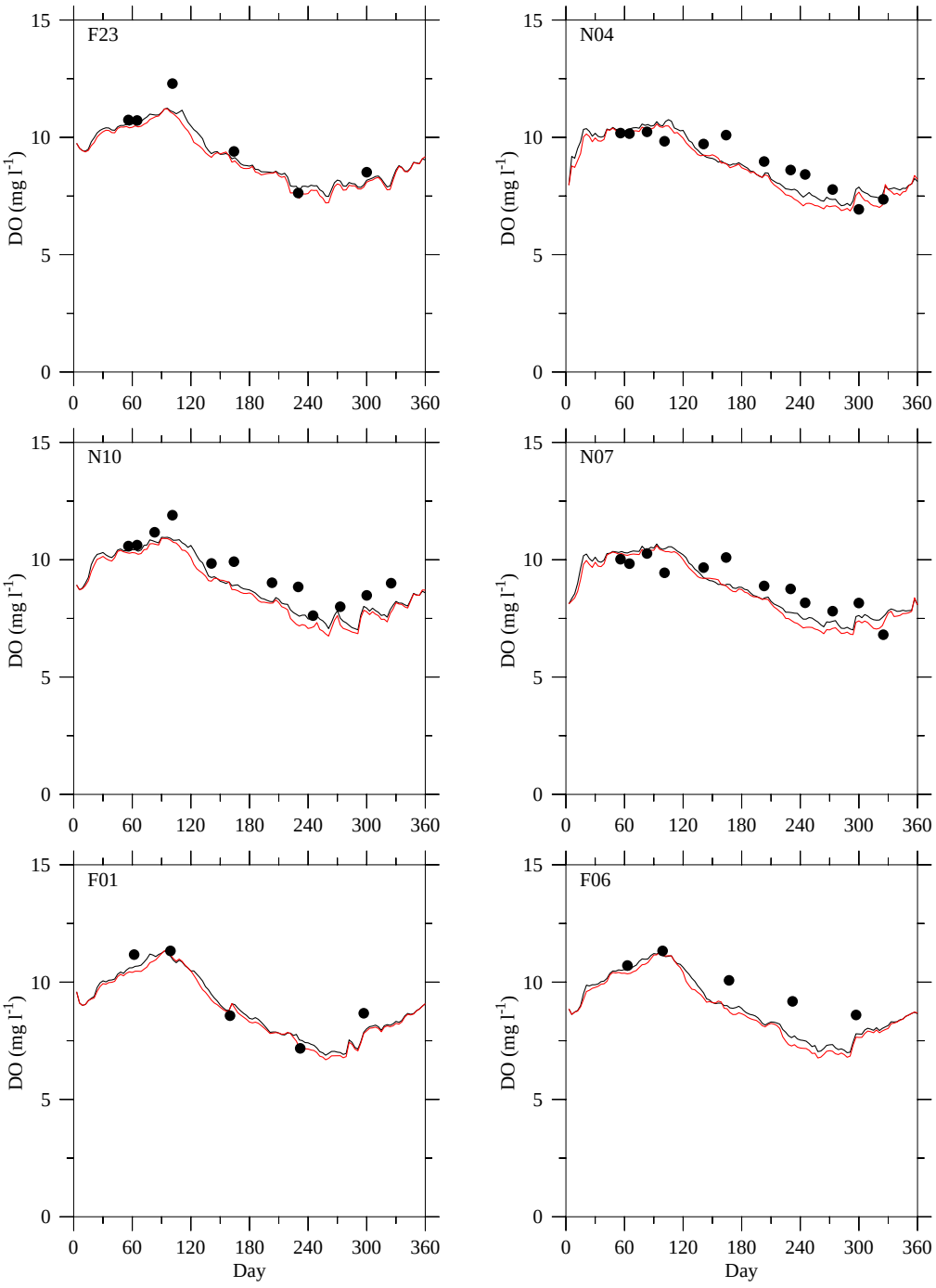

Figure 5.11 Comparison between reduced-data (black) and full-data simulation of DO in bottom waters. Dots are observation data.

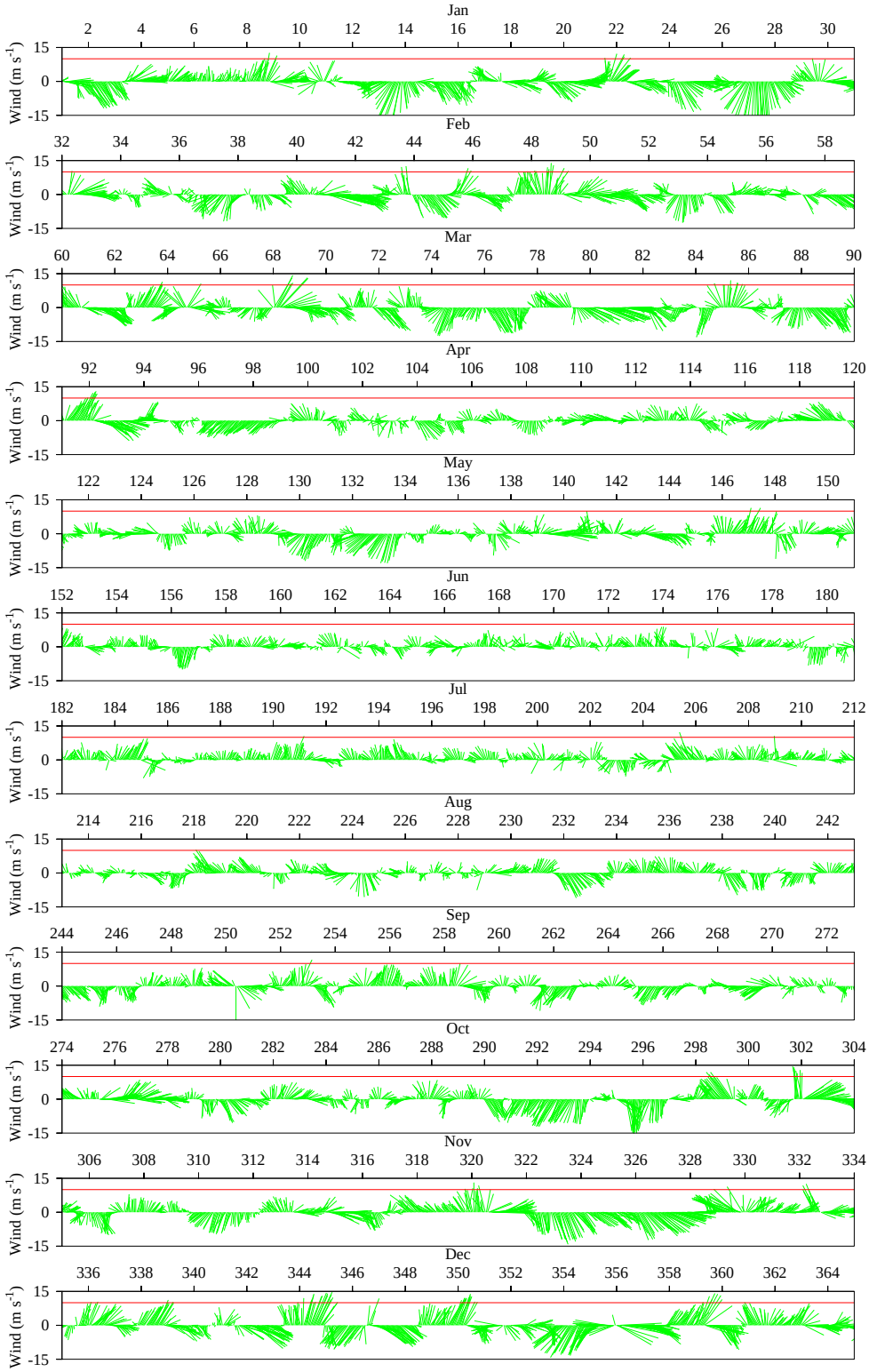

Figure 5.12 Hourly wind speed and direction at Buoy 44013 in 2008. The red line is the 10 m s^{-1} criterion as a measure of storm event (Butman et al., 2002).

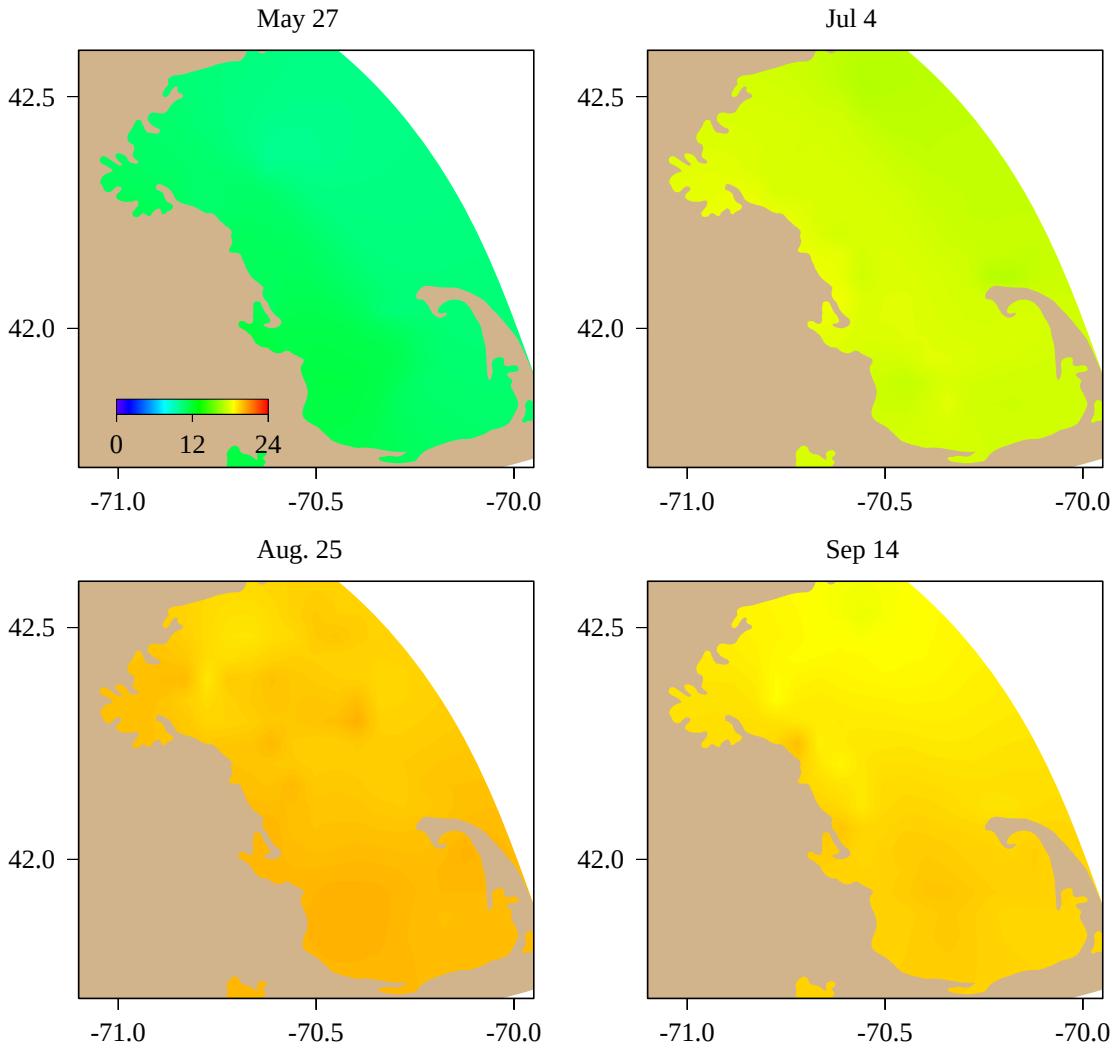

Figure 5.13 Surface temperature distribution simulated on days when moderate southerly wind prevailed in 2008.